Study of Early Transition Metal Carbides for Energy Storage Applications

A Thesis

Submitted to the Faculty

of

Drexel University

by

Yohan Dall'Agnese

in partial fulfillment of the

requirements for the degree

of

Doctor of Philosophy

March 2016

Acknowledgments

First of all, I would like to thank my PhD thesis advisors Prof. Yury Gogotsi, Dr. Patrice Simon and Dr. Pierre-Louis Taberna for providing me all the opportunities to do this research, their continuous support, and good advices throughout the projects. I was sincerely honored to meet and work with them.

I would like to sincerely thank my committee members: Prof. Richard Knight, Prof. Steven May and Prof. Aaron Fafarman for their time, useful comments and interest in my work.

I would like to acknowledge the financial support from the European Research Council (ERC, Advanced Grant, ERC-2011-AdG, Project 291543 — IONACES) and the Partnership Universities Fund (PUF) of French Embassy (PUF2012, "New twodimensional ceramics for better batteries").

I would like to thank all my collaborators, Olya Masthalir, Evelyn Chang Ren, Vadym Mochalin, Min Heon, Kevin Cook (Drexel University), Patrick Rozier, Barbara Daffos, and Benjamin Duployer (Université Paul Sabatier) with whom I had many useful and stimulating discussions. Separate thanks to Dr. Michel Barsoum, Dr. Michael Naguib and Dr. Maria Lukatskaya for their constructive feedbacks on my work.

I give special thanks to my labmates in CIRIMAT: Jeremy Come, Peihua Huang, Wan-yu Tsai, Etsuro Iwama, Koki Urita, Thomas Desaunay, Laurent Bazin, Zifeng Lin, Alagar Raj Paulraj, Léo Négre, Kévin Brousse, Yinghui Yin and Dasha Iermakova. I am also grateful to Noé, Hélène, Jean-Baptiste, Papy, Fréd, Florent, Elodie, Nicolas, Souphiane, Sébastien, Kévin, Romain, Claire, Jessica, Dalya, Imane, Vincent, Charles,

Abdé, Guillaume, Alexis and Benjamin for making my working experience fun and unforgettable. I would like to thank administrative help from Soraya Berkouk, Laetitia Lale and Sandra Geminiano, Nicole Luga, Nabila Smahi, Sandrine Cerny, Christiane Bonino, Murielle Soleillant and Maryse Bellanger. I would like to thanks all the research engineers, PhD students, Master students, postdoctoral researchers and professors from CIRIMAT whom I have not mentioned but were part of this adventure.

Additionally I'm also grateful to all my group mates in Drexel who have helped in many ways, in particular: Kristy Jost, Carlos Pérez, Boris Dyatkin, Riju Singhal, John McDonough, Amanda Pentecost, Kelsey Hatzell, Katie van Aken, Chuanfang (John) Zhang, Joseph Halim, Mengqiang Zhao, Jonathan Campos, Vadym Borysiuk, Majid Beidaghi and Muhammad Boota. I particularly thank Babak Anasori and Michael Ghidiu for help with the synthesis of both MAX phases and MXenes. Special thanks to Tyler Mathis, Katie van Aken, and Kathleen Maleski for helpful corrections. I would like to thank the Drexel Nanomaterials Institute staff; Wendy Thurman, Michelle Sipics and Danielle Tadros Kopicko for their indispensable administrative support.

Last but not least, my deepest gratitude goes to my family for their love, patience and never-ending support. I specially thank to my wife, Sissi, for her endless support and encouragement during my Ph.D.

Table of Contents

List of Tables

List of Figures

Abstract

Study of Early Transition Metal Carbide for Energy Storage Applications

Yohan Dall'Agnese

Advisor: Professor Yury Gogotsi

An increase in energy and power density is needed to match the growing energy storage demands linked with the development of renewable energy production, and portable electronics. Several energy storage technologies exist including lithium-ion batteries, sodium-ion batteries, fuel cells and supercapacitors. These systems are mutually complementary. For example, supercapacitors can deliver high power densities whereas batteries can be used for high energy density applications.

The first objective of this work was to investigate the electrochemical performances of a new family of 2-D materials called MXenes by cyclic voltammetry and galvanostatic charge-discharge measurements and to propose new solutions to tackle the energy storage concern. To achieve this goal, several directions have been explored. The first part of the research focused on Ti_3C_2-based MXenes behavior as electrode materials for supercapacitors in aqueous electrolytes. The charge storage mechanisms in basic and neutral aqueous electrolytes, investigated by X-ray diffraction, were demonstrated to be attributed to cations intercalation between Ti_3C_2 layers. X-ray photoelectron spectroscopy highlighted the contribution of oxygenated functional groups on surface redox reactions in sulfuric acid. High capacitances were achieved, up to 520 F/cm^3 and 325 F/g.

Then the electrochemical behaviors of MXenes in sodium-based organic electrolytes were explored. A new hybrid system of sodium-ion capacitor was proposed. It was demonstrated that V_2C-based MXene electrodes were suitable to be used as positive electrodes with an operating potential from 1 V to 3.5 V *vs.* Na^+/Na. Continuous intercalation and de-intercalation of sodium ions between the V_2C layers during sodiation and desodiation were showed by X-ray diffraction. An asymmetric sodium-ion capacitor full cell was assembled using hard carbon as negative electrode and showed promising results, with a capacity of 50 mAh/g.

The last part was focused on the study of MXene electrodes for supercapacitors in an organic electrolyte; 1-ethyl-3-methylimidazolium bis(trifluoromethylsulfonyl)imide (EMITFSI) in acetonitrile. High volumetric capacitances, up to 245 F/cm^3, were achieved by using carbon nanotubes as an additive to improve ion accessibility to Ti_3C_2 layers. The redox intercalation of large EMI^+ cations between Ti_3C_2 layers at -0.4 V *vs.* Ag was observed by X-ray diffraction.

General Introduction

Since the 19th century, the main energy sources have been fossil fuels (oil, gas and coal) which has led to economic concerns (limited resources) and ecological issues (global warming). With the rise of renewable energy sources (wind, sun, hydropower and other) one of today's challenges has been to create cheaper and more efficient technologies to store this intermittent energy (*1, 2*). Recently, another challenge has emerged with the wide use of rechargeable portable electronic devices (laptops, smart phones, etc.) that require increasing energy and power densities. Electrochemical energy storage solutions such as batteries and supercapacitors are environmentally friendly and have the advantage of excellent efficiency and scalability (*3-5*). Batteries store the energy through electrochemical reduction and oxidation reactions while supercapacitors, also called electrochemical capacitors, store energy through double layer electrostatic interactions (*6*).

The demand for higher energy and power densities is continuously increasing. Unfortunately, current commercial batteries and supercapacitors are not suitable for future needs (*5, 7*). To be economically sustainable, electrode materials need to provide better performance at the same cost or lower. Indeed, commercial supercapacitors suffer from low energy densities because they use activated carbon electrodes which store the energy only through double layer capacitance (*4*). In recent years it has been proposed that a promising method to reach higher energy densities with supercapacitors is to use pseudocapacitive materials that store energy through fast redox reactions. In a different

manner, hybrid capacitors based on lithium-ion battery technology are another solution proposed to increase the energy density.

The work reported herein focuses on the electrochemical performance of a new family of materials called MXenes. MXenes are a family of two-dimensional transition metal carbides which have shown promising results in the field of lithium-ion battery applications (*8*, *9*). The motivation to study these materials was that their chemical compositions are more diverse than carbon and contain transition metals that can allow redox reactions and higher energy densities. In this work, a few members of this family were investigated; Ti_3C_2, Ti_2C, Ti_3CN, Nb_2C, V_2C, $Ti_{1.5}V_{1.5}C_2$ and TiVC, in 3 different electrochemical storage devices: supercapacitors, sodium-ion batteries and sodium-ion capacitors.

The first chapter is a bibliographic review. The principle of lithium-ion batteries is explained before focusing on the state of the art of sodium-ion batteries and electrochemical capacitors. Finally, a summary of the performance of various two-dimensional materials used for energy storage are given in the last part, before concluding with an introduction about the new family of MXenes. The second chapter describes the experimental methods used. In particular, MXene synthesis from MAX phases is presented, as well as its delamination treatment. The basic principles of the electrochemical, structural and chemical material characterizations are also given.

The third chapter focuses on the electrochemical performance of Ti_3C_2 as an electrode material for electrochemical capacitors in aqueous electrolytes. The spontaneous intercalation mechanism of aqueous electrolyte ions into MXene is described. The fourth chapter starts with an overview of all synthesized MXene material behavior upon sodium

ion intercalation in half-cell batteries. V_2C was identified as a promising electrode for sodium-ion capacitor and further used V_2C as a positive electrode in a full cell with hard carbon as the negative electrode. In the fifth chapter, MXene electrochemical behavior was investigated in organic electrolytes. The electrochemical storage mechanism was analyzed by *in-situ* X-ray diffraction. In the final part, the general conclusions and perspectives of this work are presented.

CHAPTER 1: Background and Literature Survey

1.1 Electrochemical storage

The first reported electrochemical storage device was a battery created by Alessandro Volta in 1800 (*10*). It consisted of zinc and copper electrodes separated by a paper soaked with NaCl electrolyte. The mechanism taking place (oxidation of the Zn and oxygen reduction at the Cu electrode) was not understood until 1834 when Michael Faraday demonstrated that the oxidation state of the Zn metal changed during the reaction. This discovery led to the creation of a new scientific field called Electrochemistry. The 19^{th} and 20^{th} centuries saw the development of electrochemical energy storage technologies such as batteries and supercapacitors.

Among the numerous great improvements in batteries, some of the most notable were the development of the lead-acid battery by Gaston Planté in 1859; the Zn-MnO_2 dry cell in 1887, the first nickel-cadmium battery in 1899, the commercial success of the alkaline battery in 1959 and finally, after the discovery in 1980 of $LiCoO_2$ as cathode material from J. Goodenough (*11*) and graphite as anode from B.Scrosati and others (*12*), SONY introduced the lithium-ion battery to the market in 1991. The latter has revolutionized portable electronic devices (phone, laptop, etc.) and electric vehicles (Tesla).

Research on supercapacitors is more recent with the first patent in 1957 from H. Becker at General Electric, consisting of stainless steel electrodes in a sulfuric acid electrolyte (*13*). However, the charge mechanisms were not yet understood. Research done between 1966 and 1970 at Sohio Corporation (Standard Oil Company of Ohio) using graphite electrodes in an organic electrolyte (*14*) revealed that the charge storage

mechanism was due to the formation of a double layer, the interphase of which was studied by Helmholtz in 1879 (*15*). Commercial applications waited until 1982 by the Nippon Electric Company. The first devices had low capacitances and low energy densities (0.5 Wh/kg) limiting their applications. Nevertheless, better products based on activated carbon were quickly commercialized by several companies that invested in the research, such as Panassonic, Elna, ECOND, Maxwell and Batscap. Different commercial electrochemical capacitors were produced for various applications, from transport (stop and go) to large-scale stationary storage. Electrochemical capacitors based on another principle, called pseudocapacitance, have also been studied (*16*). Conway was the first to describe oxide materials that store energy through fast faradaic reactions. Pseudocapacitor materials are typically transition metal oxides (RuO_2, MnO_2, V_2O_5, etc.) and electronically conducting polymers (polyaniline, polypyrrole, etc.) but no commercial application has emerged so far (*4, 17*).

Nowadays, many different chemistries can be used for electrochemical energy storage devices that broaden the range of energy and power densities available, as shown Figure 1. The energy and power stored are calculated according to:

$$E = \frac{1}{2} C \times \Delta V^2 \quad (1)$$

$$P = \frac{\Delta V^2}{4R} \quad (2)$$

Where C is the capacitance of the cell (F), ΔV is the potential window (V) and R is equivalent series resistance (Ω).

It appears that energy storage through faradaic oxidation-reduction reactions in batteries provides higher energy densities but lower power densities than devices that

store energy through electrostatic interaction such as electrochemical capacitors. In the following, the scientific principles of lithium-ion batteries, sodium-ion batteries, electrochemical capacitors and hybrid capacitors are introduced.

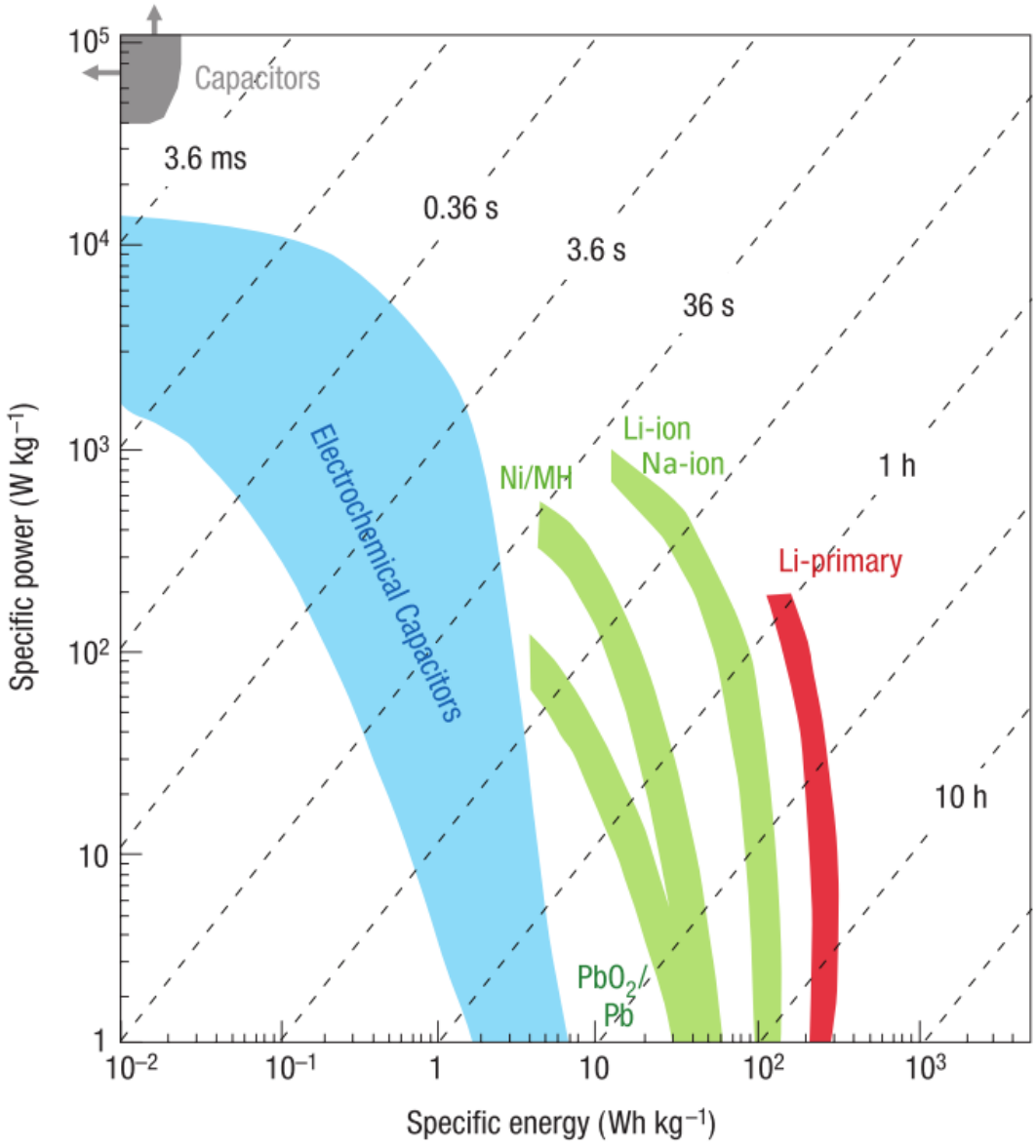

Figure 1: Ragone plot (specific power vs. specific energy) (adapted from (4)).

1.1.1 Batteries

As previously mentioned, there are many different types of batteries, but all batteries store energy through faradaic oxidation-reduction reactions at the electrodes, as described in Figure 2. In these devices, two electrodes, negative and positive, are separated by an ion-conducting and electronic-insulating electrolyte. The oxidation states of the electrode active materials are modified by charge transfer during battery charge and discharge. When the two electrodes are connected, electricity is spontaneously generated (discharge). Oxidation of the active material occurs at the anode during discharge, which generates electrons while reduction continues at the cathode which consumes electrons. The reaction occurs until one electrode has totally reacted. The battery can be recharged by applying an external current, which reverse the reactions. (*18*)

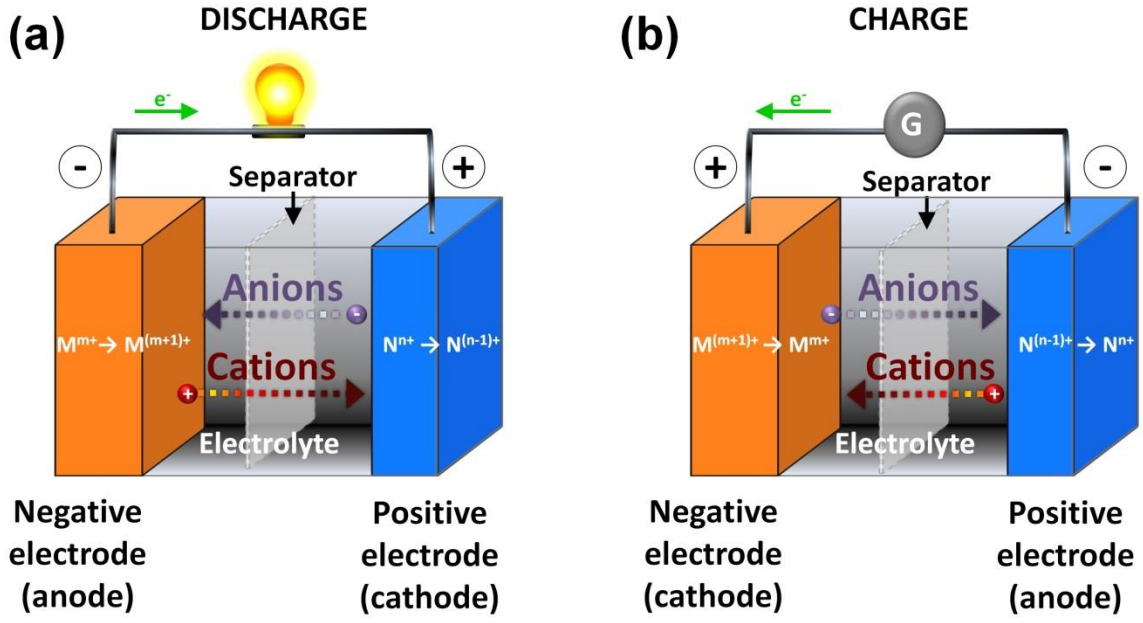

Figure 2: Schematic of a battery during discharge (a) and charge (b).

Each electrode material has a characteristic electrode potential (denoted as E, expressed in V vs. standard hydrogen electrode (SHE)) and capacity (denoted as Q, expressed in mAh/g) determined according to the following equations (*18*) :

$$E = E'^{\circ} - 2{,}3 \times \frac{RT}{nF} log(\frac{\theta}{1-\theta}) \quad (3)$$

$$Q = \frac{nF}{3.6 \times M} \quad (4)$$

Where: E'° is the standard potential of the redox couple (V vs. SHE), F is the Faraday constant (96,485 C/mol), θ is the extent of fractional coverage of the surface of the inner structure, R is the universal gas constant (8.314 J/K.mol), T is the absolute temperature (K), M is the molar mass (g/mol) and n is the number of moles of electrons transferred.

In terms of electrochemical characterization, the behavior of a battery-type material is illustrated Figure 3. The cyclic voltammetry and galvanostatic charge-discharge principles are extensively described in Chapter 2. There are well defined potentials where the oxidation and reduction occurs that are identified by peaks in the cyclic voltammetry and by plateaus in the galvanostatic charge-discharge.

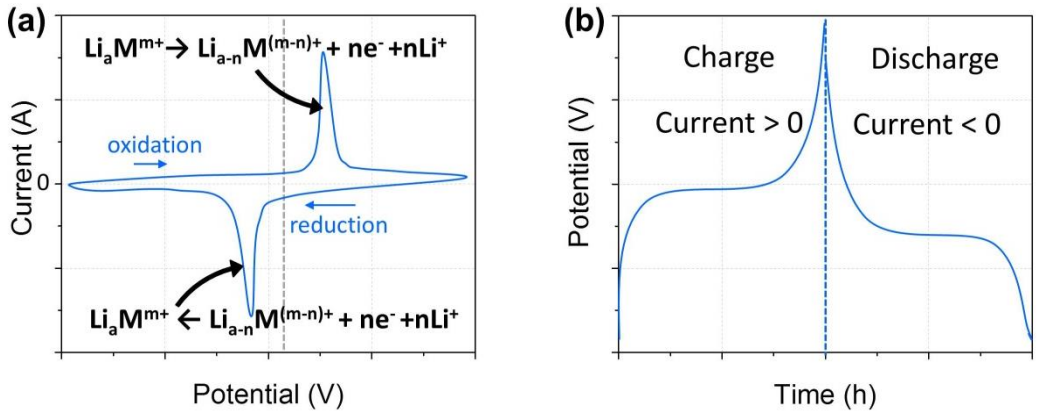

Figure 3: Typical behavior of a lithium-ion battery material during cyclic voltammetry (a) and galvanostatic charge-discharge measurements (b).

Although various commercial battery systems exist based on various chemistries, only lithium-ion and sodium-ion batteries were described, the latter being under development.

1.1.1.1 Lithium-Ion Batteries

Lithium-ion batteries are the most advanced electrochemical energy storage technology in terms of performance (*5*). The advantage of this technology is its low cost, high energy density (>550 Wh/L) and long cycle life (~ 1,000 cycles). Figure 4 is a schematic of a commercial lithium-ion battery. It is composed of graphite as the negative electrode, a $LiCoO_2$ (LCO) positive electrode and 1M $LiPF_6$ as the electrolyte. The reactions occurring at the electrodes are respectively (*19*):

$$C_6 + xe^- + xLi^+ \leftrightarrow Li_xC_6 \quad (5)$$

$$Li_{1-x}CoO_2 + xe^- + xLi^+ \leftrightarrow LiCoO_2 \quad (6)$$

Where x is the number of mole.

These Li^+ intercalation reactions lead to specific capacity up to 165 mAh/g and a voltage of 4.1V. Seen from (1) and (2) both electrodes can host lithium ions. This mechanism is called the rocking chair because the active Li ions are “transported” back and forth between the two electrodes during charge and discharge, as illustrated in Figure 4. This mechanism is specific to ion battery technology and is also observed in sodium-ion batteries (*19-21*).

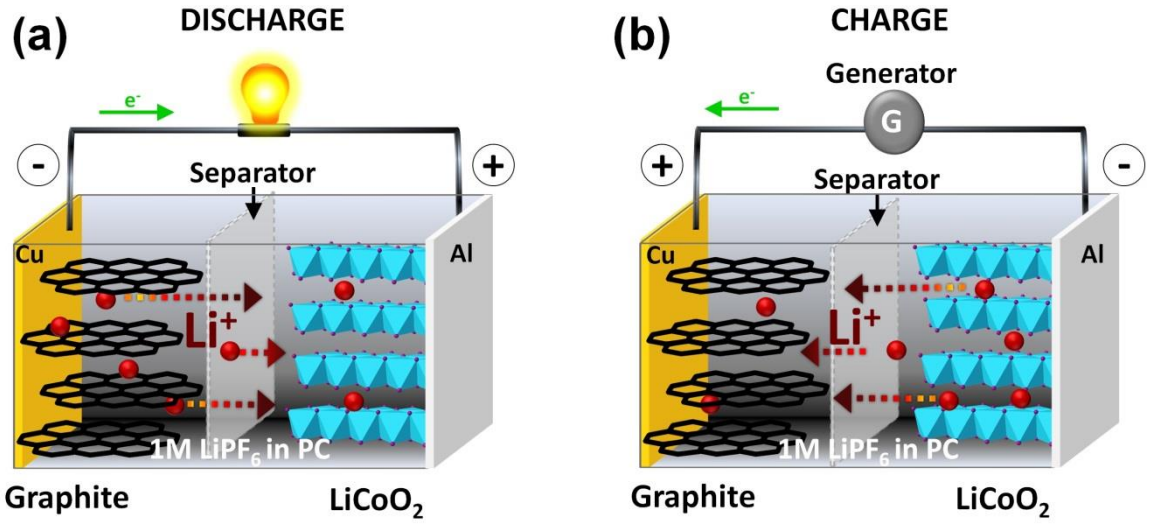

Figure 4: Schematic of a Li-ion battery during discharge (a) and charge (b).

For the past few decades, extensive efforts have been focused on the improvement of materials' capacities. The graphite anode in Li-ion batteries suffers from irreversible capacity loss due to solid electrolyte interphase formation during cycling and has limited energy and power density. In addition, the LCO cathode is expensive, not thermally safe, and has short cycle life and low power density. Figure 5 presents various electrodes proposed in the literature to replace current electrode materials. The main alternatives are; $LiMn_2O_4$ (LMO), $LiNiMnCoO_2$ (NMC) and $LiFePO_4$ (LFP) (*22*, *23*). LMO is safer and has higher power density than LCO but lower energy density and cycle life. NMC has high energy and high power densities however LFP is safer, has longer cycle life and possesses higher power density than all other Li-ion systems, but lower voltage and higher self-discharge (*24*). Materials for lithium-ion battery are not the main focus here but other relevant materials will be presented in the second part of this chapter.

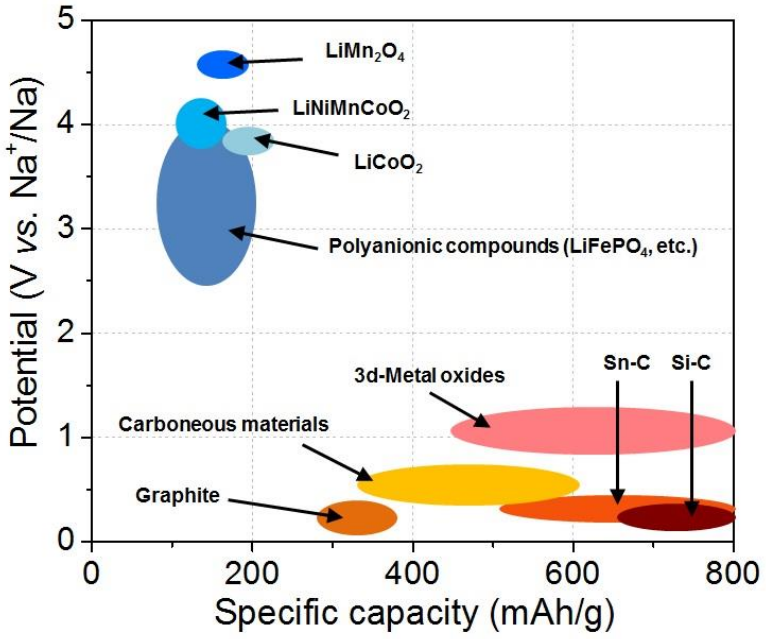

Figure 5: Voltage vs. Capacity of relevant positive and negative electrode materials for lithium-ion batteries (adapted from (1)).

1.1.1.2 Sodium-Ion Batteries

In recent years, there has been speculation concerning lithium reserves and its price (*25*, *26*). The main producers are Talison in Australia, FMC in Argentina, SQM and Rockwood Lithium ion in Chile and Tianqi Lithium in China. An increased demand for lithium is predicted for the next few decades, especially driven by the need for large scale energy storage facilities and electric vehicles. Because lithium is not abundant (Table 1) and the resources are mainly located in emerging countries, it could create political tension and increase the cost of metallic lithium and lithium salts. Even if it is uncertain that a lithium economic crisis will occur, these concerns have driven researchers to study more sustainable alternative energy storage technologies.

Since sodium is one of the most abundant elements on earth and is homogenously distributed (see Table 1), it will not suffer from geopolitical issues (*25-29*). Moreover, the copper current collector that is required in lithium-ion batteries can be replaced by cheaper aluminum current collectors. Beside these advantages, it is important to know that the technology used in Li-ion batteries and Na-ion batteries are very similar. This has renewed the interest in the development of Na-ion technology (*30-34*). The advancement of Na-ion batteries faces several intrinsic challenges. First, the redox potential of Na^+/Na is higher than Li^+/Li, reducing the operating voltage. Then, the ionic radius is larger, meaning that many materials cannot reversibly host it (for example graphite), it can cause higher volumetric change, and reduce the ionic conductivity and diffusion. Because of these drawbacks, the first Na-based system that was developed in the 90's had been disregarded until recently (*20, 21, 35-38*).

Table 1: Comparison of the properties of lithium and sodium.

	Li	Na
Abundance in Earth'crust	20 ppm	23 000 ppm
Average world production	24 600 tons	281 800 000 tons
Specific capacity	3860 mAh/g	1160 mAh/g
Redox potential	-3.045 V *vs.* SHE	-2.714 V *vs.* SHE
Ionic radius	$0.76\ 10^{-10}$ m	$1.02\ 10^{-10}$ m

One of the challenges that sodium-ion batteries are facing is the limited number of suitable negative electrode materials. Graphite is the most commonly used negative electrode in Lithium-ion batteries. It has numerous advantages, such as a very competitive cost and reasonable capacity of 372 mAh/g. Although Na-ion technology is similar to that of Li-ion, unfortunately Na-ions do not intercalate into graphite (*27-29*). Several alternatives have been studied, ranging from carbon materials to alloys. The most notable anode materials, Hard carbon and $NaTiO_2$, are discussed here. A comparison between the different electrodes is shown at the end of this part in Figure 7.

Hard carbon, amorphous carbon synthesized by oxidation then carbonization under neutral flow, was proposed as a negative electrode for sodium-ion batteries as early as 2000 by Dahn *et al*. (*39*). It was later studied and improved by several independent groups, notably in 2002 by Thomas *et al.* (*40*), by Komaba in 2011 (*41*) and finally by Ponrouch *et al.* in 2013 (*42*). The latter investigated the effect of the synthesis method to optimize the surface area, porosity, particle size and the degree of graphitization in order to obtain the best electrochemical performance, as shown in Figure 6. Specific capacities up to 326 mAh/g at C/10 rate (10 hours discharge) with excellent capacity retention (>100 cycles) and excellent rate capability, 230 mAh/g at 1C rate (1 hour discharge), were achieved by hard carbon prepared through relatively cheap pyrolysis of sugar. These results were comparable to graphite in lithium-ion battery.

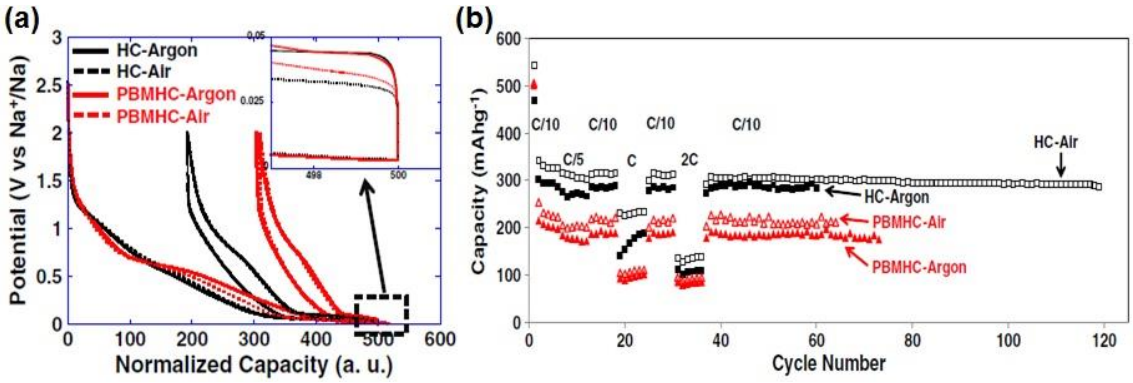

Figure 6: Electrochemical performance of hard carbon with different synthesis methods cycled in 1M $NaClO_4$ in EC:PC vs. metallic Na: first cycle galvanostatic charge-discharge curves (a) and capacities *vs.* cycle number (b) (adapted from (*42*)).

The other relevant negative electrode materials were early transition metal oxides, in particular Ti-based intercalation compounds, such as $NaTiO_2$ and $Na_2Ti_3O_7$. Xiong *et al.* showed promising results obtained from large $NaTiO_2$ nanotubes (lateral dimension >80 nm) (*43*). Capacity improved from 70 to 150 mAh/g after 15 cycles at C/3 rate (3 hours discharge) when cycled between 1V and 2.5V vs Na^+/Na. This was attributed to the fact that Na ion concentration on the surface was increasing upon cycling and suggested the need for pre-cycling a cell, in some cases limiting commercial interest. Senguttuvan *et al.* reported on $Na_2Ti_3O_7$ which is a very low voltage insertion compound (between 0.2 and 0.4 V vs. Na^+/Na) (*44*). A capacity of about 200 mAh/g at a low rate (C/25 rate, 25 hours discharge) was measured, corresponding to the insertion of 2 Na ions. But these electrochemical systems suffer from low rate capability and cycle life.

Numerous studies have been done on cathode materials for lithium-ion battery and this is the reason most of the cathode materials proposed for sodium-ion batteries are the

sodiated counterpart of the well-studied layered transition metal oxides, olivines and compounds with the NASICON (Natrium super ion conductor) framework.

Early research on transition metal oxides containing sodium, Na_xMO_2, was done in the 80's by Delmas *et al.* (*45*). It was demonstrated that reversible insertion/deinsertion was feasible and therefore extensive research on such structure has been done. The most studied metal oxides are Na_xMnO_2 and Na_xCoO_2 based materials (*46-52*). In these systems, capacities up to 140 mAh/g at slow rates were obtained, but on a large 2-3.8V potential range numerous two-phase transition steps were observed which is undesirable for real devices.

Olivine structured-materials have been studied extensively for lithium-ion batteries, most notably $LiFePO_4$ (*53*). Its sodium based analog, $NaFePO_4$, has logically been proposed (*54-57*). Although the capacities obtained, 125 mAh/g at C/20 rate, were comparable to the capacity obtained with $LiFePO_4$ in a lithium-ion battery (150 mAh/g) the same drawback associated with low potential was present.

The NASICON, or Natrium super ion conductor, is a family of 3D structures with good structural stability and fast ion conduction. Several member of this family have been investigated, such as $NaTi_2(PO_4)_3$, $NaNbFe(PO_4)_3$, $Na_2TiFe(PO_4)_3$, $Na_2TiCr(PO_4)_3$, and $Na_3V_2(PO_4)_3$ (*35, 58-60*). Recently the effort focused on carbon-coated $Na_3V_2(PO_4)_3$ with a demonstrated capacity of up to 240 mAh/g when cycled between 3.8V and 1.5V at C/12.5 rate but a potential plateau at 1.6V vs Na^+/Na was observed, which is neither cathodic nor anodic, and therefore not suitable for commercial application (*60-64*).

Another important part of a battery is the electrolyte (41, 47, 65, 66). The most common electrolyte formulations found in the literature are similar to those used in

lithium-ion batteries, replacing Li^+ ions with Na^+: $NaPF_6$ or $NaClO_4$ salts are dissolved in carbonate ester solvents such as propylene carbonate, ethylene carbonate or diethyl carbonate. The formation of the solid electrolyte interphase (SEI) in sodium-ion batteries has been less investigated than in lithium-ion batteries. It appeared that the SEI is not stable and homogeneous in these electrolytes, causing Coulombic inefficiency. Here also research efforts on electrolyte additives to stabilize the SEI have been inspired from the Li-ion battery field. Ponrouch et al., proposed the addition of fluoroethylene carbonate (FEC) to stabilize the SEI film at the negative electrode and results showed an improved cycling capacity (65). Deeper understanding of the SEI formation and solvent formulation will have to be performed to further improve the performance of sodium-ion batteries, however, it is not the focus of this thesis.

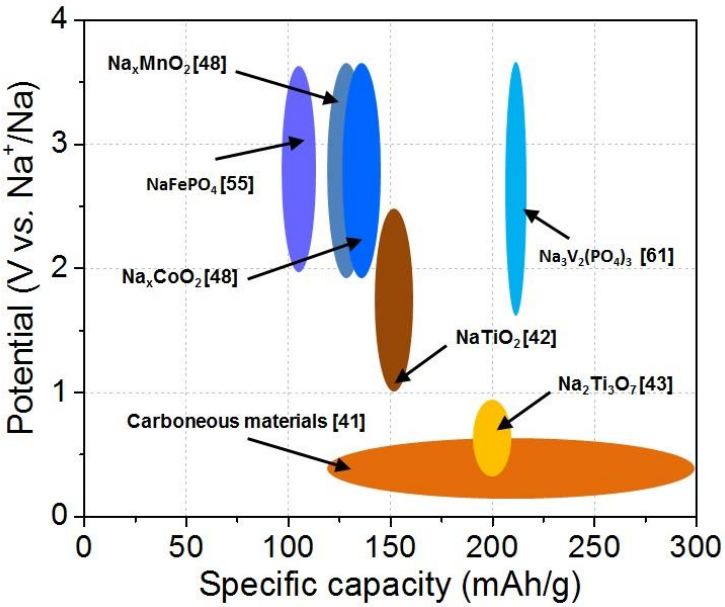

Figure 7: Voltage vs. Capacity of relevant positive and negative electrode materials for sodium-ion batteries. All materials can be found in the text.

1.1.2 Supercapacitors

Supercapacitors, also called electrochemical capacitors or electrical double layer capacitors, consist of two electrodes separated by a separator soaked with electrolyte (*67*). Different from batteries, supercapacitors have high power densities, excellent rate capability and almost infinite cycle life. Supercapacitors can store energy through two fast-kinetic charge storage mechanisms: double layer capacitance and pseudocapacitance (*3, 4, 68*). The difference between these two mechanisms will be described in the following sections.

1.1.2.1 Double Layer Capacitance

The double-layer capacitance is caused by electrostatic separation of the charges at the electrode / electrolyte interface when a potential is imposed, as described in the simplified schematic shown in Figure 8. Several models have been developed to describe the double layer successively by Helmholtz (1853) (*15*), Gouy and Chapman (1913)(*69*), Stern (1924), Grahame (1947) (*70*), and Bockris, Devanthan and Muller (1963).

The Helmholtz model described the double layer as two layers of opposite charge accumulated at the electrode/electrolyte interface and separated by the radius of the solvated ion. The Gouy-Chapman model described a diffuse model of the double layer, due to thermodynamic distribution of counter-ions from the electrolyte. The Stern model represented in Figure 8.b combined both models and considered that the charge compensation occured within a volume of electrolyte defined by the thickness d of the diffusive layer. The layer of charge in the electrolyte near the interface was in fact composed of several layers. Right next to the negative electrode there was the compact

layer or Helmoltz layer at the distance of the partially desolvated and solvated cation radius and then the Gouy-Chapman diffusive layer.

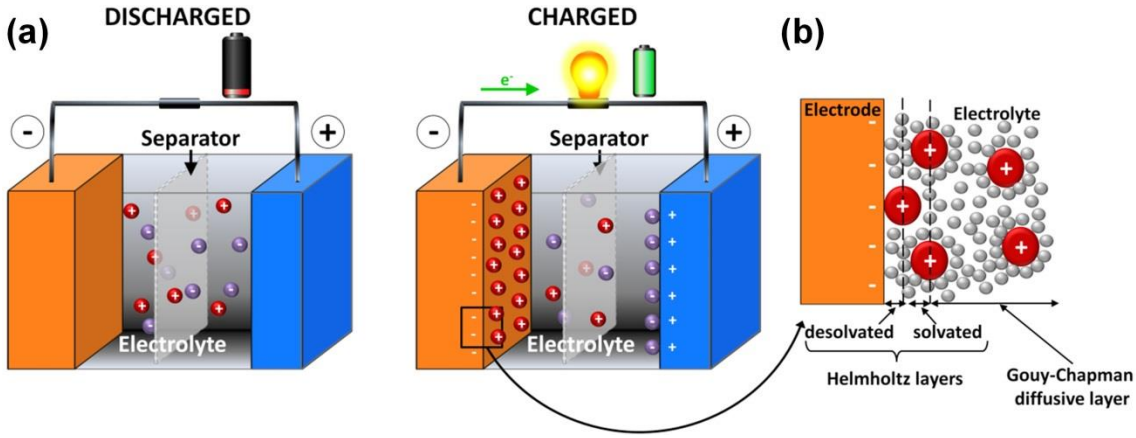

Figure 8: Schematic of an electrochemical double layer capacitor (a) and the Stern model (b)

The capacitance can be described as the association of the Helmoltz capacitance and Gouy-Chapman capacitance in serie:

$$\frac{1}{C_{dl}} = \frac{1}{C_{Helmoltz}} + \frac{1}{C_{Gouy-Chapman}} = \frac{d}{A\varepsilon_r\varepsilon_0} + \frac{1}{A\varepsilon_r\varepsilon_0\kappa_D} \quad (7)$$

Where: C_{dl} is the double layer capacitance (F) of the electrode, A is the electrode surface area (m^2), ε_r is the relative dielectric constant, ε_0 is the permittivity of a vaccum ($8.85\ 10^{-12}$ F/m), d is the approaching distance of the ions (m) and κ_D is the Debye length (m) or $1/\kappa_D$ is the diffusion length of the Gouy-Chapman layer. In concentrated electrolyte, like in this work, $1/\kappa_D$ tends to 0. Thus, the double layer capacitance is defined by the Helmholtz capacitance.

As described in Figure 8.a, there are two electrodes facing each other. Therefore the total capacitance of the cell can be described as the combination of the two electrode capacitances in series and is given by the following equation:

$$\frac{1}{C_{Cell}} = \frac{1}{C_{+}} + \frac{1}{C_{-}} \tag{8}$$

The electrochemical responses of an ideal supercapacitor are shown Figure 9. In contrast to batteries, the storage mechanism does not occurs at a specific potential, thus no plateaus or peaks are present. The current response to a linear voltage sweep in cyclic voltammetry has a rectangular shape corresponding to equation 9.

$$I = C\, {dV}/{dt} \tag{9}$$

Where, I is the current (A), C is the capacitance (F), V is the potential (V) and t is the time (s). Further characteristics of the electrochemical measurement methods will be described in Chapter 2.

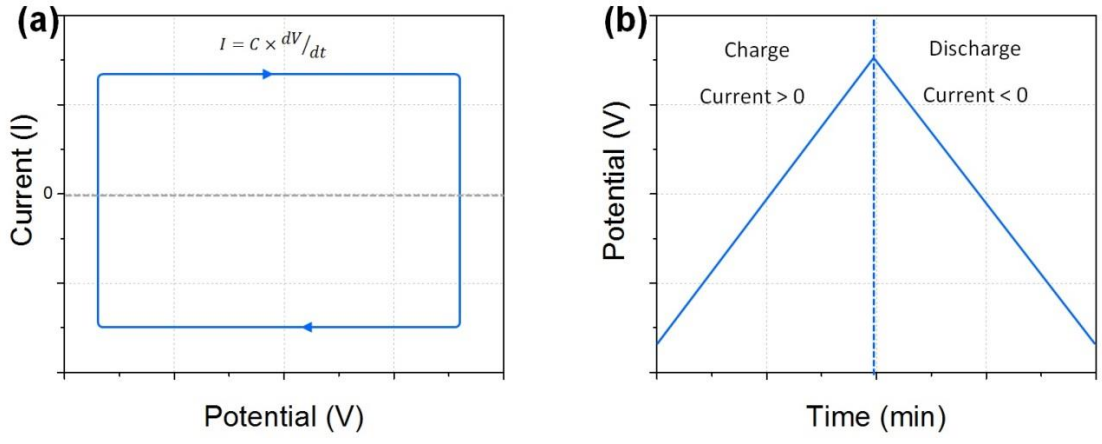

Figure 9: Typical behavior of electrochemical double layer capacitors during cyclic voltammetry (a) and galvanostatic charge-discharge measurements (b).

The electrode materials must exhibit high electrical conductivity and high specific surface area. The best candidates are carbon materials, such as carbon nanotubes, graphene sheets and activated carbon (*71-74*). They have a large electrochemical stability voltage window in addition to their high electric conductivity and their high specific surface area. The most conventional materials used are activated carbons thanks to their good properties and low cost. Activated carbons are synthesized from biomass (coconut shells, wood, etc.) by carbonization at temperatures lower than 800°C in an inert atmosphere, then treated in a process called activation, consisting of a physical method (steam, etc.) and/or chemical treatment (strong bases, etc.), in order to enhance the porosity (*75*). Table 2 summarizes the properties of these materials:

Table 2: Comparison of the electrochemical performances of different carbon materials (adapted from (*74*)).

		Specific Capacitance (F/g)	
	Specific surface area (m^2/g)	In 1M H_2SO_4	In organic electrolyte
Activated carbon	2000 - 3000	300	240
Carbide derived carbon	1300 - 2500	200	170
Carbon nanotubes	300 - 1000	150	90
Onion-like carbon	550	40	38
Graphene	300 - 3000	280	170
Carbon aerogels	400 – 1000	100	80

Kotz demonstrated that when increasing the specific surface area above 1500 m^2/g, the capacitance reached a limit of about 100 F/g (*76*). Another significant parameter is the pore size distribution and the electrode-electrolyte interface. Chmiola *et al.* (*77*) controlled the pore size distribution of a carbide-derived carbon (CDC) by controlling the synthesis temperature and demonstrated the importance of these parameters on the electrochemical performance. An unprecedented increase in capacitance was observed for pore sizes smaller than 1 nm, which was attributed to ion de-solvation observed when the average pore size corresponded to the ion size (*78, 79*).

1.1.2.2 Pseudocapacitance

The electrochemical behavior, such as the current response of a potential change, of a pseudocapacitor is similar to double layer capacitors. The distinction comes from the energy storage mechanism as double layer capacitance occurs through electrostatic interaction whereas pseudocapacitance is due to electron-transfer reactions (*16, 17, 80*). Therefore, higher energy densities can be achieved using pseudocapacitive materials. However, it can also be distinguished from faradaic reactions occurring in batteries for two main reasons: the faster charging time and the linear dependence of the charge stored with the potential window.

Conway described pseudocapacitance as one of the three faradaic mechanisms described in Figure 10 that can exhibit capacitive electrochemical behavior. The first case is underpotential deposition, which is metal ions forming an adsorbed monolayer at a different metal surface above their redox potential. The second case is redox capacitance, which is the electrochemical adsorption of ions onto the surface or near surface of a material with a concomitant faradaic charge-transfer. The third case is intercalation

capacitance, which is the faradaic intercalation of ions into tunnels or layers of electrode materials. It is worth noting that some battery-type materials can exhibit this behavior thanks to tuning the engineering of the electrodes; usually using thin film technology or nanometric particle synthesis to achieve pseudocapacitve behavior (*16*, *81*). These materials are called extrinsic pseudocapacitive materials because their bulk counterparts do not behave as supercapacitor type materials, as opposed to intrinsic pseudocapacitive materials that behave similar to double layer capacitors regardless of the particle size.

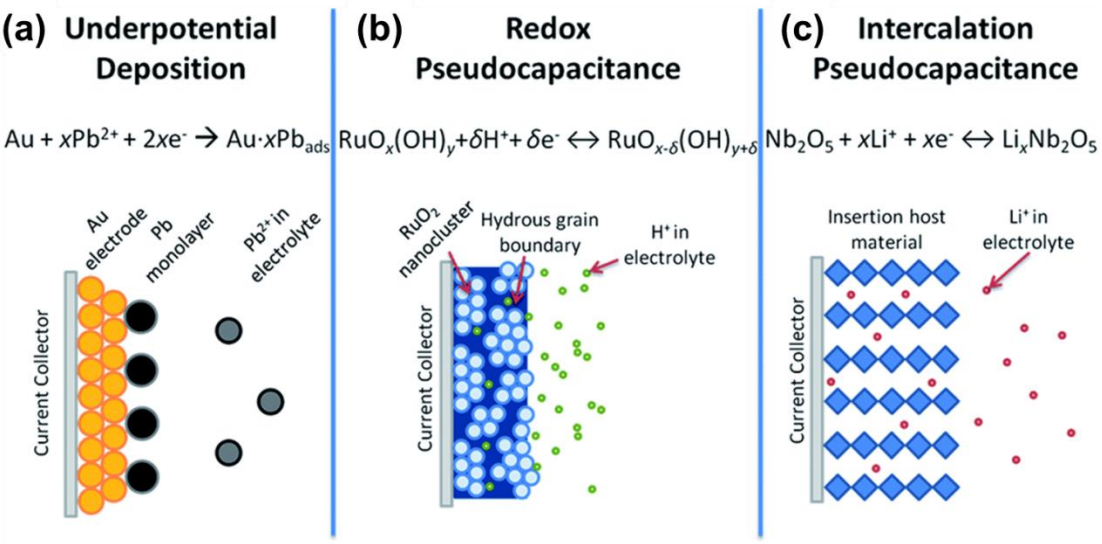

Figure 10: Different types of reversible redox mechanisms that give rise to pseudocapacitance: underpotential deposition (a), redox pseudocapacitance (b) and intercalation pseudocapacitance (c) (adapted from (*16*)).

Since pseudocapacitive electrodes store energy through faradaic reactions, the capacitance (C) can be expressed by equation 10.

$$C = \left(\frac{nF}{M}\right)\frac{\theta}{E} \tag{10}$$

Where, C is the specific capacitance (F/g), n is the number of electrons, F is the Faraday constant (96,485 C/mol) and M is the molecular weight of the active material (mol/g). This induces an infinite apparent redox potential next to each other and the potential (E) responds linearly with the extent of fractional coverage of the surface of the inner structure or the advancement of the reaction (θ).

This translates as mirror image voltammograms and a triangular galvanostatic charge-discharge curve, as illustrated in Figure 11. In other words, the capacitive behavior of pseudocapacitive electrodes results from fast, successive, indistinguishable, and reversible redox reactions occurring at the surface, which are not limited by diffusion (*82*).

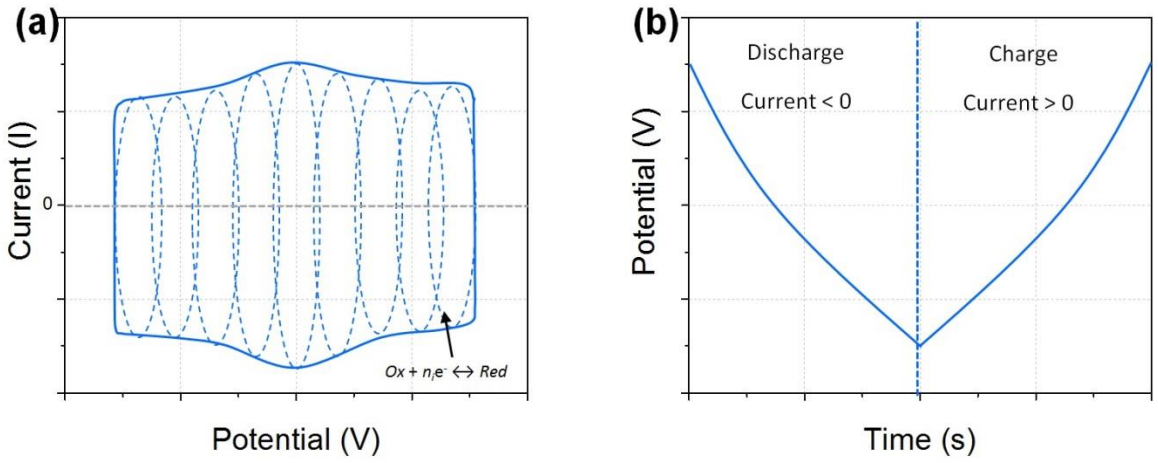

Figure 11: Typical behavior of pseudocapacitive materials during cyclic voltammetry (a) and galvanostatic charge-discharge measurements (b).

Transition metal oxides, such as MnO_2, RuO_2, Co_2O_3, TiO_2 and V_2O_5 were the first materials investigated for pseudocapacitors (*16*). The most studied is RuO_2 because regardless of its high cost it has the highest conductivity and three stable oxidation states

occurring on a 1.2V potential range (*83-87*). When cycled in sulfuric acid the reaction noted in Figure 10.b occurs. Figure 12 shows the voltammograms obtained for different potential ranges and highlights the pseudocapacitive behavior of RuO_2 as the broad anodic and cathodic peaks are symmetrical. First results using RuO_2 showed capacitance up to 720 F/g (*87, 88*).

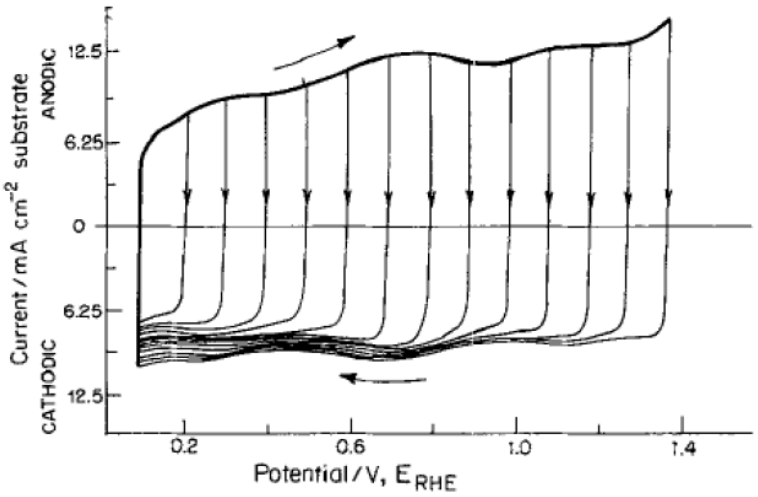

Figure 12: Cycle voltammetry of RuO_2 in H_2SO_4 at 50 mV/s (adapted from (*3*)).

Other metal oxides have been studied, in particular MnO_2 because of its low cost, resource abundance, environmental friendliness and high theoretical capacitance (*89*). Capacitance up to 260 F/g was obtained in 0.5M K_2SO_4 (*90*). Because of the low electronic conductivity of oxide materials, the preparation of composites using a carbon matrix was proposed to benefit from better electric conductivity as well as higher specific surface area. In the second part of this chapter, results reported with graphene-based composites are analyzed.

1.1.2.3 Electrolytes

The electrolyte is a key factor in the electrochemical performance of a supercapacitor (*91*). The energy and power are proportional to the square of the potential window (equations 1 and 2). Therefore research has focused on formulating electrolytes with large potential window stability. There are three types of liquid electrolytes: aqueous electrolytes, organic electrolytes, and ionic liquids. The ionic conductivity, the temperature stability and the compatibility with the electrode are also important factors. Table 3 summarizes the properties of these electrolytes and it falls to the engineer to select the best electrolyte corresponding to the desired application.

Table 3: Properties of electrolytes (adapted from (*71, 91, 92*)).

	Potential window stability (V)	Conductivity (mS/cm)	Temperature stability (°C)
Aqueous	< 1.2	>400	-20 to +50
Organic	< 3	<100	-40 to +80
Ionic Liquid	< 6	<15	-100 to +400

Ionic liquids, which are room-temperature solvent-free electrolytes, show the largest potential window and temperature stability. However they have lower conductivity which reduces power density. Two of the most conventional ionic liquids used are EMITFSI (1-ethyl-3-methylimidazolium bis(trifluoromethylsulfonyl)imide) and EMIBF4 (1-ethyl-3-methylimidazolium tetrafluoroborate). Organic electrolytes are typically

solutions of tetraethyl ammonium salts dissolved in acetonitrile (ACN) or propylene carbonate (PC).

Aqueous electrolytes suffer from reduced potential window limited by the electrolysis potentials of water. Nevertheless, they are the most used electrolytes thanks to safety, convenience, high conductivity, low cost and good compatibility with most electrode materials, in particular with pseudocapacitive electrodes. Figure 13 shows example of the behavior of an activated carbon in various electrolytes. In all cases, rectangular shaped cyclic voltammograms were obtained; however the operating potential ranges and resistances were different and will be explained later.

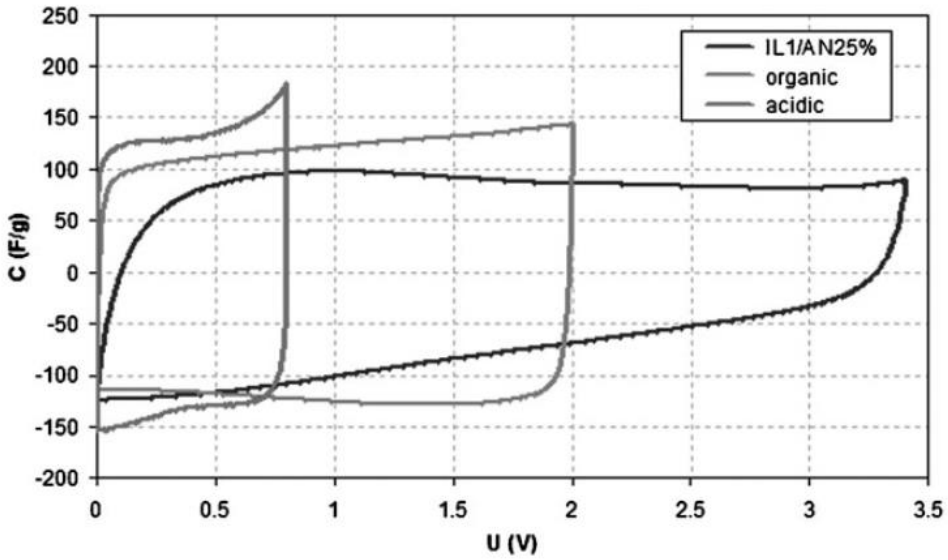

Figure 13: Cyclic voltammetry of activated carbon at 5 mV/s in different electrolytes (adapted from (*93*)).

1.1.2.4 Hybrid Capacitors

The principle of a hybrid between electrochemical capacitors and batteries was first introduced by John Miller (*94*). Hybrid capacitors combine an electrochemical capacitor electrode with a battery electrode. As the battery-type electrode potential is mostly constant during the charge-discharge cycle (plateau), the total cell potential behaves like the supercapacitor electrode, that is, the cell potential varies linearly with time during constant charge-discharge cycles, as described in Figure 14. The objectives of these systems are to deliver higher energies than supercapacitors at higher power density than batteries (*95, 96*), by increasing the average discharge voltage and the cell capacity. In other words, hybrid capacitors are promising energy storage devices that bridge the gap between batteries and supercapacitors on the Ragone plot (Figure 1).

The capacitance of a hybrid cell is described by equation 11. In the case of a symmetric supercapacitor the cell capacitance can be expressed as half the capacitance of an electrode ($C_{cell} = C_{EC+,-}/2$). Whereas in the case of an asymmetric hybrid capacitor, the capacitance of the faradaic electrode ($C_{faradaic}$) is greatly superior to the capacitance of the capacitive electrode (C_{EC}) and the total cell capacitance is expressed as follow:

$$\frac{1}{C_{cell}} = \frac{1}{C_{EC}} + \frac{1}{C_{Faradaic}} \quad \Leftrightarrow C_{total} \approx C_{EC} \tag{11}$$

Therefore the total capacitance in a hybrid capacitor cell would be twice the capacitance of a symmetric electrochemical double layer capacitor. Depending of the choice of the faradaic electrode, the cell voltage can be greatly increased. However, using a faradaic electrode also comes with a limitation in the rate capability and cycle life because of the presence of a battery-like electrode.

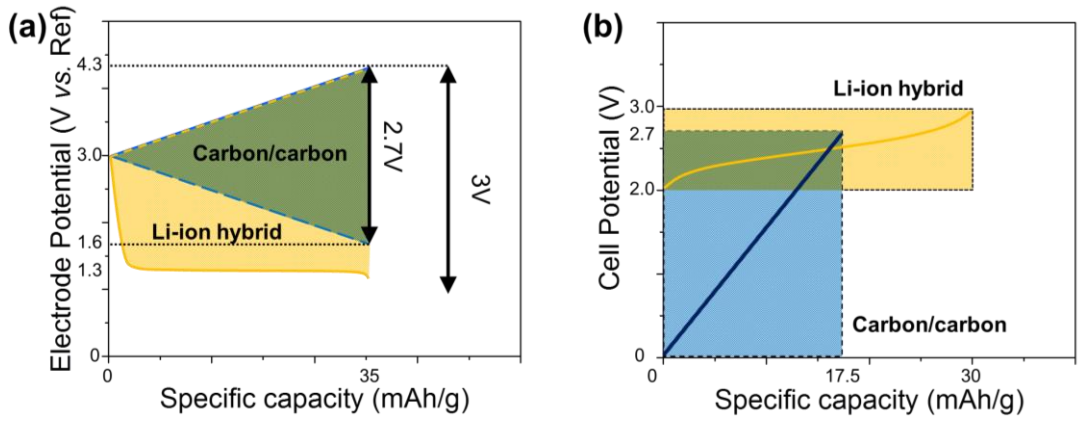

Figure 14: Electrode potentials vs. specific capacity of each electrode in a symmetric carbon/carbon supercapacitor and an asymmetric Li-ion hybrid during charging (a). Cell potential vs. specific capacity based on the total mass of the two electrodes (b).

Several hybrid systems have been investigated. In aqueous electrolytes the most extensively systems studied are: Carbon/NiOOH in KOH (*97*), Carbon/PbO_2 in H_2SO_4 (commercial)(*98*) and MnO_2/Carbon in K_2SO_4 (*99*). Although these systems are interesting, this thesis will focus only on hybrid capacitor in organic electrolytes that are lithium-ion capacitors and sodium-ion capacitors since these systems have larger voltage windows and show the best performance in terms of power and energy density.

Li-ion capacitor systems combine the high energy density from the lithium-ion intercalation electrodes of batteries and the high power of supercapacitor electrodes. The electrolytes used are lithium salts in carbonate-based organic solvents, similar to electrolytes used in lithium-ion batteries. Due to their high energy and power densities, they are intended for use in a wide variety of applications, such as transportation (electric and hybrid cars), electronics (telephones and laptops), and storage of renewable energy. Several companies have started to commercialize their devices, such as ACT, JM Energy Corp., Ioxus, Asahi Kasei FDK Energy, Aowei and TAIYO YUDEN Co (*96*).

Amatucci *et al.* were the first to propose a non-aqueous hybrid device in 2001 (*100*), with two systems: activated carbon/$Li_4Ti_5O_{12}$ (LTO) and activated carbon/WO_2 in a 1M $LiBF_4$ in acetonitrile. The most interesting is the former because LTO has several advantages including high coulombic efficiency (≈100%), high theoretical capacity (175 mAh/g), safe cycling with a redox plateau potential at 1.55 V vs. Li^+/Li (above solid electrolyte interphase formation), small volumetric changes and low cost. Such devices reached up to 18 Wh/kg (*101*). Figure 15 shows the first results published by Amatucci *et al*. Later this system's power performance was greatly improved by Naoi *et al*. using a nanocomposite between carbon nanofibers and nano-crystal of LTO synthesized by ultracentrifugation (*102, 103*). This process solved the problem of the low conductivity of LTO. Excellent high rate performances were obtained with up to 40 mAh/g at 1200C rate (3 seconds discharge) as well as excellent cycle life. Activated carbon was still used as the positive electrode thanks to its suitable properties discussed earlier, and counter anion of the electrolyte can form double layer capacitance at its surface.

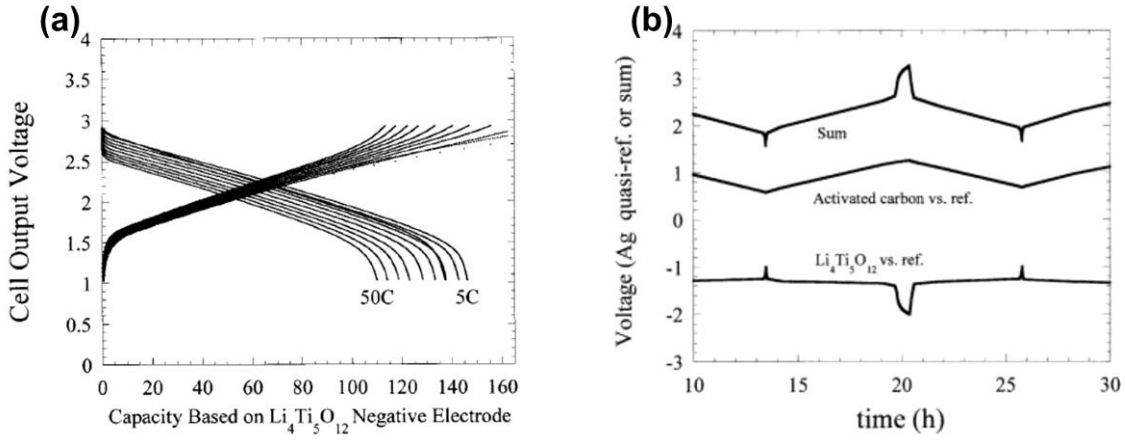

Figure 15: Discharge profile as function of rate (a) and three-electrode measurements (b) of an asymmetric hybrid cell utilizing an activated carbon positive electrode and $Li_4Ti_5O_{12}$ negative electrode in $LiPF_6$ EC/DMC electrolyte (adapted from (*100*)).

With graphite and activated carbon respectively being the most used electrodes in batteries and supercapacitors, asymmetric hybrid devices combining these two materials were proposed (*104*). The graphite needs to be pre-lithiated because of the formation of the solid electrolyte interphase and lithium-ion consumption that decrease the conductivity during the first lithiation. The advantage of pre-lithiated graphite/activated carbon system compared to LTO/AC is that graphite has a higher specific capacity and low intercalation/deintercalation potential (0.1V vs Li^+/Li) extending the cell operating voltage range. This system has been commercialized by JMEnergy since 2008, with cells that claim capacities of 2200F and power densities up to 10 kW/kg but energy densities limited at 10Wh/kg (*105*).

However, the limited supply of lithium and quickly widening use of energy storage devices justify replacement of lithium with a cheaper and more abundant element. For the same reason that sodium-ion batteries emerged as an alternative to Li-ion batteries,

sodium-ion capacitors , where the Li intercalation electrode is replaced with a low cost Na ion electrode were proposed (*106-109*). In 2012, Kuratani *et al*. investigated Hard carbon/activated carbon sodium-ion capacitors and showed the feasibility of such systems (*107*). Similar to Lithium-ion capacitors and sodium-ion batteries, most of the ongoing work on Na-ion capacitors is focused on the development of negative electrodes and several anodes have been proposed, such as hard carbon, carbon nanotubes, $NiCo_2O_4$ and sodium titanate nanotubes.

1.2 Relevant 2D Materials for Energy Storage

High power densities can only be reached if the energy storage mechanism is either an electrostatic interaction at the electrode / electrolyte interface or fast surface redox reaction. Therefore, bulk materials containing inactive volumes that do not participate in charge storage are inappropriate candidates. In a 2D material, all the active material is directly in contact with the electrolyte as the single sheets of the material are only a few nanometers thick. Moreover, 2D materials have also attracted attention as promising electrode materials since graphene has excellent electrical conductivity, has similar surface area to activated carbon and can be use without an insulating binder (*110*). This thesis focuses on a new family of 2D materials called MXenes. Before describing the state-of-the-art MXenes, other relevant 2D materials for energy storage will be introduced.

1.2.1 Graphene

Among 2D materials, graphene is by far the most famous and the most extensively studied since A. Geim and K. Novoselov characterized isolated graphene sheets in 2004 (results for which the two authors won the Nobel Prize in Physics in 2010) (*111*). It consists of a few layers of carbon with a graphitic structure that has an excellent theoretical electric conductivity, high charge carrier mobility, high specific surface area, high transparency, high flexibility and great mechanical strength (*111-114*). These properties are very interesting for many applications, including energy storage. Recently, graphene electrodes were prepared for supercapacitors and lithium-ion batteries.

1.2.1.1 Graphene for Supercapacitors

As mentioned, graphene has a very high specific surface area ($SSA_{theoretical}$ = 2630 m^2/g) corresponding to a maximum theoretical capacitance of 550 F/g, one of the highest among carbon materials. Therefore many attempts to use graphene as an electrode material in supercapacitors have been attempted that have been more or less successful (*114-121*). Zhu *et al.* used microwaved exfoliation of graphene oxide activated in KOH with an apparent specific surface area of 3100 m^2/g. Performances in several electrolytes were investigated and capacitances up to 166 F/g were obtained in organic electrolytes ($BMIMBF_4$) with good cycle life but resistive voltammograms compared to activated carbons (*118*). El-Kady *et al.*, developed a laser scribing technique to prepare few micrometer thick graphene, obtaining a graphene specific surface area of 1520 m^2/g. The authors used a polymer gel electrolyte (PVA-H_3PO_4) to assemble an all solid supercapacitor and tested the flexibility of the cell, as described in Figure 16. The performances at different angles demonstrated the feasibility of flexible supercapacitors

that have many potential applications such as wearable electronic. Other electrolytes were used to increase the potential range and capacitance up to 276 F/g were obtained in an $EMIMBF_4$ ionic liquid with a potential range of 3.5V. The limitation here lies in the small areal capacitance (<5 mF/cm²) due to the use of thin film.

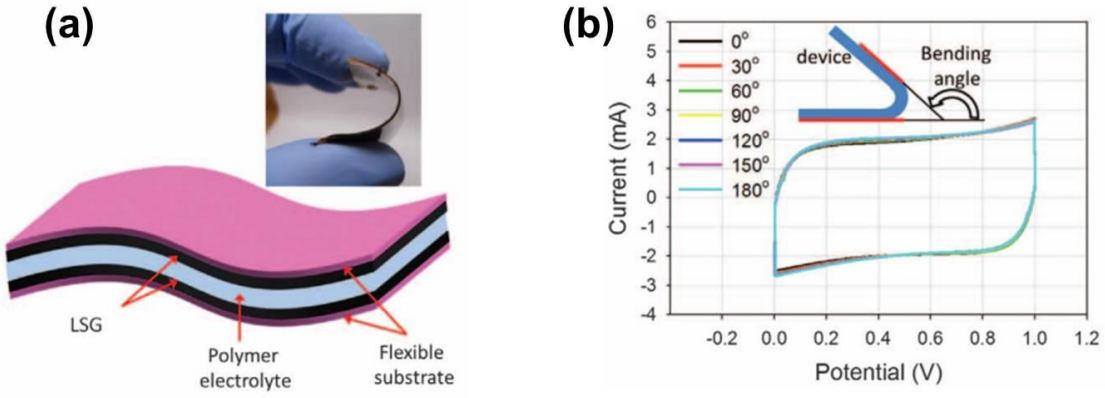

Figure 16: Design of a flexible supercapacitors based on laser-scribed graphene. (inset) A digital photograph showing the flexibility of the device (a) Cyclic voltammograms and the effect of the bending at 1000 mV/s (b) (adapted from (*119*)).

1.2.1.2 Graphene for Lithium-Ion Batteries

Keeping in mind that graphite is the most commonly used negative electrode in lithium-ion batteries, graphene has still attracted a great deal of attention for lithium-ion batteries. The theoretical capacity of graphene is 744 mAh/g (twice that of graphite) corresponding to two layers of lithium on both sides of the graphene sheet. Many research teams currently investigate graphene for lithium-ion batteries, both experimentally and theoretically (*120, 122-129*). However, the storage mechanism is still

not fully understood, in particular the diffusion of lithium and the effect of defects on performance.

The first investigations by Yoo *et al.* showed a capacity of 540 mAh/g for graphene sheets prepared by reduction of graphene oxide and later improved to 650 mAh/g for thinner graphene. These capacities were higher than for graphite and supported the hypothesis that lithium could be adsorbed at the graphene surface. The authors added C60 to further increase the capacity up to 784 mAh/g. Graphene prepared by other synthesis routes led to different results, highlighting the effects of the synthesis method used.

However, graphene is facing major obstacles if it is to be used as the negative electrode for lithium-ion batteries (*120*). First, there are no plateaus during galvanostatic charge-discharge which are necessary for a stable discharge voltage. Second, the solid electrolyte interphase formation and reaction with functional groups during the first cycle are responsible for a significant degree of irreversibility during the first cycle (*124*). Third, the rate capability is poor because of the limited lithium diffusion in stacked graphene layers.

1.2.2 Graphene Composites

1.2.2.1 Graphene Composites for Supercapacitors

Metal oxides, presented earlier as materials for supercapacitor, store the energy through pseudocapacitance (fast reversible redox reactions). The low electrical conductivity of most oxides and of doped polymers limits their electrochemical performance. Composite materials using good electric conductors, such as carbon nanotubes or carbon black, were investigated early on and recently graphene composites

have been proposed. Another factor to improve the performance is the use of nanomaterials, because the fast redox reactions that occur at the surface of the electrode and the inner part is not active. Therefore, nanomaterials benefit from increased specific surface area, shorter diffusion and reduced charge transfer length (*117*).

Metal oxide/graphene composites have also been proposed (*117, 130-132*). MnO_2/graphene nanosheet composites were synthesized and exhibited good conductivity, good capacitance (310 F/g), good cycle life (95% retention after 15,000 cycles) and good rate capability. Ni(OH) was synthesized *in-situ* on graphene sheets and exhibited capacitances up to 935 F/g. Similar techniques were used for the synthesis of $CoOH_2$/graphene composite and led to 972 F/g.

However, despite graphene composites showing higher capacitance than graphene thanks to the redox reactions, insulating materials reduce the conductivity and the composites have lower cycle life and rate capability than their pure graphene counterpart. More work is ongoing to find new synthesis routes and balance between these different factors.

1.2.2.2 Graphene Composites for Lithium-Ion Batteries

As mentioned earlier, many other electrodes with higher capacity than graphite have been proposed. Some have intrinsic drawbacks such as a large volume change during cycling (Sb, Sn and Si) or a poor electrical conductivity (metal oxides). Therefore, mixing these materials with carbon materials (including graphene) was considered to be a solution.

The electrode materials commonly used in lithium-ion batteries (Co_3O_4, Fe_2O_3, TiO_2, SnO_2, $LiFePO_4$, etc.) were investigated for graphene composites on a order to improve

their conductivity and rate capability with more or less success in laboratory scale (*133-143*). Negative electrodes using metal alloy reactions to store energy such as Si, Sb or Sn have excellent theoretical capacity but have problems such as large volume change, short cycle life, low rate capability and aggregation of particles. It is reported that graphene composites partially solve these issues (*144-146*). For example, Chou *et al.* showed a graphene/Si composite with capacity up to 1168 mAh/g, whereas graphene shows less than 200 mAh/g and silicon nanoparticles showed 346 mAh/g, but the issue of short cycle life persisted (*146*).

1.2.3 Transition Metal Dichalcogenides

Transition metal dichalcogenides are a family of two dimensional materials that are composed of an MX_2 layer, with M a transition metal element (Mo, W, etc.) and X a chalcogen element (S, Se, etc.) (*147*). The most common members of this large family are MoS_2, WS_2, and SnS_2 as represented in Figure 17. Multilayered transition metal dichalcogenides are structurally similar to graphite. Like graphite, the layers of transition metal dichalcogenides are bound to each other by weak Van-der-Waals interactions that can be broken to obtain single sheets that have different physical and chemical properties. These materials have been considered for different applications, including energy storage (*148*).

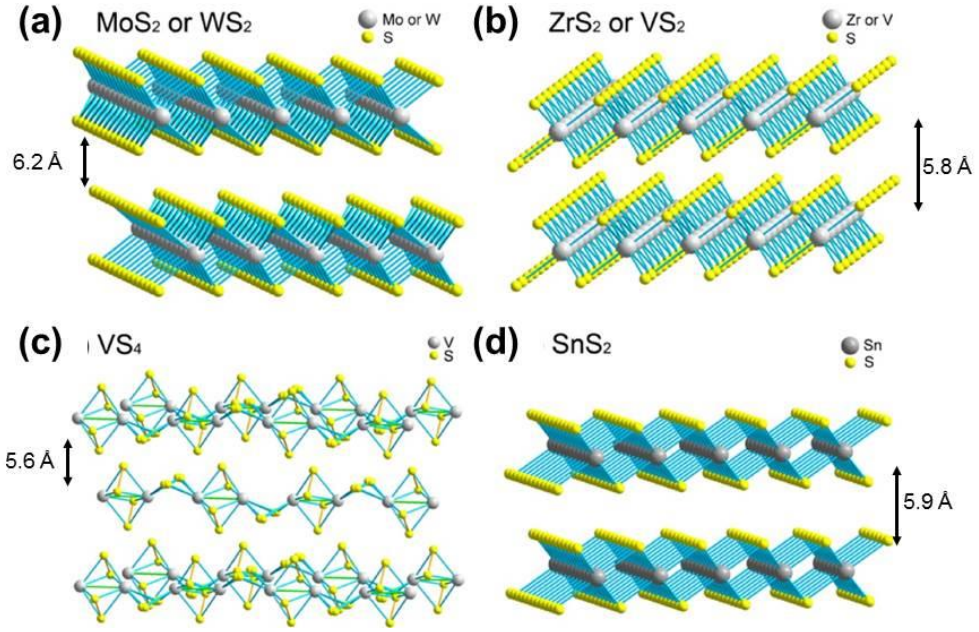

Figure 17: Structure of several typical layered transition metal sulfides: (a) MoS_2 or WS_2, (b) ZrS_2 or VS_2, (c) VS_4 and (d) SnS_2 (adapted from (*147*)).

1.2.3.1 Lithium-Ion Batteries

Among the transition metal dichalcogenide family, the layered transition metal sulfides have attracted attention as potential electrode for lithium-ion battery for different reasons. They store energy through complex mechanism such as conversion or alloying reactions. They have theoretical capacities higher than graphite (from 432 mAh/g for WS_2 to 1196 mAh/g for VS_4), show less volume change compared to silicon and metal oxides, and better rate capability and cycle life thanks to their layered structure.

The most investigated transition metal dichalcogenides for lithium-ion batteries are MoS_2 (*149, 150*) and Sn_2S (*147, 148, 151*). Many MoS_2 synthesis routes have been investigated but the capacity, up to 1183 mAh/g, have short cycle life. Moreover, the lithium storage mechanism in MoS_2 and several other metal sulfides is a 3 step process

which is not practical for commercial applications. Although the first cycle is irreversible, the interest in this system relies on the reversible lithiation/delithiation of sulfur. A systematic study by Kim and Goodenough demonstrated that the position of the potential plateau of this reaction increased with the heavier transition metal used (*152*).

1.2.3.2 Supercapacitors

Relatively few studies have focused on transition metal dichalcogenide for supercapacitor applications. Feng *et al*. investigated two dimensional VS_2 nanosheets for an in-plane supercapacitor (*153*). They succeeded in synthesizing VS_2 thin films with a high specific surface area and high conductivity. They fabricated the in-plane supercapacitors by a mechanical shaping process and a solid electrolyte (BMIMBF4-PVA gel) was used. Capacitance was measured from galvanostatic charge-discharge measurments and volumetric capacitance values up to 317 F/cm^3 were obtained with good cyclability. However, the cyclic voltammogram shown in Figure 18 was very resistive and far from the rectangular shape expected for supercapacitors.

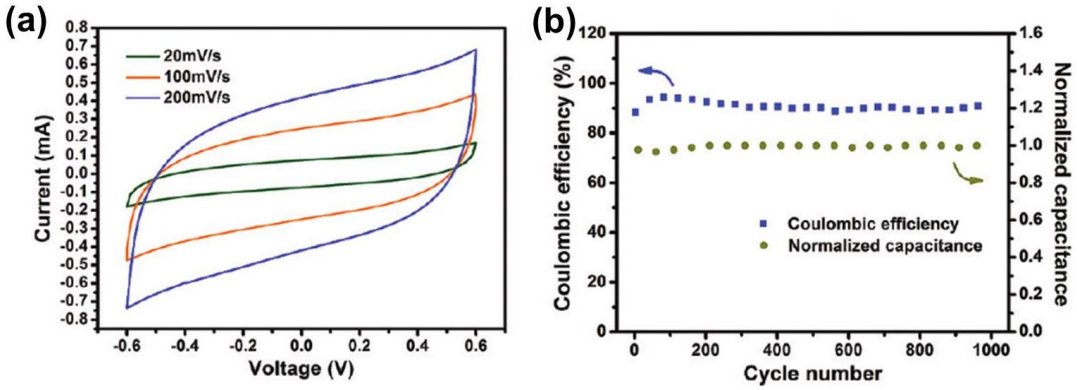

Figure 18: Performances of the in-plan supercapacitor based on VS_2; cyclic voltammetry (a) and cycle life (b) (adapted from (*153*)).

TiS_2 was proposed to have a pseudocapacitive behavior by Conway (*80*). Recently, Muller *et al*. investigated the electrochemical performance of TiS_2 as an electrode for Li-ion capacitors (*154*). The authors observed and analyzed the storage mechanism, separating the capacitive and pseudocapacitive behavior. Figure 19 shows the electrochemical performance. Impressive capacitances up to 540 F/g at 4C and 320 F/g at 120C were obtained but a potential drop occured between 3V and 2,5V, reducing the real voltage window.

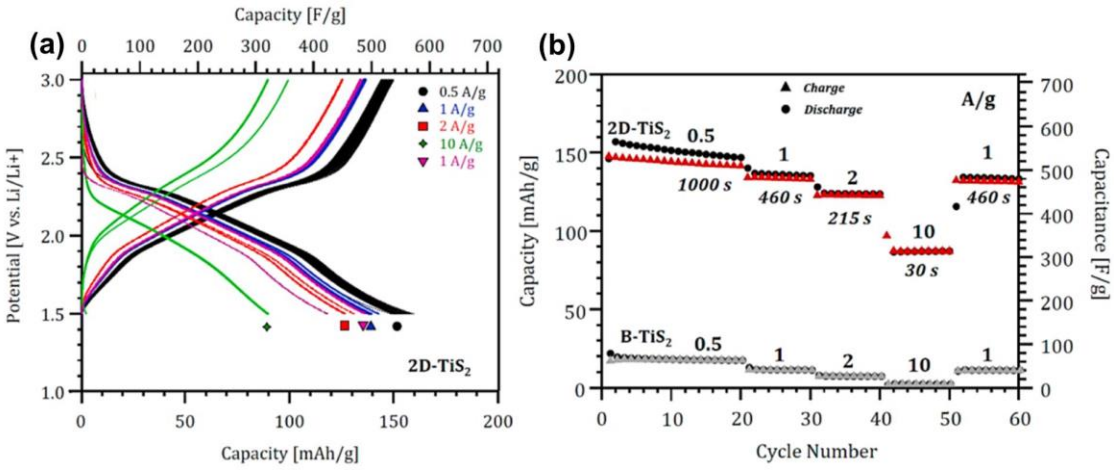

Figure 19: Charge−discharge curves (a) and rate capability (b) of TiS_2 (adapted from (*154*)).

1.3 New Two Dimensional Materials: MXenes

A new family of 2D materials has been discovered in 2011 by Y. Gogotsi and M. Barsoum groups at Drexel University; a whole family of exfoliated materials derived from MAX phases and called MXene (*8, 155*). These materials have a layered structure composed of more than one element. Ti_3C_2, Ti_2C, Ta_4C_3 and TiNbC were the first

compounds synthesized (*156*). The main interest in MXenes for energy storage applications is that these materials contain a carbide core that guarantees good conductivity and tunable transition metal oxides at the surface that can undergo redox reaction. Its potential for lithium-ion battery and lithium-ion capacitor applications has been previously demonstrated by M. Naguib *et al.* (*9*), and J. Come, *et al.* (*157*).

1.3.1 MAX Phases

MAX phases are a class of layered ternary carbides or nitrides composed of an early transition metal element M, an A-group element A and carbon or nitrogen, represented by X. Figure 20 shows a classification of the MAX phases on the periodic table (*158*).

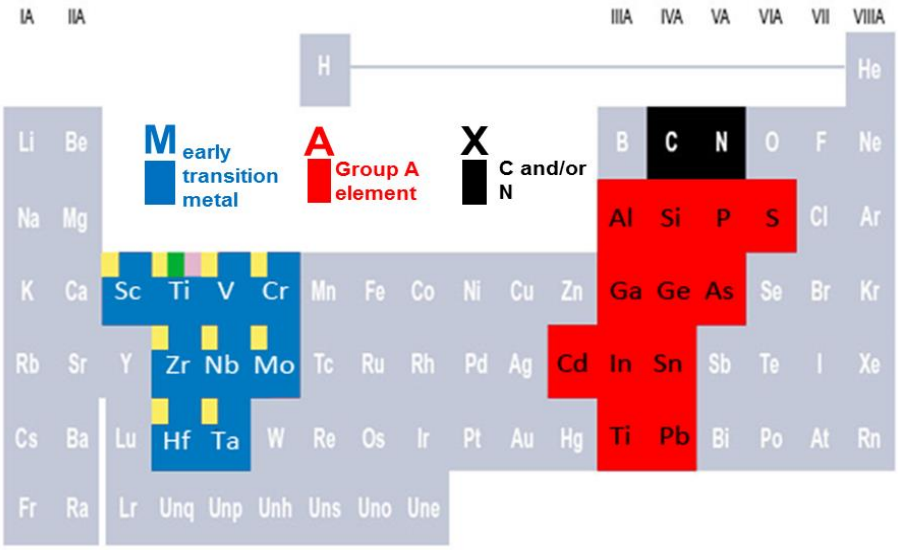

Figure 20: Distribution of M, A and X elements in the periodic table (adapted from (*158*)).

These phases are layered hexagonal (space group D^4_{6h}–$P6_3/mmc$) with two formula units per cell, as represented in Figure 21. They are organized in a $M_{n+1}AX_n$ chemistry, where n is 1, 2, or 3. There are commonly called by their respective chemistry, for example Ti_3AlC_2 belongs to the 312 group.

Regardless of the chemistry, a MAX phase structure can be described as close-packed layers of M layers which are interleaved with A layers in the center of a trigonal prism and where X atoms occupy the octahedral sites in M_6X. The main difference between the three structures shown in Figure 21 is the number of M-layers separating the A-layers; in 211 there are two, in 312 three and in 413 four.

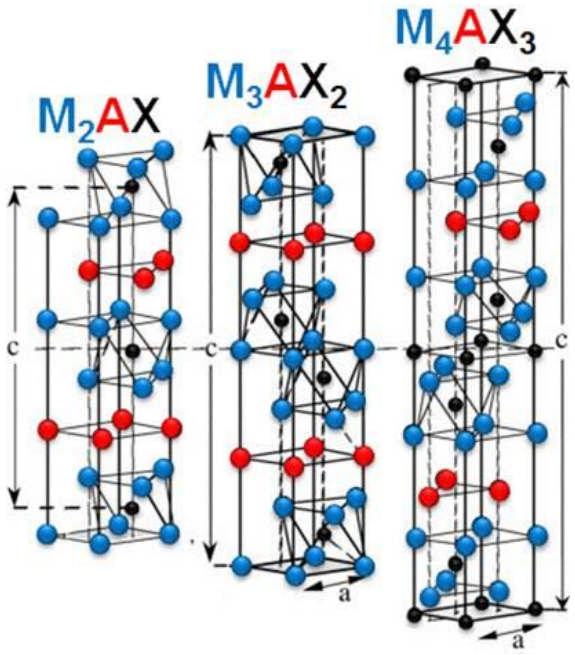

Figure 21: Crystalline structures of MAX phases M_2AX, M_3AX_2 and M_4AX_3 (adapted from (*158*)).

MAX phases are highly damage tolerant, resistant to chemical attack, thermal shock resistant, and machinable. In other terms, they have some properties found in metals and some found in ceramics. Anomalously, they are soft for transition metal carbides and nitrides (*158*).

The Vickers hardness values are between 2-8 GPa, which is high for transition metals. In some MAX phases it has been shown that they exhibit plastic-brittle transitions at temperature above 1000°C, while retaining decent mechanical properties. At elevated temperature, these phases decompose incongruently into MX-based compounds and A-rich liquids in an inert atmosphere whereas they are oxidized in air. Some display formation of protective oxide layer, and therefore have excellent oxidation resistance (*158*).

1.3.2 Synthesis of MXenes

A family of MAX phase derived compounds has been discovered: MXenes. More precisely it comprises exfoliated layers of MAX phases where the A layer has been removed. Developed in 2011, the first synthesis route consisted of a wet HF treatment of the MAX phases previously described. Figure 22 shows a schematic representation of the MXene synthesis. The reactions occurring were the following:

$$M_{n+1}AX_n + 3HF \rightarrow M_{n+1}X_n + \frac{3}{2}H_2 + AF_3 \quad (12)$$

$$M_{n+1}X_n + H_2O \rightarrow M_{n+1}X_n(OH)_2 + H_2 \quad (13)$$

$$M_{n+1}X_n + 2HF \rightarrow M_{n+1}X_nF_2 + H_2 \quad (14)$$

After etching, the MXene surface was not M-terminated but covered with oxygen-containing groups and fluorine. Considering that there are more than 60 MAX phases

known, with different properties, the MXene family is already believed to be as diverse and complex as its precursor. Previous studies already showed the successful synthesis of several member of this family: Ti_3C_2, Ta_4C_3, TiNbC, and $(V_{0.5}Cr_{0.5})_3C$ (*156*). Figure 23 shows scanning electron microscopy images of MAX phases and exfoliated MXenes. Electrical conductivities of cold pressed MXene disks were found to be comparable to multilayer graphene. The specific surface area was found to be about 20 m^2/g.

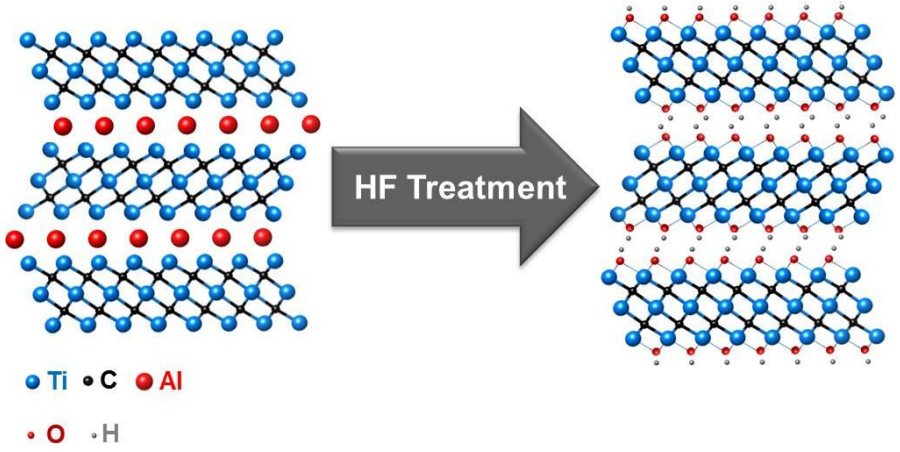

Figure 22: Schematic synthesis of MXenes from MAX phases (adapted from (*8*)).

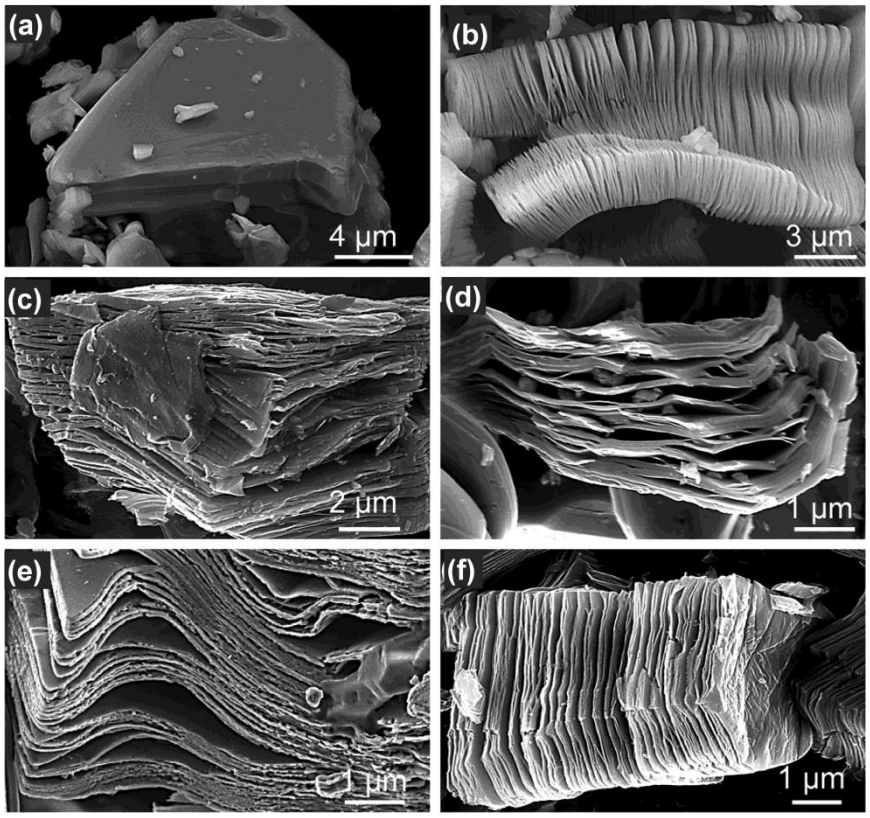

Figure 23: Secondary electron micrographs for (a) Ti_3AlC_2 particles before treatment. Particles after HF treatment of (b) Ti_3AlC_2, (c) Ti_2C, (d) Ta_4AlC_3, (e) TiNbAlC and (f) Ti_3AlCN (adapted from (*156*)).

1.3.3 Delamination

Intercalation and delamination of two-dimensional solids is a requisite step in many cases for exploiting the enhanced properties of two-dimensional materials. In 2012, Olha *et al*. demonstrated that MXenes could be intercalated by urea, hydrazine and N,N-dimethylformamide (DMF) (*159*). The increase of the c-lattice parameter of surface functionalized Ti_3C_2 was observed by X-ray diffraction (from 1.95 to 2.548 to 2.68 nm). Figure 24.a shows a schematic representation of intercalated MXene. When dimethyl sulphoxide (DMSO) was intercalated into Ti_3C_2, followed by sonication in water, the

Ti_3C_2 was delaminated (d-$Ti_3C_2T_x$) forming a stable colloidal solution (Figure 24.b) that was in turn filtered to produce single sheet MXene (Figure 24.c).

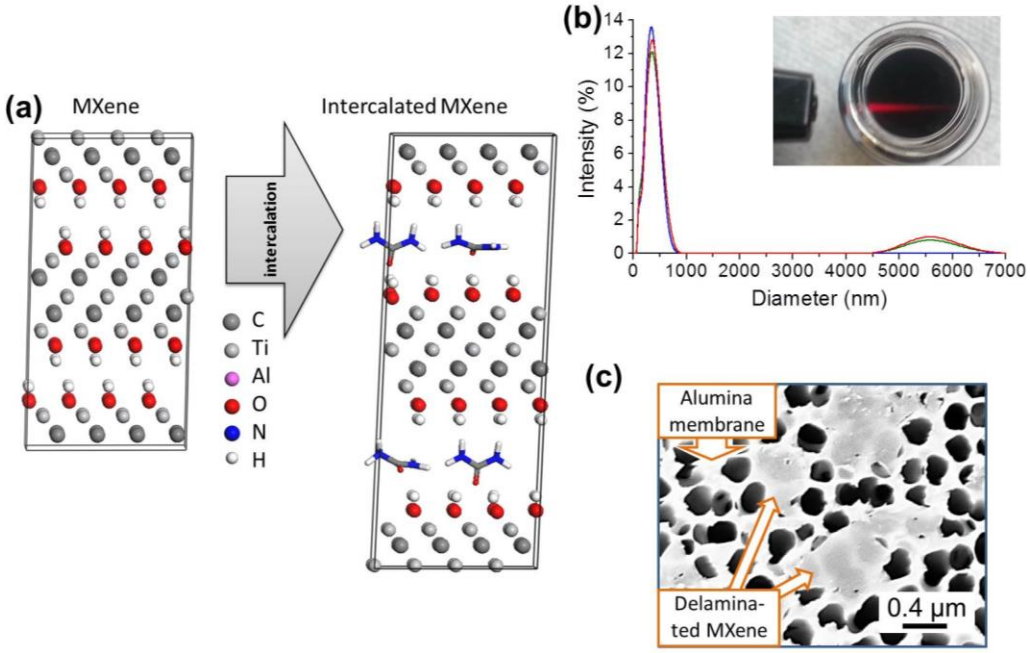

Figure 24: Schematic of the intercalation mechanism (a). Particle size distribution in aqueous colloidal solution; inset shows Tyndall scattering effect in solution (b). Scanning electron microscope image of d-Ti_3C_2 single flake on alumina membrane (c) (adapted from (*159*)).

1.3.4 Applications

Ti_2C was the first member of the family to be analyzed for lithium-ion battery application. The reason is that Ti_2AlC is one of the most common and cheapest MAX phases. Powders with particles smaller than 45 µm (− 325 mesh) are commercially available. It is also an excellent electronic conductor and its associated MXene is the lightest (*156*).

Figure 25.a shows the cyclic voltammogram of the Ti_2C electrode. A broad irreversible peak was observed around 0.6 V, during the first lithiation (*9*). It was attributed to the formation of a solid electrolyte interphase and to an irreversible reaction with the electrode material. Authors assigned these peaks with TiO_2 and lithiated titania. Thanks to the similarities, the following redox reaction was proposed:

$$Ti_2CO_x + yLi^+ + ye^- \leftrightarrow Li_yTi_2CO_x \quad (15)$$

It was suggested by the authors that because the electrode was dried at 200°C prior to assembling the coin cell, all absorbed water and OH species were removed. Figure 25.b show capacity values *vs.* cycle number. A stable capacity of 225 mAh/g at a C/25 rate was reported, corresponding to about one Li^+ per Ti_2C formula unit. A promising reversible cycling capacity of 80 mAh g^{-1} at 3C rate and 70 mAh g^{-1} after 200 cycles at a 10C rate were reported.

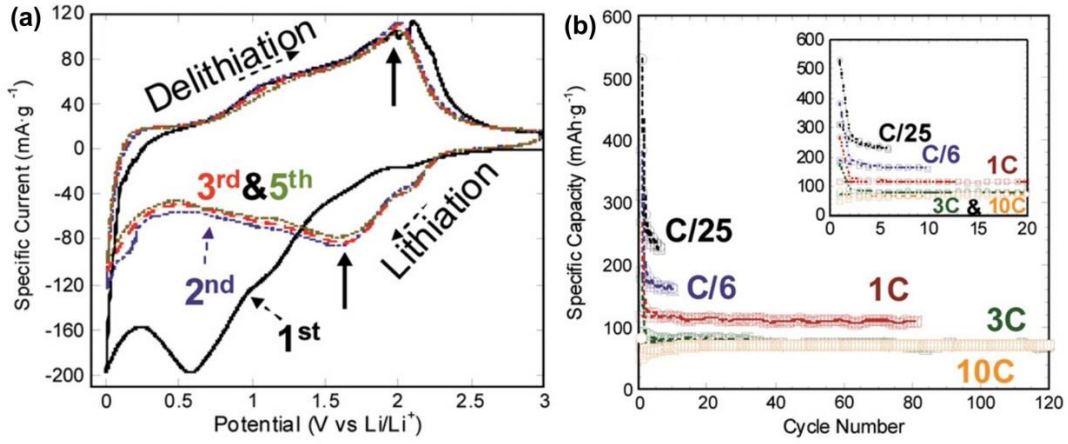

Figure 25: Cyclic voltammetry at a constant scan rate of 0.2 mV/s. (a) and capacities vs cycle number at different scan rates (b) (adapted from (*9*)).

Moreover, Ti_2C was investigated as a negative electrode material in non-aqueous asymmetric cell in lithium-ion capacitors (*157*). The authors investigated the lithiation/delithiation mechanism. Figure 26.a shows *in-situ* X-ray diffraction measurement. A shift was observed, consistent with the lithium insertion process. Figure 26.b shows charge and discharge specific capacity at 10C rate. The capacity decreased from 70 mAh/g to 60 mAh/g after 1,000 cycles.

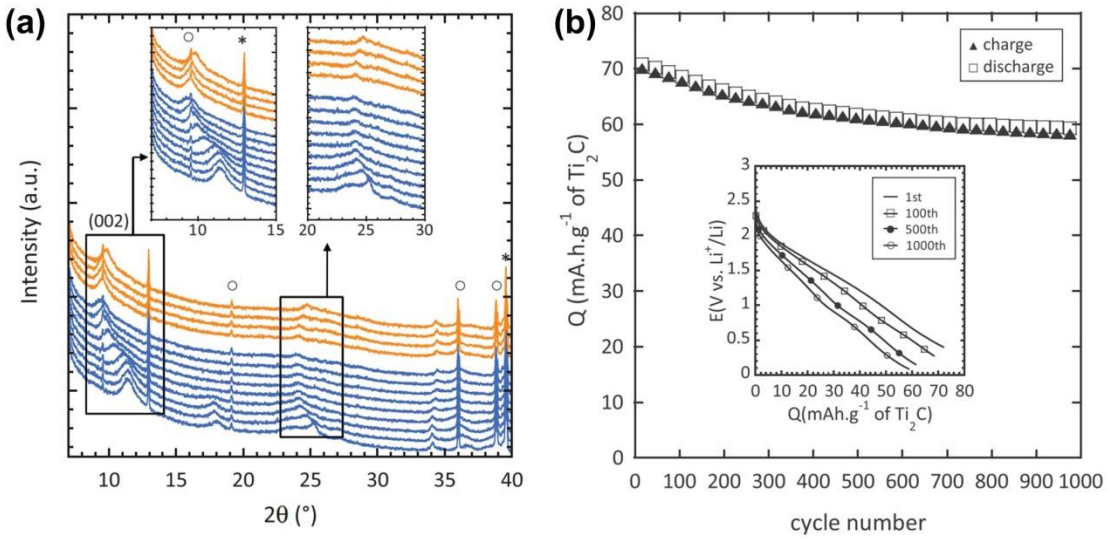

Figure 26: *In-situ* X-ray diffraction patterns during charge and discharge of Ti_2C (a). Charge and discharge specific capacities vs. cycle number of a Ti_2C/activated carbon asymmetric cell at 10C rate. Inset: corresponding curves at different cycles (b) (adapted from (*157*)).

The delamination process of Ti_3C_2 recently discovered was used to assemble a binder-free MXene 'paper' (inset Figure. 27.a) by filtering the aforementioned colloidal solution through a membrane. The breakthrough in terms of lithium-ion battery applications was the Li-ion uptake on d-Ti_3C_2 free-standing paper. As shown in Fig. I.30.A the capacity of

d-Ti_3C_2 was a factor of 4 higher than that of the as-synthesized Ti_3C_2. The paper showed a capacity of 410 mAh/g at a 1C cycling rate and 110 mAh/g at 36C. As shown in Fig I.32.B, the 410 mAh/g represented three Li^+ ions per $Ti_3C_2(OH)_2$. The capacity obtained at 1C rate was higher than the maximum theoretical capacity of Ti_3C_2 MXene predicted (320 mAh/g (*160*)). The results at 1C rate were better than graphite and MXene exhibited excellent rate capability promising for high power applications. Nevertheless no plateau was observed during cycling, thus limiting the interest for this material as a lithium-ion battery electrode. The good rate capability obtained was not the objective of this preliminary work, but it raised the interest in these materials toward high power applications. It is essential to further study this large family of materials to improve its power densities.

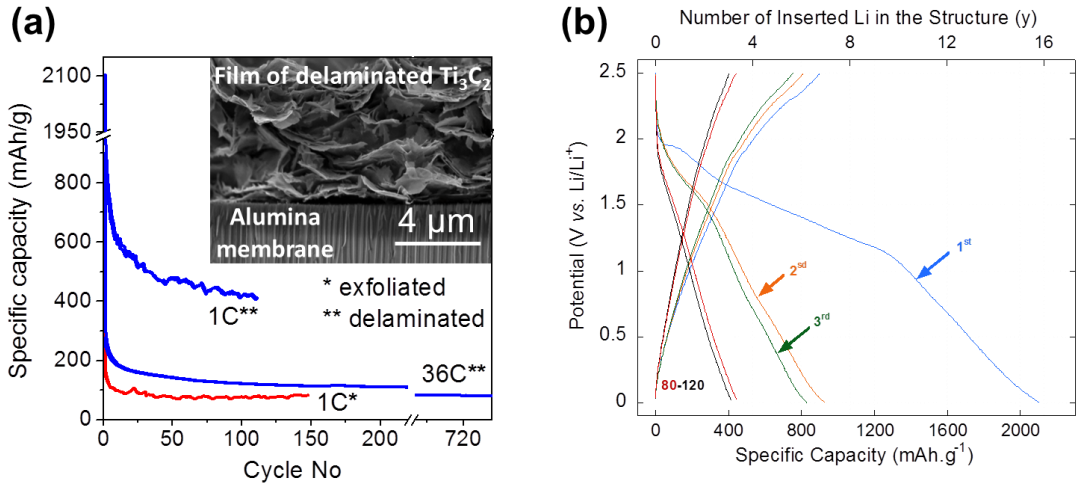

Figure 27: Comparison of the performance of exfoliated and delaminated Ti_3C_2 as an anode material in Li-ion batteries. Inset shows scanning electron microscope image of an additive-free film of delaminated f-Ti_3C_2 filtered through the membrane. (a) The galvanostatic charge/discharge curves at a 1C rate. The "y" value shown on top x-axis was calculated assuming a MXene chemistry of $Ti_3C_2(OH)_2$ (b) (adapted from (*159*)).

1.4 Objectives

This PhD thesis started just after the demonstration by O. Mashtalir *et al*. (*159*) of the intercalation of large organic molecules into MXenes, the elaboration of delamination procedure and the electrochemical testing of the delaminated paper as electrode materials for lithium-ion batteries, which demonstrated the impressive rate capability.

Herein, the primary objective of this PhD thesis was to investigate MXene performance for high power applications. The challenges were to select the right MXene for each application, to optimize the selected MXene by preparing composites or by chemically modifying its surface and to investigate the energy storage mechanism. Energy storage applications and two-dimensional materials are among the hottest research topics. Since the initial discovery of MXenes in 2011, scientific activities on this topic started worldwide.

The high rate performance demonstrated in lithium-ion batteries led to the investigation of the electrochemical performance of MXene for supercapacitors. Chapter 3 is focused on multilayered MXene and delaminated MXene electrodes tested in various aqueous electrolytes. The effect of the surface chemistry is extensively discussed. The results demonstrated the intercalation of large cations into Ti_3C_2, including Na^+. This encouraged the exploration of MXene for beyond-lithium-ion batteries.

Chapter 4 is focused on the systematic investigation of all synthesized MXenes for negative and positive electrodes for either sodium-ion batteries or sodium-ion capacitors. The behavior during charge-discharge cycling lacked a potential plateau, which is extremely important for practical battery type electrodes. Therefore the research shifted toward Na-ion capacitors. However around the same time, Wang *et al*. released an article

about Ti_2C as a negative electrode for Na-ion capacitors. In order to propose innovative research, V_2C has been proposed as a positive electrode and a full cell with hard carbon was assembled.

The results obtained in 2014 by Ghidui *et al*. (*161*) concerning a new synthesis method and the results obtained by Zhao *et al*. (*162*) concerning CNT/MXene composites modified the direction of the end of the thesis. From the study of HF synthesized MXene, the study changed toward CNT/'clay'MXene electrodes. Chapter 5 investigates the electrochemical behavior as supercapacitor electrodes in organic electrolyte in order to increase the potential window and increase the power density.

CHAPTER 2: Materials and Methods

2.1 MXene Synthesis

Two-dimensional transition metal carbides and nitrides, called MXenes, studied in this thesis were prepared in collaboration with Professor M. Barsoum's group at Drexel University.

2.1.1 MAX Phases

MXenes are derived from MAX phases that are a class of layered ternary carbides and/or nitrides that were introduced in the previous chapter (Figure 20 and 21). The MAX phases used were either commercial or were prepared at Drexel University by ball milling raw precursors in a specific ratio then heating in a tube furnace under argon. The following seven different MAX phases were prepared for the study; Ti_3AlC_2, Ti_2AlC, Nb_2AlC, V_2AlC, TiVAlC, $Ti_{1.5}V_{1.5}AlC_2$ and Ti_3AlCN.

The Ti_3AlC_2 MAX phase was synthesized by mixing commercial Ti_2AlC powders (> 92 wt. %, 3-ONE-2, Voorhees, NJ) with TiC (99%, Johnson Matthey Electronics, NY) in a 1:1 molar ratio, followed by ball milling for 24 h using zirconia balls. The mixture was then heated at 5 °C/min, under flowing argon in a tube furnace for 2 h at 1,350 °C. The resulting lightly sintered brick was ground using a TiN-coated milling bit and sieved through a 400 mesh sieve producing powder with particle size less than 38 μm (*8*).

2.1.2 Etching

Wet hydrofluoric acid (HF) treatment of MAX phases was the first efficient method to synthetize MXenes discovered. It allowed selective extraction of the aluminum layers from the MAX phases.

To synthetize a given MXene, 10 g of the corresponding MAX phase was immersed in 100 mL of HF solution (Fisher Scientific, Fair Lawn, NJ) at room temperature. The reactions between HF and the MAX phase were previously discussed in Chapter 1. The resulting suspension was then rinsed several times using deionized water and centrifuged (at 1400 rpm) to separate the powders. The resulting layers were terminated with mostly oxygenated and fluorinated groups, which were weakly bonded together. In regards to the functional groups, T_x were added to the MXene formula, where "T_x" stand for terminated-surface groups such as in $Ti_3C_2T_x$. Table 4 gives the detailed synthesis conditions for each MXene.

Table 4: Synthesis condition of MXenes.

MAX Phase	HF concentration	Time (hour)	MXene
Ti_3AlC_2	50%	18	$Ti_3C_2T_x$
Ti_2AlC	10%	10	Ti_2CT_x
Nb_2AlC	50%	90	Nb_2CT_x
V_2AlC	50%	8	V_2CT_x
TiVAlC	50%	1	$TiVCT_x$
$Ti_{1.5}V_{1.5}AlC_2$	50%	18	$Ti_{1.5}V_{1.5}C_2T_x$
Ti_3AlCN	30%	18	Ti_3CNT_x

2.1.3 Delamination

The delamination process, described in Chapter 1 and illustrated in Figure 28, consisted of intercalating a large organic molecule to weaken the Van-der-Waals force between layers and using ultra-sound to completely separate the layers (*163*). After mixing the $Ti_3C_2T_x$ with dimethyl sulfoxide (DMSO) for 18 h at room temperature, the colloidal MXene suspension was centrifuged (1400 rpm) to separate the intercalated powder from the liquid DMSO. After decantation of the supernatant, deionized water was added to the residue in a weight ratio of MXene to water of 1:500. After bath sonication of the suspension for 6 h, centrifuging was carried out and the supernatant was filtered using a porous anodic aluminium oxide membrane filter (47 mm diameter, 0.2 mm pore size, Whatman Anodisc, Maidstone, UK) and dried in an oven at 70°C overnight, resulting in d-MXene ‘paper’ that detached easily from the membrane (*159*).

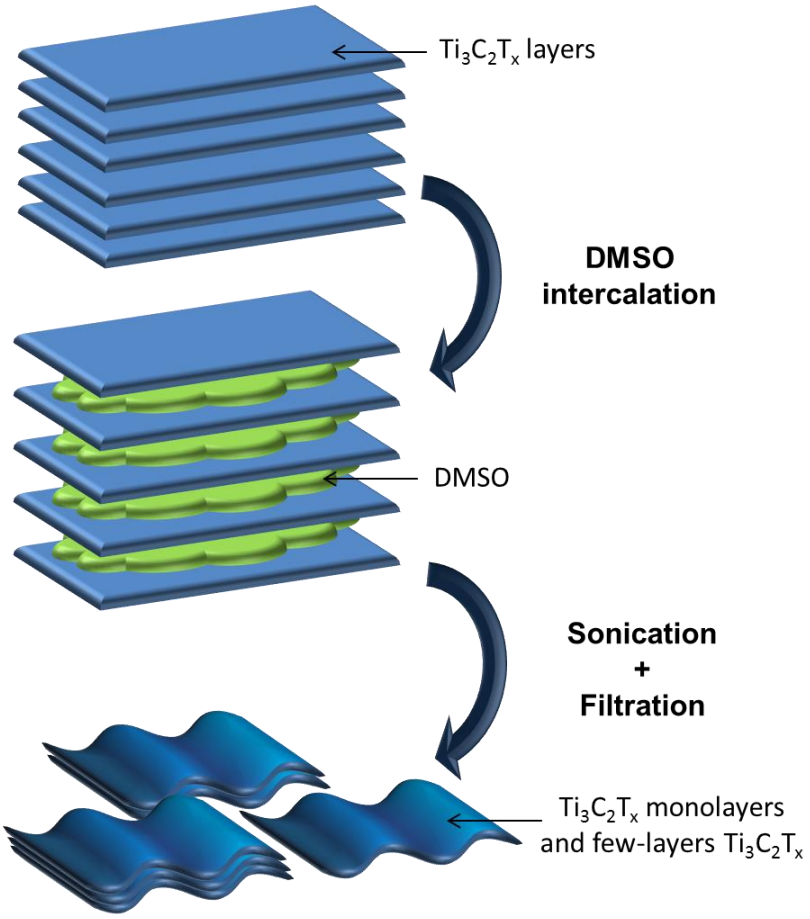

Figure 28: Schematic of the delamination process.

2.2 Electrochemical Characterization

Electrochemical characterization of the materials were done using two types of Swagelok® cells (2- and 3-electrode). Three main electrochemical techniques were used, cyclic voltammetry, galvanostatic charge-discharge and electrochemical impedance spectroscopy, at room temperature using a VMP3 potentiostat (Bio-Logic S.A, France).

2.2.1 Electrochemical Cells

2.2.1.1 Two-Electrode Setup

Figure 29 shows the two electrode Swagelok® cell used for assessing the electrochemical performances of the different MXenes synthesized.

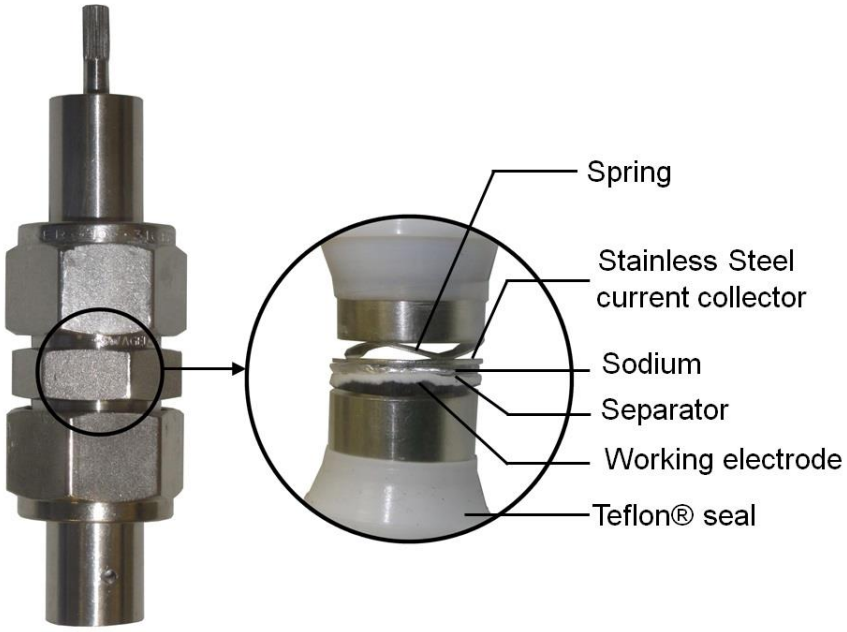

Figure 29: Picture of a 2-electrode Swagelok® cell.

This configuration was mainly used for cyclic voltammetry tests in a half-cell sodium-ion battery configuration. In this case, the working electrode was set as the positive electrode and metallic sodium is the negative electrode. The cell was assembled in an argon-filled glovebox because both the electrolyte and metallic sodium are oxygen and water sensitive.

2.2.1.2 Three-Electrode setup

In a three electrode configuration, a reference electrode was added and placed near the two others. Therefore, it was possible to control the potential of the working (positive) electrode while simultaneously measuring the potential of the negative electrode vs. the reference. Silver wire was selected to be the quasi-reference electrode thanks to its electrochemical stability in all the electrolytes studied. Figure 30 shows the three-electrode Swagelok® cell used.

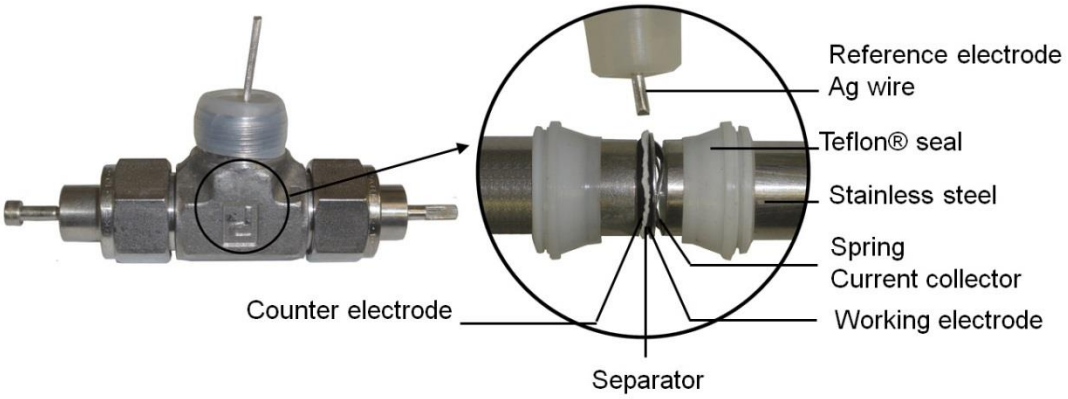

Figure 30: Picture of a 3-electrode Swagelok® cell.

With this cell, two types of setup were possible. In the first case, the potential was controlled and/or measured between the working electrode and the reference electrode. This configuration was used in Chapters 3 and 5, where an overcapacitive activated carbon was used as a counter electrode. In the second case, the potential was controlled and/or measured between the working electrode and the counter electrode. This configuration was used in Chapter 4 for the full cell study using a hard carbon negative counter electrode and a positive V_2CT_x electrode.

2.2.2 Cyclic Voltammetry

Cyclic voltammetry measurement involve measuring the current response when imposing a potential change at a constant scan rate (v in V/s) between two set potentials according to the following equation:

$$E(t) = E_0 \pm vt \tag{16}$$

Where, E_0 is the initial potential (V), generally the open circuit potential, v is the scan rate (V/s), and t is time (s).

When the cell potential reaches a set potential, the linear potential sweep is reversed. During cycling, a current is generated due to the potential variation. Herein, the current is mainly driven by various electrochemical phenomena occurring at the electrode/electrolyte interface. The two main phenomena are charge storage through redox reactions and double layer capacitance. Their corresponding I vs. E voltammograms are shown Figure 31.

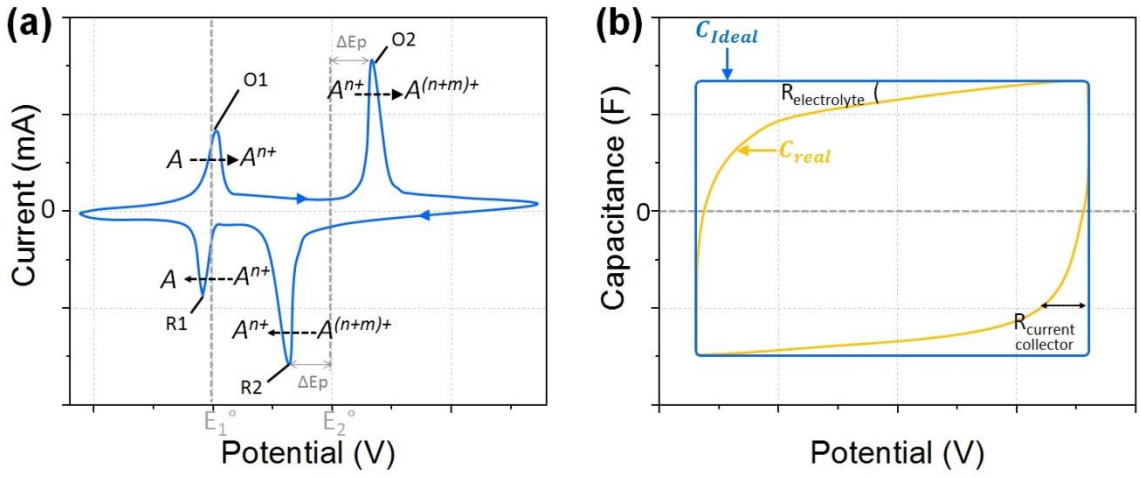

Figure 31: Typical cyclic voltammograms of redox (a) and double layer (b) materials.

In the first example (Figure 31.a) the presence of two set of peaks (O1;R1 and O2:R2) that was attributed to two redox reactions.

$$A^{n+} + ne^- \leftrightarrow A \quad (17)$$

$$A^{(n+m)+} + me^- \leftrightarrow A^{n+} \quad (18)$$

In this example, the oxidant of one reaction is the reductant of the other. The distance between the peaks, or ΔEp, of the second reaction was larger than the first, meaning that this reaction was more irreversible (or showed a larger potential polarization). ΔEp increases with the scan rate and diffusion limitation can be extrapolated. In reversible redox reactions, the areas of oxidation and reduction peaks are the same. In most battery-type electrode, the peak current intensity is proportional to the square root of the scan rate which means that the reactions are usually kinetically limited by mass transfer to the electrode.

In the second example, Figure 31.b, rectangular shaped voltammograms characteristic of capacitive behavior is observed. The differences between an ideal double layer capacitor and a more realistic supercapacitor have many origins. An ideal double layer capacitance is constant at all scan rates and is determined from the equation 19:

$$C_{dl} = \frac{I}{v} \quad (19)$$

Where, C_{dl} is the double layer capacitance of an electrode (F), v the scan rate (V/s) and I the current (A).

Several phenomena can cause deviations from ideal rectangular voltammograms. The most common are the series resistance (mainly coming from the electrolyte resistance), electrolyte decomposition, gas evolution, irreversible surface reactions and the carbon

pore size distribution that may create mass transfer limitation in smaller pores at high potential scan rates.

2.2.3 Galvanostatic Charge-Discharge Measurements

The galvanostatic charge-discharge measurements consisted of passing a constant current to the cell and recording the potential evolution with time. A potential window is selected and when a potential limit is reached the current is reversed. The charge/discharge curves are usually plotted as potential vs. time or potential vs. capacity. This technique is also used to estimate the cycle life of the cell, by repeating the charge/discharge a high number of times and trace the capacity or capacitance vs. the cycle number. The cycling rate is generally noted as C/n rate where n is the time in hours for a complete charge or discharge at the corresponding current density and C the capacity (Ah). Usually the rate is lower for batteries (tens of minutes to hours) than for supercapacitors (tens of seconds to minutes).

As shown in Chapter 1, batteries and supercapacitors have different behaviors during galvanostatic cycling. Figure 32 summarize the main characteristic observable on charge-discharge curves.

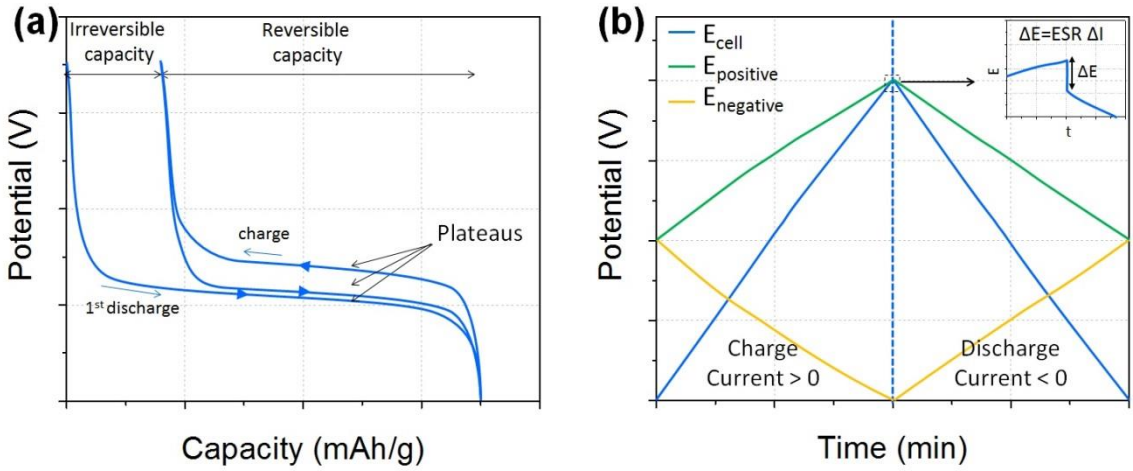

Figure 32: Typical galvanostatic charge-discharge curves of lithium-ion intercalation (a) and double layer (b) materials.

In both cases, the specific capacity is calculated from equation 11. Volumetric and areal capacities are also often calculated.

$$Q = \frac{I \times t}{m} \tag{11}$$

Where Q is the specific capacity (mAh/g), I the current applied (A), t the time (h) and m the mass (g).

In the example of redox reaction Figure 32.a, the plateau regions are characteristic of a two-phase mechanism corresponding to the insertion of cations into the host material. These redox reactions occur at a fixed potential. The differences of plateau potential during charging and discharging can originate from thermodynamic limitations, charge transfer kinetics limitations, ion diffusion, and electrical resistance (*164*). In most cases for batteries, irreversibility is observed during the first cycle. For lithium-ion batteries irreversible reactions occur, such as the formation of a solid electrolyte interphase at the

anode during charging, which is responsible for the irreversibility seen in the first cycle (*165*).

In the case of capacitive-type electrodes, Figure 32.b, the potential follows a quasi-straight line during galvanostatic charge-discharge measurements that correspond to the following equation:

$$\Delta E = I \times (ESR + \frac{t}{C}) \quad (20)$$

Where ΔE is the potential evolution (V), I the current applied (A), ESR the equivalent series resistance (Ω), C the double layer capacitance (F) and t the time (s).

The coulombic efficiency is a factor that brings out information regarding the cycle life of a cell. It is calculated as follow:

$$\eta\ (\%) = \frac{Q_{discharge}}{Q_{charge}} \quad (21)$$

Double layer capacitive materials have excellent coulombic efficiency (>99%) which allow supercapacitors to reach 100,000 cycles. In contrast, electrode materials that store charge through redox reactions usually have lower coulombic efficiency. The cycle life of lithium-ion batteries is approximately hundreds of cycles.

2.2.4 Electrochemical Impedance Spectroscopy

This technique consists in imposing a sinusoidal potential of small amplitude (few mV) over a wide range of frequency f (from hundreds of kHz down to few mHz) according to equation 14 to a steady state. Equation 22 describes the current response to the applied potential. It is a sinusoidal current which presents a shifted angle of phase φ.

$$E = E_0 + \Delta E sin(\omega t) \quad (22)$$

$$I = I_0 + \Delta I sin(\omega t + \varphi) \quad (23)$$

Where E is the potential (V), E_0 the initial steady state potential (V), ΔE the amplitude of the signal (V), ω the pulsation (rad.s^{-1}), t the time (s), I the current (A), I_0 the initial steady state current (in this thesis I_0 = 0 A), ΔI the amplitude of the current response (A) and φ the phase shift.

In order to facilitate mathematical treatment, the potential and current during electrochemical impedance spectroscopy are usually written with complex numbers as follow:

$$\Delta E = \Delta E_{max} e^{j(\omega t)} \tag{24}$$

$$\Delta I = \Delta I_{max} e^{j(\omega t + \varphi)} \tag{25}$$

The complex impedance is defined by the ratio between the complex potential and complex current:

$$Z = \frac{\Delta \mathrm{E}}{\Delta \mathrm{I}} = \frac{\Delta E_{max}}{\Delta I_{max}} e^{-j\varphi} \tag{26}$$

And using Euler's formula:

$$Z == \frac{\Delta E_{max}}{\Delta I_{max}} \cdot [\cos(\varphi) - j sin(\varphi)] = Re(Z) - j \times Im(Z) \tag{27}$$

Where Re(Z) and Im(Z) are the real and imaginary parts of the impedance.

The most common data representation method is to plot –Im(Z) versus Re(Z), which is called a Nyquist plot. Figure 33 represents the Nyquist plot of the electrochemical impedance for two different electrochemical systems.

The equivalent circuit of a lithium-ion electrode is presented Figure 33.a, accompanied with a typical impedance of an intercalation material $Li_xMn_2O_4$ (*166-168*). When the frequency tends to ∞, the impedance depends on the electrolyte resistance. When the frequency decreases, the first semi-circle observed corresponds to the solid

electrolyte interphase and the second semi-circle describes non-ideal double layer behavior. At lower frequencies, an element called Warburg impedance is present, related to diffusion limitations, then the curve tends towards a vertical line associated with intercalation capacitance (*167*).

The Nyquist impedance and equivalent circuit of a porous electrode in electrochemical double layer capacitors are represented in Figure 33.b. This model, called the Transmission Line Model, was proposed by De Levie in 1963 and consists of a succession of series/parallel RC components that account for the porosity of the carbon (*169, 170*). At high frequencies the ions can only reach the outer surface of the electrode, thus the impedance depends on the electrolyte resistance, the current collector resistance and electronic resistance of the electrodes. When the frequency decreases, schematically, ions can access deeper into the pores, thus the resistance increases due to the diffusion of ions into the pores. As the frequency decreases, it reaches the knee frequency which corresponds to the frequency where the resistance reaches a maximum. At lower frequencies, a vertical straight line is observed, corresponding to a capacitive behavior (*171*).

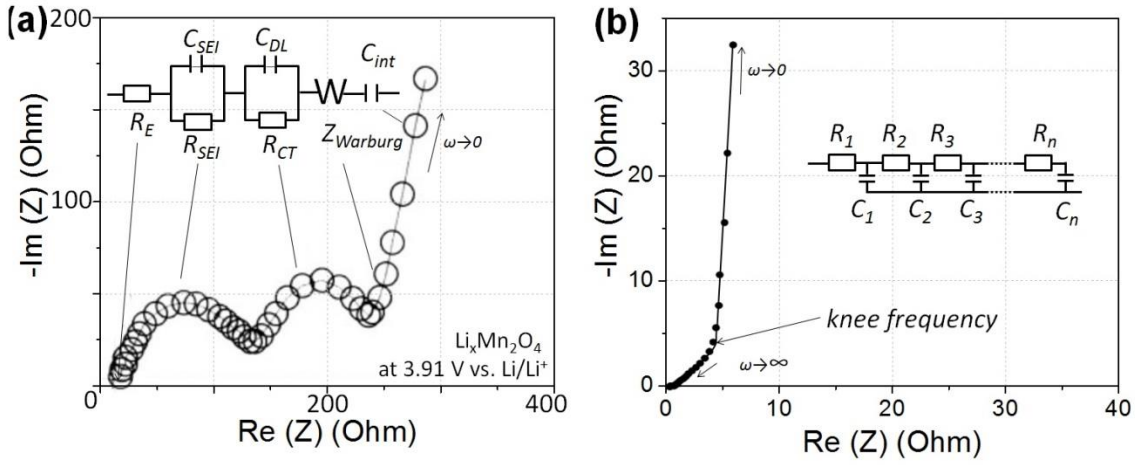

Figure 33: Typical Nyquist plots of battery-type materials ($Li_xMn_2O_4$) (a) and carbon double layer materials (b). Inset: equivalent circuit. (adapted from (*167*) (*171*))

2.3 Materials Characterization Techniques

2.3.1 X-Ray Diffraction

2.3.1.1 Principle

X-ray diffraction is an analytical technique used to characterize the atomic structure of materials. A solid is defined as crystal when it is composed of a regular arrangement of atoms as represented in Figure 34. The crystal is defined by a three dimensional lattice and the interplane atomic spacing is noted d_{hkl} where h, k and l, called Miller indices, are the reciprocal of the lattice vectors.

The X-rays generated from copper excitation irradiate the solid, and are scattered by its electrons. The wavelength of copper Kα radiation is similar in size to d_{hkl} (few Å). As a consequence, diffraction patterns can be observed due to constructive and destructive interference between X-rays and atoms. The condition for constructive interference is given by Bragg's Law:

$$n\lambda = 2d_{hkl}sin\theta \quad (28)$$

Where n is an integer corresponding to the order of the reflection, λ the wavelength of radiation used (m), d_{hkl} the interplane atomic spacing (m) and θ the scattering angle (rad).

In a θ-2θ configuration, θ corresponds to the angle between the hkl plane and the incident X-ray and the diffracted X-ray. The detector is placed at an angle of 2θ to the incident X-rays. The results are usually presented as the intensity vs. 2θ. From the position of intensity peak it is possible to calculate d_{hkl} according to Bragg's Law. In the specific case of MXenes the (002) plane, corresponding to h=0 k=0 and l=2, diffracts and is one of the most intense peaks observed. The 2θ position of this peak is therefore used to determine the c-lattice parameter.

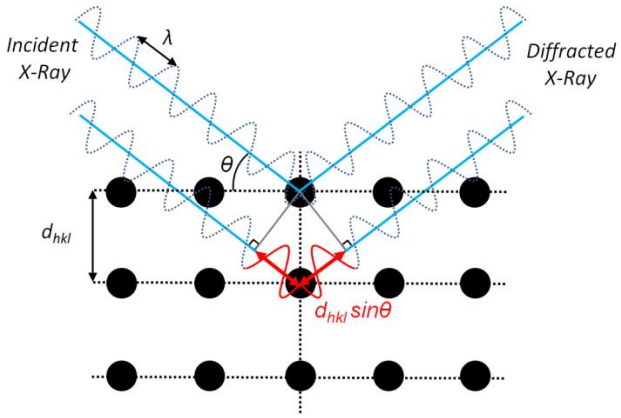

Figure 34: Schematic of Bragg diffraction.

2.3.1.2 Equipment

Ex-situ X-ray diffraction patterns of the electrodes were collected using a Bruker D4 diffractometer using Cu Kα radiation (λ = 1.5406 Å) over the range 2θ = 5−50° with a step size of 0.016°.

In-situ X-ray diffraction patterns of $Ti_3C_2T_x$ electrodes were collected on a Bruker D8 diffractometer using Cu Kα radiation (λ=1.5406 Å) with a step of 0.02°. Figure 35 shows the special 2-electrode Swagelok® type cell designed in LRCS (Amiens University), where the samples are placed and covered with materials that are transparent to X-ray to avoid electrolyte evaporation and allow *in-situ* X-ray diffraction. With aqueous electrolytes a Mylar® window was used whereas a beryllium window was used with organic electrolytes. The counter electrodes were either overcapacitive activated carbon or metallic sodium. In each chapter, the corresponding experimental details of the *in-situ* setup will be described.

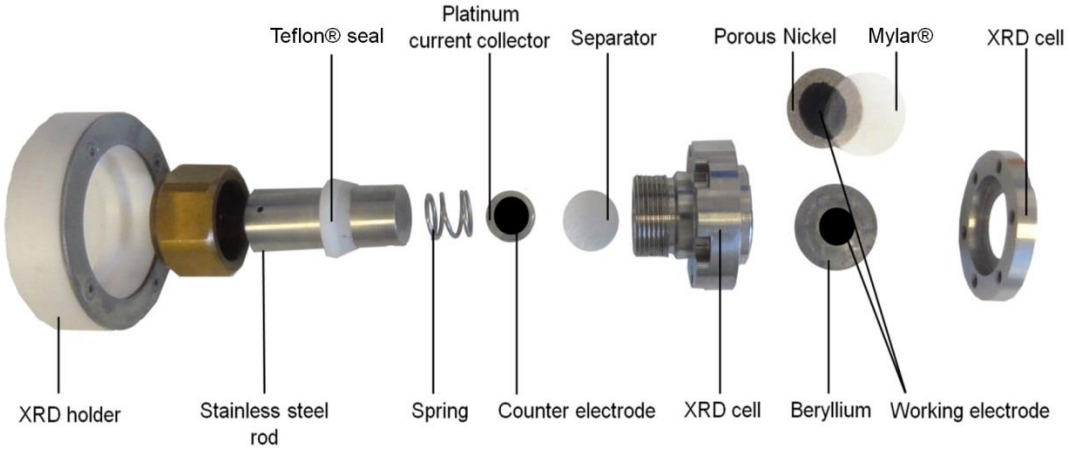

Figure 35: Photograph of the electrochemical *in-situ* X-ray diffraction cell.

2.3.2 Scanning Electron Microscopy

2.3.2.1 Principle

Scanning electron microscopy is a technique commonly used to observe the surface topography of materials at the microscopic scale based on the interaction of the material with a beam of electrons. The electron beam is produced thermionically by a tungsten filament cathode of an electron gun. The interaction between the material and the electron beam produce various types of radiation (electrons, X-rays and fluorescence). Specialized detectors collect the secondary electrons which are low-energy electrons (<50 eV) ejected from the k-shell of the atoms at the surface of the material. An image is created by scanning the material surface with the electron beam and recording the number of secondary electrons detected.

2.3.2.2 Equipment

Two scanning electron microscopes were used to investigate the electrode morphology, structure and thickness. A JSM-6700F (JEOL, Japan) was used by Barbara Daffos and a Zeiss Supra 50 VP (Carl Zeiss SMT AG, Oberkochen, Germany) was used by Maria R. Lukatskaya.

2.3.3 Energy Dispersive X-ray Spectroscopy

Energy dispersive X-ray spectroscopy is a technique used for elemental analysis and is often present in scanning electron microscopes, like in this case. A Zeiss Supra 50 VP (Carl Zeiss SMT AG, Oberkochen, Germany) was used. The principle is to use an X-ray detector to record the number and energy of X-rays produced from the sample studied

during irradiation by an electron beam. The energies of the X-rays emitted are converted to measure the elemental composition of the sample.

2.3.4 Gas Sorption Analysis

Gas sorption analysis consists of measuring the quantity of gas absorbed by the sample studied as a function of gas pressure at constant temperature. This data can be used to calculate the specific surface area using the Brunauer–Emmet–Teller (BET) equation. Nitrogen sorption analysis at 77 K using a Micromeritics ASAP 2020 apparatus was carried out after outgassing under vacuum at 300 °C for 12 h. The analysis was performed with the help of Barbara Daffos.

2.3.5 X-ray Photoelectron Spectroscopy

X-ray photoelectron spectroscopy is a technique commonly used to analyze the surface chemistry of a sample based on the interaction of the material with an X-ray beam that produces photo-emitted electrons. The number and kinetic energy of these electrons can be measured using a specialized detector under ultrahigh vacuum ($<10^{-7}$ Pa). An X-ray photoelectron spectrometer (VersaProbe 5000, Physical Electronics Inc., USA) using a 100 μm monochromatic Al Kα X-ray beam to irradiate the surface of the samples was used to obtain X-ray photoelectron spectra. Emitted photoelectrons were collected using a 180° hemispherical electron energy analyzer. Samples were analyzed at a 45° takeoff angle between the sample surface and the path to the analyzer. High-resolution spectra were taken at a pass energy of 23.50 eV and with a step size of 0.05 eV. The peak fitting was carried out using CasaXPS Version 2.3.16 RP 1.6. The experiment and analyses were performed by Kevin M. Cook at Drexel University.

CHAPTER 3: MXene as Supercapacitor Electrode in Aqueous Electrolytes

3.1 Introduction

The primary objective of this chapter was to investigate the electrochemical performance of MXene as an electrode material for supercapacitors for high power applications.

The strategy was to develop MXene electrodes for supercapacitors that could potentially store energy through surface redox reactions or intercalation of ions between layers. In this chapter, the study focuses exclusively on Ti_3C_2 which was selected because it has shown the best performances in lithium-ion batteries. The intercalation of ions between MXene layers has been previously observed. Come *et al*. demonstrated the intercalation of Li^+ into Ti_2C promoted electrochemically (*157*) and Mashtalir *et al*. showed the spontaneous intercalation of organic molecules (DMSO, hydrazine, urea) into Ti_3C_2 (*159*). The purpose of this work was to investigate the spontaneous intercalation of ions from several aqueous electrolytes in between the 2D $Ti_3C_2T_x$ layers, where T_x stands for surface terminal groups containing oxygen and fluorine functional groups. The electrochemical performance of $Ti_3C_2T_x$ in a variety of electrolytes was measured by cyclic voltammetry and galvanostatic charge-discharge techniques. The surface chemistry was analyzed by X-ray photoelectron spectroscopy and the intercalation mechanism was observed by X-ray diffraction.

3.2 Spontaneous Intercalation of Cations

3.2.1 Study by X-ray Diffraction

To investigate the spontaneous reaction of $Ti_3C_2T_x$ with aqueous solutions, 0.4 g of multilayer $Ti_3C_2T_x$ powder was added to 50 mL of various aqueous electrolytes, stirred for an hour with a magnetic stirrer at room temperature; then the solution was decanted after powder sedimentation; this process was repeated 5 times. The final time the solution was filtered on a hydrophilic polypropylene membrane (GH polypropylene). The powders were collected and analyzed by X-ray diffraction. X-ray diffraction patterns of $Ti_3C_2T_x$ and treated $Ti_3C_2T_x$ (here in LiOH as an example) are shown in Figure 36. As described in Chapter 2, the c-lattice parameter which defines the distance between single Ti_3C_2 sheets of $Ti_3C_2T_x$ and treated $Ti_3C_2T_x$ can be calculated directly from the (00n) peaks according to equation 29:

$$d_{(00n)} = n\lambda/2\sin(\theta) = n \times d_{c-\text{lattice parameter}} \quad (29)$$

The (002) peak was always the most intense peak of the pattern, therefore calculations and discussions focused on this peak. In the case of $Ti_3C_2T_x$ the c-lattice parameter was calculated to be 20.3 Å. The intercalation of species between layers induced an increase in the c-lattice parameter, noticeable by the 2θ downshift of the (00n) peak position compared to the untreated $Ti_3C_2T_x$.

Figure 37 shows the X-ray diffraction patterns of $Ti_3C_2T_x$ obtained after treatment in various electrolytes. The aqueous solutions selected were 1M sulfuric acid (H_2SO_4), 1M lithium hydroxide (LiOH), 1M sodium hydroxide (NaOH), 1M potassium hydroxide (KOH), 1M potassium acetate (KOAc), 1M potassium sulfate (K_2SO_4), 3M sodium acetate (NaOAc), 1M lithium sulfate (Li_2SO_4), 1M sodium sulfate (Na_2SO_4) and 1M

magnesium sulfate ($MgSO_4$). A 2θ downshift was observed in all cases except for $Ti_3C_2T_x$ treated by 1M H_2SO_4. A possible explanation was that the distance between two Ti_3C_2 layers was large enough that the intercalation of small H^+ had no effect on the c-lattice parameter. Another explanation could be that the as-synthesized $Ti_3C_2T_x$ already contained intercalated H^+ cations that came from the acidic environment during the synthesis with hydrofluoric acid.

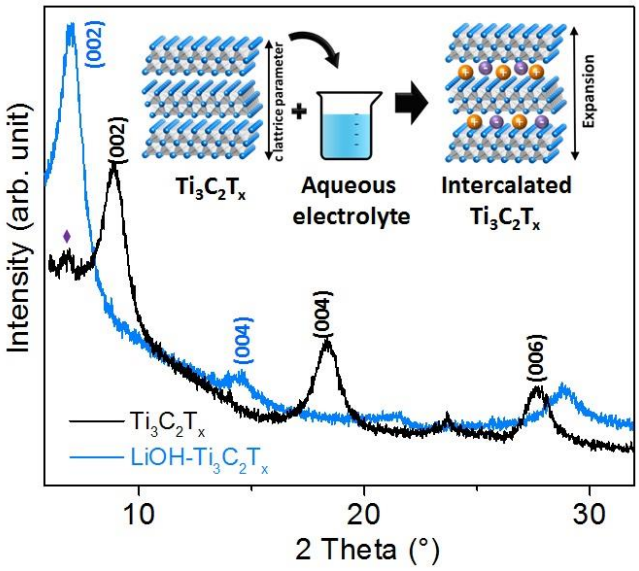

Figure 36: X-ray diffraction pattern of $Ti_3C_2T_x$ and LiOH-$Ti_3C_2T_x$. Inset is a schematic of the intercalation process.

Figure 37.a shows $Ti_3C_2T_x$ treated in KOH, KOAc and K_2SO_4. The three chemicals share the same cation, thus the difference in their c-lattice parameter is attributable to other factors, such as pH or anion size. Yet, despite the acetate ion being larger than the hydroxide ion, KOH- $Ti_3C_2T_x$ had a larger c-lattice parameter than KOAc- $Ti_3C_2T_x$, thus the difference could not be directly correlated with the size of the anion. The same

conclusion could be deduced from the results presented in Figure 37.b where $Ti_3C_2T_x$ was treated with three chemicals that shared the same Na^+ cation.

Figure 37.c shows $Ti_3C_2T_x$ treated in 1M LiOH, NaOH and KOH. In this case, the anion and the pH were the same for the three solutions; therefore the differences observed should be attributed to the cation nature. Slightly different shifts were observed but it did not correlate with the cation size. Although the downshift of the (002) peaks was not exactly the same, they were more similar to each other than with any of the other electrolytes investigated, which demonstrated the importance of the pH.

Figure 37.d shows $Ti_3C_2T_x$ treated in 1M H_2SO_4, Li_2SO_4 and $MgSO_4$. Here, the anion was the same but the cation and pH were different. As explained before, no shift was recorded after treatment in H_2SO_4. The intercalation from Li_2SO_4 was comparable to results obtained with Na_2SO_4 and K_2SO_4. The shift obtained in the case of the $MgSO_4$ treatment is the largest observed so far. As the pH of 1M Li_2SO_4, Na_2SO_4, K_2SO_4 and $MgSO_4$ were similar; it suggested that the cation valence had an effect on the lattice expansion. To conclude, the shift depends on both pH and valence of the cation.

Energy-dispersive X-ray spectroscopy analysis of $Ti_3C_2T_x$ after treatment in a few electrolytes was performed in order to determine whether the cations or the anions were intercalated into $Ti_3C_2T_x$ layers. Results are presented in Table 5 and confirmed the presence of the cations while the anion (sulfur) was not detected. This implied that the cations intercalated between the $Ti_3C_2T_x$ layers.

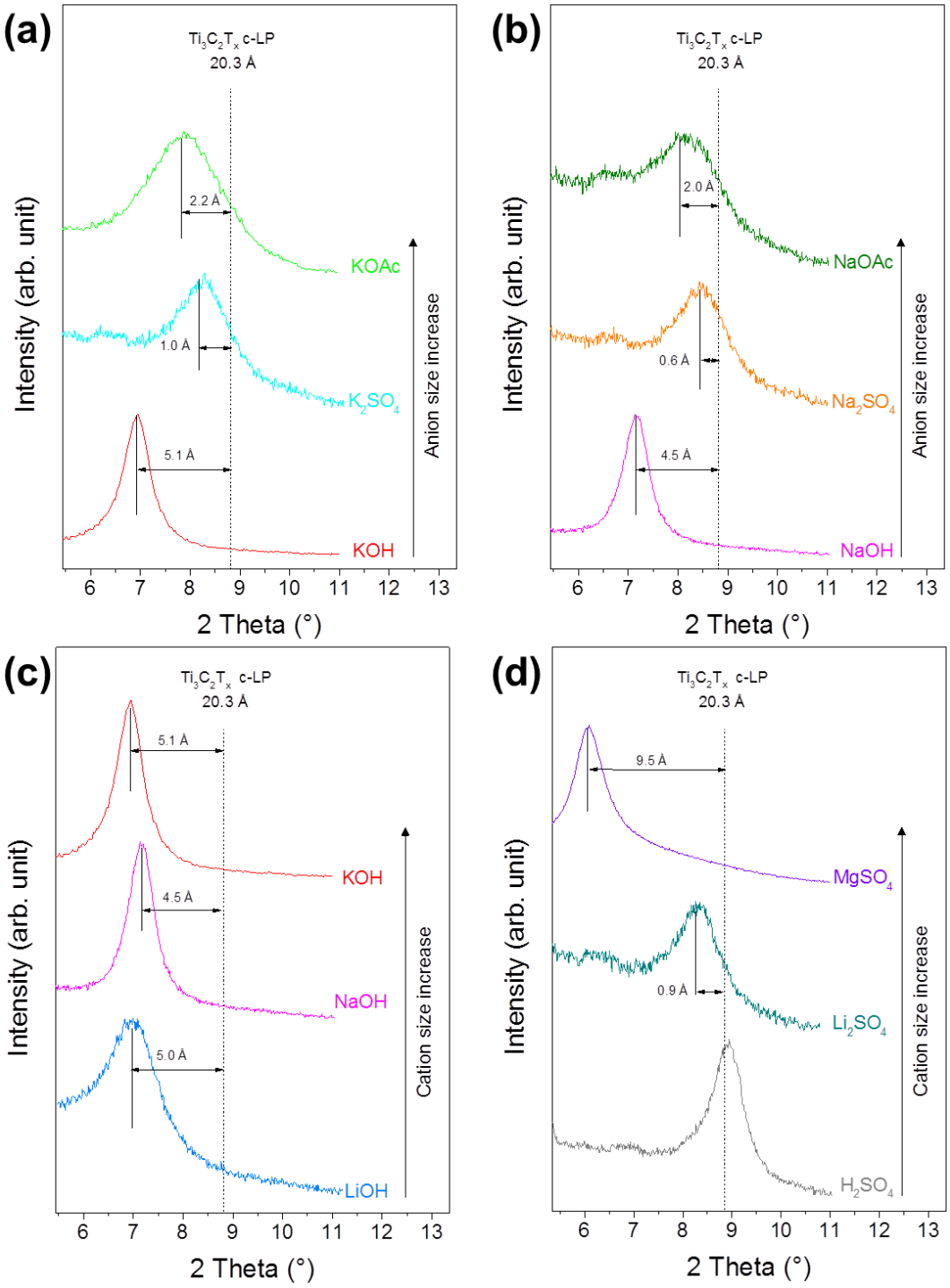

Figure 37: X-ray diffraction patterns of $Ti_3C_2T_x$ after treatment in electrolytes with different anions (a-b) and different cations (c-d).

Table 5: Energy-dispersive X-ray spectroscopy analysis of $Ti_3C_2T_x$-based powders.

Material	Atomic %					
	Ti	C	O	F	S	Cation of electrolyte
$Ti_3C_2T_x$	30.0	14.8	16.0	18.9	-	-
KOH-$Ti_3C_2T_x$	30.0	21.2	30.9	11.4	-	3.2
NaOAc-$Ti_3C_2T_x$	30.0	16.2	18.2	27.4	-	5.5
K_2SO_4-$Ti_3C_2T_x$	30.0	17.8	8.4	15.4	0	1.4
Na_2SO_4-$Ti_3C_2T_x$	30.0	17.5	12.9	15.8	0	1.0

*Values of the carbon, oxygen and fluorine content are approximate, since spectra were collected from the rolled $Ti_3C_2T_x$-based electrode, which contained carbon additive (contributes to C and O content) and PTFE binder (contributes to C, O and F content) (*172*).

In most 2D materials, the intercalation of ions is electrochemically driven or is limited by diffusion and kinetics (*173, 174*). In order to shed light on the spontaneous intercalation mechanism, X-ray diffraction spectra of $Ti_3C_2T_x$ in an *in-situ* cell containing a 1M $MgSO_4$ solution was recorded during cycling, as shown in Figure 38. In the first pattern (yellow) no shifts were observed but with time the peak at 9° started to decline while a peak at lower angles emerged. In the second scan the two peaks were clearly identifiable. The emerging peak shifted from 6.7° to 6° in the following scans. This

suggests that the intercalation reaction of $MgSO_4$ into $Ti_3C_2T_x$ layers was limited by diffusion.

Similar experiments (not reported here) were attempted with $Ti_3C_2T_x$ in 1M KOH and 3M NaOAc but the (002) downshift was observed immediately. This suggested that the diffusion and kinetic parameters of the intercalation depended on the electrolyte used but further work is needed to better understand the mechanism.

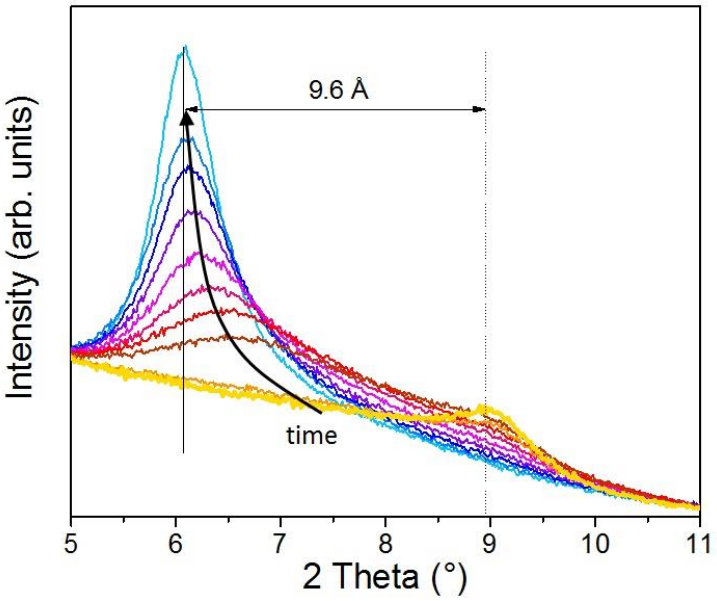

Figure 38: X-ray diffraction patterns of $Ti_3C_2T_x$ during intercalation from 1M $MgSO_4$. Each pattern took 20 min to be recorded. Vertical dashed lines indicate the original position of the (002) peak.

3.2.2 Delamination

Similar to the spontaneous intercalation of aqueous electrolytes described in the previous pages, Mashtalir *et al.* demonstrated the intercalation of large organic

molecules, in particular dimethyl sulfoxide (DMSO) (*159*). The intercalation of DMSO was demonstrated by X-ray diffraction, as shown in Figure 39. The intercalation had the effect of weakening the bond between $Ti_3C_2T_x$ layers. Thanks to this, it was possible to fully separate the layers by ultrasonication. This procedure, called delamination, is described in detail in Chapter 2. Figure 39 shows the X-ray diffraction pattern obtained for the freestanding delaminated Ti_3C_2 film prepared by filtration, noted as d-$Ti_3C_2T_x$. A peak was observed at 6.16° meaning that the delaminated layers recombined with the same orientation. The d-$Ti_3C_2T_x$ (002) peak was at a lower angle than the DMSO-$Ti_3C_2T_x$ (002) peak; proving that DMSO molecules were not present between layers and probably deintercalated during the washing or ultrasonication steps.

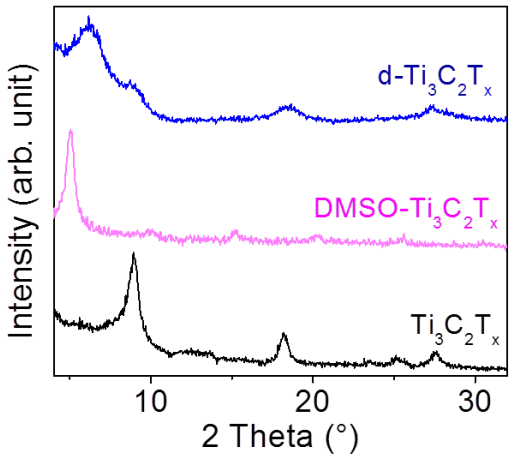

Figure 39: X-ray diffraction patterns of $Ti_3C_2T_x$, DMSO-$Ti_3C_2T_x$ and d-$T_3C_2T_x$.

3.3 Surface Modification

The surface chemistry of the as-synthesized $Ti_3C_2T_x$ was rich in oxygenated and fluorinated groups (*155*). After $Ti_3C_2T_x$ treatment in various aqueous electrolytes, cations were found in the material but the nature of the bond between the cation and the $Ti_3C_2T_x$ surface was not known. The hypothesis deduced earlier was that the intercalation of cations induced a change in the c-lattice parameter that depended on the pH and cation valence. Theoretical predictions suggested that treatment in basic aqueous solutions should replace –F terminal groups with hydroxyl groups as Ti-F becomes unstable at high pH (*175*). Moreover the delamination process demonstrated that the morphology of MXenes can be modified.

In the following, the goal was to investigate the morphology and surface chemistry modifications of $Ti_3C_2T_x$ after two different processes: 1) the intercalation of K^+ cations between $Ti_3C_2T_x$ layers from treatment in 1M KOH and 1M KOAc as described previously; 2) the delamination of individual $Ti_3C_2T_x$ layers after the intercalation of DMSO and ultrasonication (*159*). To monitor these processes, the structure and chemistry of the $Ti_3C_2T_x$ electrodes were analyzed by scanning electron microscopy (Zeiss, Supra 50VP, Oberkochen, Germany) and X-ray photoelectron spectroscopy (VersaProbe 5000, Physical Electronics, Inc., USA).

3.3.1 Observation by Scanning Electron Microscopy

The morphologies of $Ti_3C_2T_x$, KOH-$Ti_3C_2T_x$ and d-$Ti_3C_2T_x$ were observed using scanning electron microscopy, as shown in Figure 40 $Ti_3C_2T_x$ and KOH-$Ti_3C_2T_x$ images showed aggregates of multilayered particles. Although the K^+ intercalation conserved the exfoliated morphology, it was noted that the layer thickness appeared to be larger than

before intercalation as if the layers were glued together. This phenomenon is commonly observed in intercalated graphite (*176, 177*).

d-$Ti_3C_2T_x$ images showed layers on top of each other forming a continuous ordered film and no multilayered $Ti_3C_2T_x$ aggregate was noticeable. This led to an increase in the specific surface area up to 100 m^2/g while $Ti_3C_2T_x$ and KOH-Ti_3C_2 specific surface areas are about 20 m^2/g (*159*). As described in Chapter 2, the d-$Ti_3C_2T_x$ film electrode was prepared by filtration and did not contain any binder. A free standing and flexible film was obtained thanks to the formation of a network of layers overlapping (similarly to graphene (*121*)).

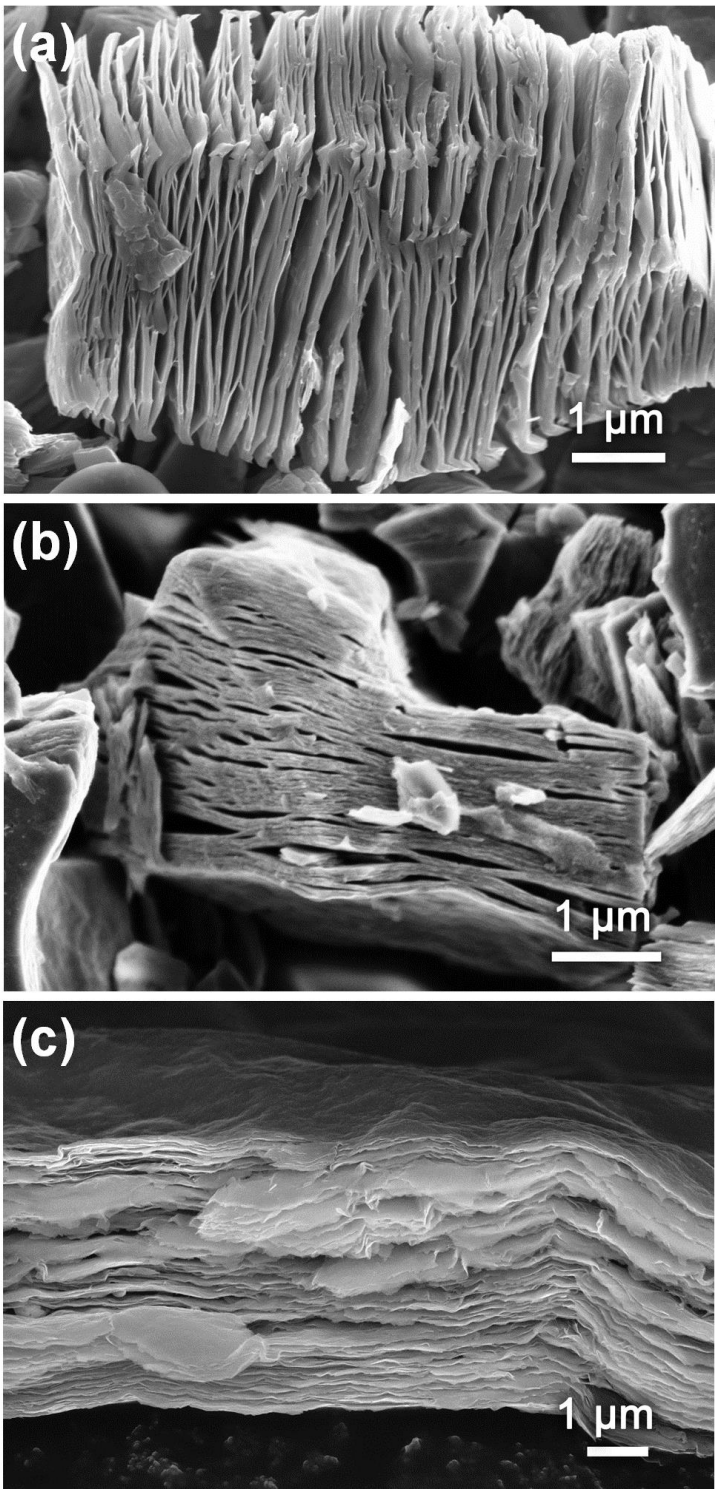

Figure 40: Scanning-electron microscope images of $Ti_3C_2T_x$ (a), KOH-$Ti_3C_2T_x$ (b) and d-$Ti_3C_2T_x$ (c) (adapted from (*178*)).

3.3.2 X-ray Photoelectron Spectroscopy

X-ray photoelectron spectroscopy was used to characterize the surface chemistry of the samples. High-resolution X-ray photoelectron spectroscopy spectra of the samples ($Ti_3C_2T_x$, KOH-$Ti_3C_2T_x$, KOAc-$Ti_3C_2T_x$ and d-$Ti_3C_2T_x$, shown in Figure 41.a-c) in the F 1s region indicated that the $Ti_3C_2T_x$ sample contained a large amount of F-terminated Ti (Figure 41.a). It was also noticed that AlF_3 salt residue from MAX phase etching was only present in the KOAc-$Ti_3C_2T_x$ and $Ti_3C_2T_x$ samples. It was completely removed after KOH or DMSO treatment. The intensity of the Ti-F peaks decreased in the order d-$Ti_3C_2T_x$, KOAc-$Ti_3C_2T_x$, KOH-$Ti_3C_2T_x$, being the lowest for the latter one. The signal of the Ti-F component, which was initially at 684.4 eV, shifted toward a higher-binding energy as F was removed from Ti as fluoride salt.

Due to the 2D-nature of the $Ti_3C_2T_x$, oxidation did not proceed homogeneously and likely started from the outer edges of the $Ti_3C_2T_x$ grains, giving oxides and mixed carboxides (TiC_xO_y) at the flake edges and on the outermost surface layer of the multilayer particle, while $Ti_3C_2T_x$ remained in the center of the grain. This inhomogeneity gave rise to the broadened and convoluted spectra seen in the Ti 2p region (Figure 41.b). In this region, the Ti-carbide photoemission arises from $Ti_3C_2T_x$, while the Ti (II) and Ti (III) components arise from these mixed oxides and carboxides, and the Ti (IV) component arises from TiO_2 present on the surface of the grains as oxidation goes to completion. These spectra also included a component for Ti-F that became less prominent and merged with that for Ti (IV), likely as a result of the formation of a small amount of the intermediate, fluorinated TiO_2, as hydroxyl groups replaced the –F termination during the oxidation of the outer surface of $Ti_3C_2T_x$. This region also

indicated oxidation of the surface of the Ti3C2Tx grains to Ti (IV) (TiO2) for all modified $Ti_3C_2T_x$ samples. Accordingly, instead of F-termination, the KOH-$Ti_3C_2T_x$, KOAc-$Ti_3C_2T_x$ and d-$Ti_3C_2T_x$ surfaces were terminated with oxygen-containing groups. High-resolution spectra of the samples in the K 1s region (Figure 41.c) revealed two components, the first for K^+ that was strongly electrosorbed and the second component suggests that K^+ was present as salt, probably KF. The electrosorbed K^+ is much more prevalent in KOAc-$Ti_3C_2T_x$ than in KOH-$Ti_3C_2T_x$. Figure 41.d shows a schematic summarizing these two chemical modification paths for $Ti_3C_2T_x$.

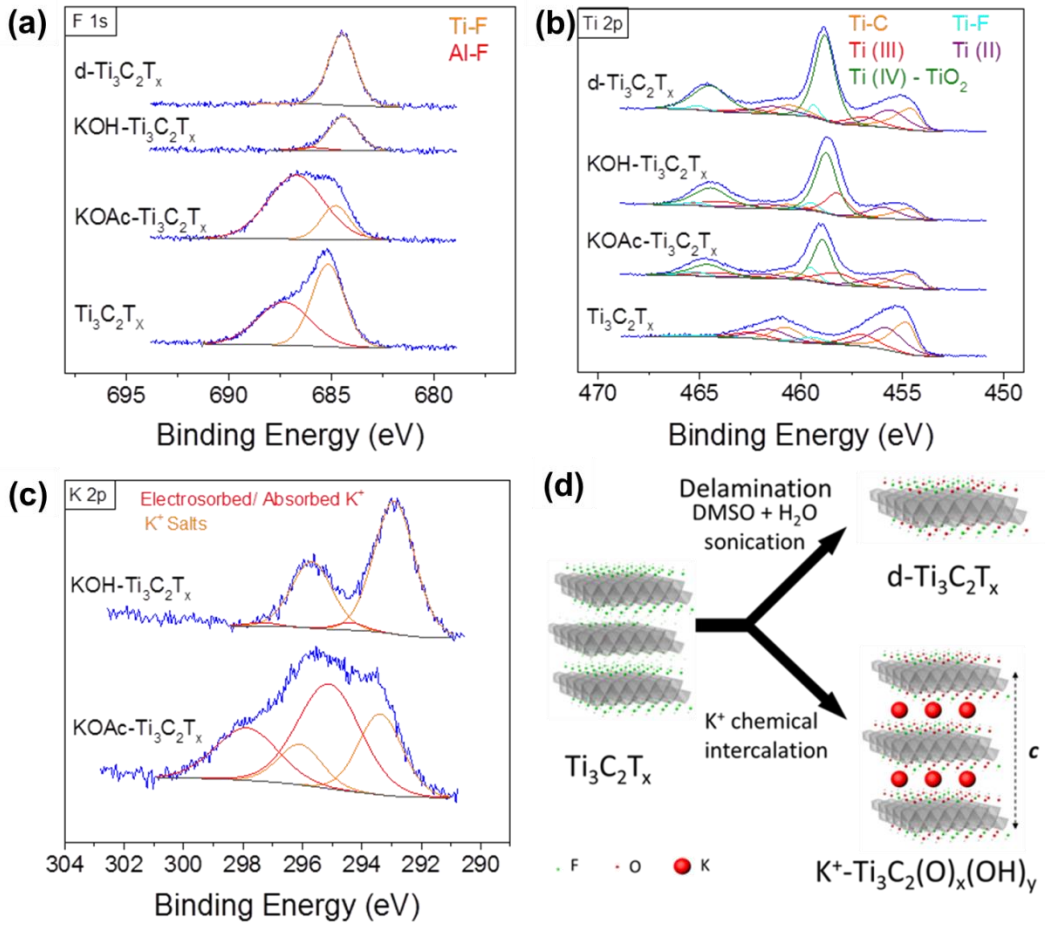

Figure 41: Characterization data of Ti_3C_2-based materials after surface modification in various intercalation agents. High-resolution X-ray photoelectron spectroscopy spectra in the F 1s region (a), the Ti 2p region (b), and K 2p region (c). Schematic illustration of the modifications of $Ti_3C_2T_x$; delamination and intercalation of K^+ (d) (adapted from (*178*)).

3.4 Electrochemical Characterizations

The X-rays diffraction and X-rays photoelectron spectroscopy experiments demonstrated that a spontaneous intercalation reaction modifying the surface chemistry can occur when $Ti_3C_2T_x$ is in contact with different electrolytes. However the objective of this work was to investigate the electrochemical behavior of $Ti_3C_2T_x$. For this purpose,

$Ti_3C_2T_x$ electrodes were prepared by mixing the dried powder in ethanol with 5 wt. % polytetrafluoroethylene binder (60 wt.% in H_2O, Sigma Aldrich) and 5 wt. % carbon black (Alfa Aesar), followed by rolling and cutting the electrode films into 7 mm diameter disks with thicknesses between 50 µm and 70 µm.

3.4.1 Results in Various Aqueous Electrolytes

A large array of electrolytes were selected to observe the response to different electrolyte properties (stability window, pH, conductivity, cation and anion etc). The aqueous solutions selected were the same as used in previous tests: 1M sulfuric acid (H_2SO_4), 1M lithium hydroxide (LiOH), 1M sodium hydroxide (NaOH), 1M potassium hydroxide (KOH), 1M potassium acetate (KOAc), 1M potassium sulfate (K_2SO_4), 3M sodium acetate (NaOAc), 1M lithium sulfate (Li_2SO_4), 1M sodium sulfate (Na_2SO_4) and 1M magnesium sulfate ($MgSO_4$).

The resulting cyclic voltammograms using a three-electrode Swagelok® cell with Ag/AgCl as reference electrode and overcapacitive activated carbon as counter electrode at 20 mV/s as shown in Figure 42. The main advantage of this electrochemical configuration was that the counter electrode potential was almost constant and therefore it allowed the study of the behavior of the working electrode over the total potential range.

Unlike what was observed for graphite, there was no irreversible capacitance loss during the first cycle for any of the studied electrolytes (*179*).The conductivities of all electrolytes are presented in Table 6. As explained extensively in Chapter 1 and 2 the rectangular shaped cyclic votammograms indicated a capacitive behavior.

Rectangular cyclic voltammograms were obtained in all electrolytes, with some broad peaks noticeable in some cases. Curiously the peaks were located at -0.2V vs. Ag in the

following electrolytes; NaOAc, KOAc, Na_2SO_4, K_2SO_4, $MgSO_4$, H_2SO_4. Further work is needed to identify the reaction. As explained in detail in Chapter 1, the presence of peaks in cyclic voltammograms is due to redox reactions. The combination of an overall rectangular shaped cyclic voltammogram with few broad peaks is commonly observed in pseudocapacitive materials, such as RuO_2, as described in detail in Figure 12.

The performance of $Ti_3C_2T_x$ electrodes tested at different scan rates is summarized in Figure 42.f. The specific capacitances were calculated by integrating the reduction portions of the cyclic voltammograms. The capacitances obtained at 2 mV/s were to be found between 45 F/g and 108 F/g. These results were quite high for such low specific surface area electrodes. Indeed, the capacitance due to the double layer was directly proportional to the specific surface area, as described by equation 7. However, $Ti_3C_2T_x$ electrodes had a moderate specific surface area of 23 m^2/g (*159*) which was very small compared to electrochemical double layer capacitor electrodes such as activated carbon (2000 m^2/g). If double layer capacitance were the only operative mechanism, the capacitance for this material should be lower. It is important to note that the capacitances obtained greatly depended of the electrolyte used.

The cyclic voltammograms obtained with electrolytes of same valence, of same anion and of same pH were compared to study the effect of cation size on the electrochemical behavior. No clear dependence on cation size could be deduced since results with K^+ were better than Na^+ with hydroxide anions (Figure 42.a) but the opposite order appeared with acetate anions (Figure 42.b).

The responses in the Li_2SO_4, Na_2SO_4, K_2SO_4 and $MgSO_4$ (Figure 42.c-d) were distinctively different. This was in agreement with the fact that the cations were

intercalating, and not the anions. The best performance among sulfate electrolytes with close to neutral pH was obtained with $MgSO_4$ (up to 82 F/g). As the conductivity in $MgSO_4$ was the lowest, the better performance was suggested to be attributed to the divalence of Mg^{2+}. However other electrolytes with multivalent cations (1M $Al_2(SO_4)_3$ and 1M $Al(NO_3)_3$) were investigated by Lukatskaya *et al.* (*172*). Their performances were lower than with $MgSO_4$ even if the $Al(NO_3)_3$ conductivity was higher (110 mS/cm^2). Therefore no direct link between a cation's valence and electrochemical performance could be concluded.

The highest capacitances among all electrolytes studied were obtained in 1M H_2SO_4 with capacitances up to 108 F/g at 2 mV/s. This electrolyte had the best conductivity but the lowest potential window because of the low pH. Broad peaks at -0.2V vs. Ag were well defined. Recent work based on chronoamperometry (imposing a potential while recording the current response *vs*. time) at different potentials suggested that these peaks in H_2SO_4 were associated with hydrogen storage but no study in the other electrolytes where this peak was observed has been performed to confirm it (*180*).

To conclude, the best performances were obtained with 1M H_2SO_4 and 1M $MgSO_4$, which had very different physical properties (different cation sizes, different conductivities, different pH). In the following section, effort will be focused on understanding the energy storage mechanism.

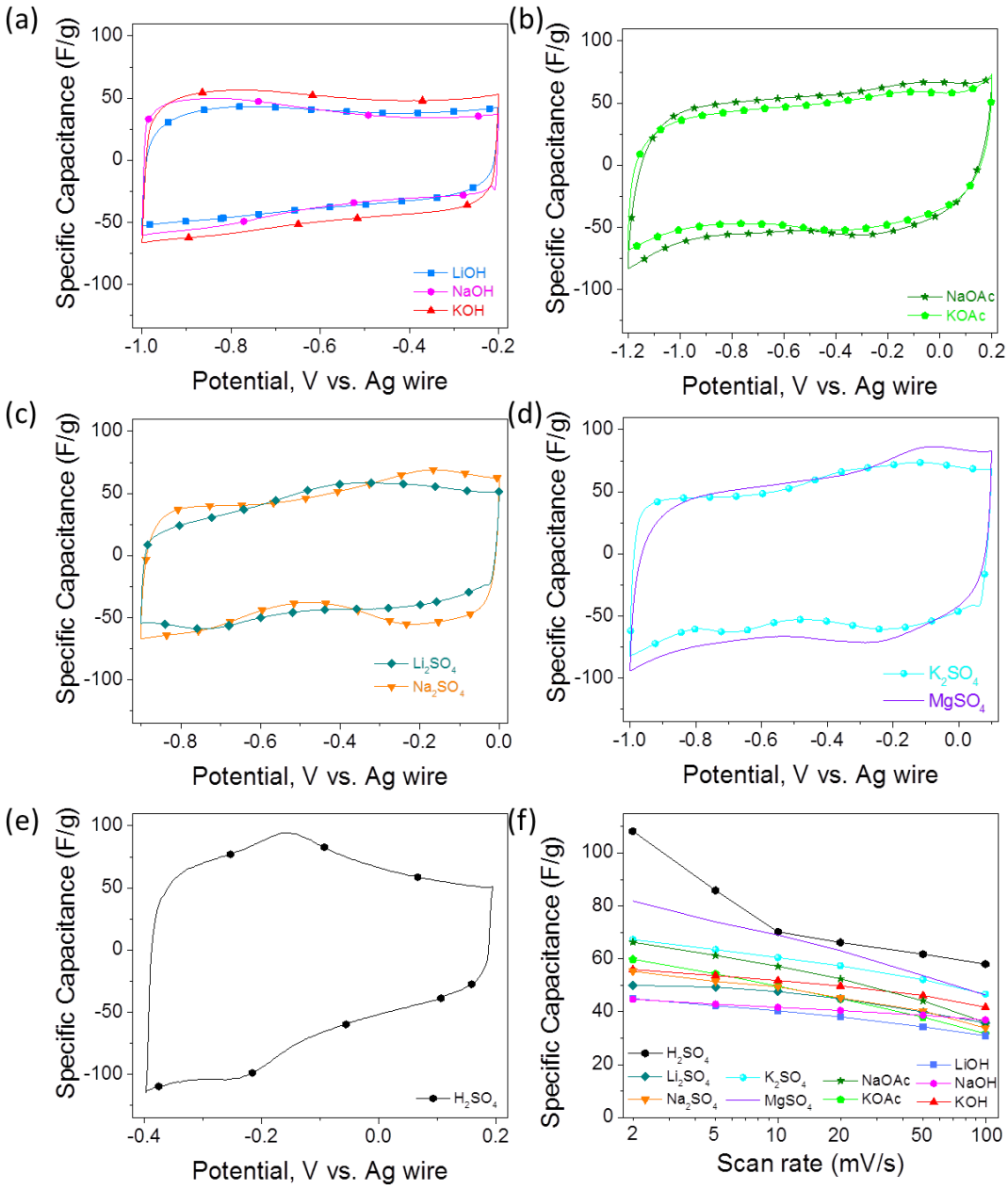

Figure 42: Electrochemical performance of $Ti_3C_2T_x$ in various electrolytes; cyclic voltammograms at 20 mV/s in LiOH, NaOH and KOH (a) NaOAc and KOAc (b), Li_2SO_4 and Na_2SO_4 (c) K_2SO_4 and $MgSO_4$ (d) H_2SO_4 (e). Summary of rate performances in the different aqueous electrolytes (f).

Table 6: Ionic conductivities of the various aqueous electrolytes used in electrochemical experiments (adapted from (*181, 182*)).

Electrolyte	Conductivity, (mS/cm)
1 M H_2SO_4	265
1 M KOH	191
1 M LiOH	150
1 M NaOH	141
1 M K_2SO_4	100
1 M Na_2SO_4	100
1 M KOAc	92
3 M NaOAc	79
1 M Li_2SO_4	71
1 M $MgSO_4$	51

3.4.2 Mechanism Study by *In-Situ* X-ray Diffraction

Electrodes that store charge through double layer capacitance have an areal capacitance up to 20 µF/cm²(*4*). It can be calculated that in order to reach a capacitance of 40 F/g based on double-layer, a specific surface area of 200 m²/g is the minimum required, which is far above the value measured for $Ti_3C_2T_x$ electrodes. Therefore the double layer capacitance contribution to the total capacitance in this case is limited. To shed light on the energy storage mechanism, *in-situ* X-ray diffraction was performed

using $Ti_3C_2T_x$ electrodes. It consisted of recording the X-ray diffraction spectra at different potentials using the experimental set-up described in Chapter 2. Figure 43 shows the results in the three different electrolytes that were selected for this study; 1M KOH, 1M $MgSO_4$ and 3M NaOAc.

Confirming the results shown previously, it was observed that when $Ti_3C_2T_x$ is in contact with these aqueous electrolytes a (002) peak downshift was observed, demonstrating the spontaneous intercalation mentioned earlier. In the case of $MgSO_4$, the peaks appeared after 2 hours. The shift observed for NaOAc and $MgSO_4$ did not correspond perfectly to the values observed in Figure 36. A possible explanation was that the materials used were slightly different, for example in one case the material used was a powder treated for 6 hours in the electrolytes and in the other case it was a film electrode of untreated $Ti_3C_2T_x$ with PTFE binder and carbon black that was soaked in the electrolyte.

In-situ X-ray diffraction studies during cycling showed that electrochemical cycling leads to small changes in the c-lattice parameters. This demonstrates an intercalation process was occurring. For example, when a $Ti_3C_2T_x$ electrode was cycled in a KOH containing electrolyte, the c values fluctuated within 0.33 Å as the potential was scanned from -1 to - 0.2 V, as shown Figure 43.a. Interestingly, a slight shrinkage in c-lattice parameter was observed with increasing potential. The simplest explanation for this observation was that the positively charged ions incorporated in $Ti_3C_2T_x$ increased the electrostatic attraction between layers, in a manner analogous to what was observed for MnO_2 (*183*).

Similar behavior was observed when $Ti_3C_2T_x$ was cycled in 3M NaOAc as shown Figure 43.b. The lattice expanded and shrank by up to 0.22 Å during oxidation and reduction which was smaller than in 1M KOH. Considering that acetate anions are larger than hydroxide anions and that the capacitance at low scan rates were better in 3M NaOAc than in 1M KOH, the lower change in the lattice was attributed to the smaller size of the cation. It also further supported the hypothesis that the anions did not intercalate.

Figure 43.c shows the *in-situ* X-ray diffraction results in 1M $MgSO_4$. When $Ti_3C_2T_x$ was electrochemically cycled, here again, a slight shrinkage in c values was observed with increasing V. The shift of the (002) peak almost doubled compared to the KOH and NaOAc electrolytes (0.5 Å) and might either be due to the larger size of the cation and/or its divalence. As the same phenomenon was demonstrated in these three very different electrolytes it can be generalized that $Ti_3C_2T_x$ stores energy via an intercalation capacitance mechanism.

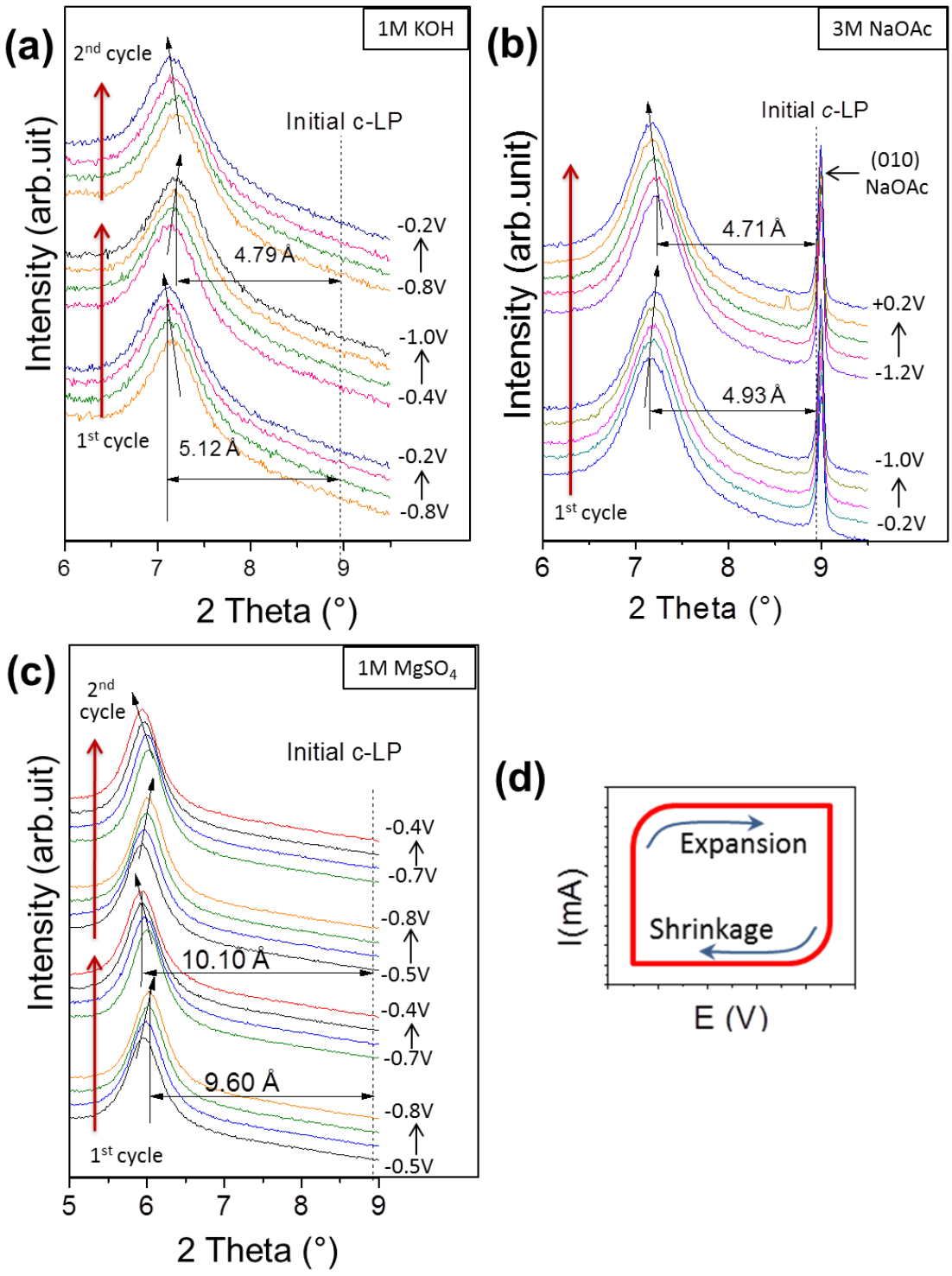

Figure 43: Electrochemical *in-situ* X-ray diffraction study of $Ti_3C_2T_x$ in 1M KOH (a), 1M $MgSO_4$ (b) and 3M (NaOAc) (c).Vertical dashed lines indicate the original position of the (002) peak. Inclined arrows show the direction of the (002) peak shift.

Illustration of cycling direction and concomitant change in c-lattice parameter (adapted from (*172*)).

3.4.3 Surface-Modified $Ti_3C_2T_x$ Performance

The effect of intercalation and delamination of the $Ti_3C_2T_x$ on its surface chemistry was studied by X-ray photoelectron spectroscopy in part II.2.2. It was confirmed that terminal fluorine was successfully replaced by oxygen-containing functional groups after the chemical intercalation of potassium acetate (KOAc-$Ti_3C_2T_x$) and potassium hydroxide (KOH-$Ti_3C_2T_x$). Delamination of $Ti_3C_2T_x$ layers, denoted d-$Ti_3C_2T_x$, led to both an increase of the specific surface area of MXene films and the modification of the surface chemistry of d-$Ti_3C_2T_x$.

Theoretical calculations using first-principles simulations recently investigated the Li, Na, K, Mg, Ca, and Al storage on MXene nanosheets (*175*, *184*). The effect of the surface chemistry on the electrochemical performance for use in batteries was systematically studied. The results demonstrated that bare MXenes had higher capacities and greater ion mobilities than the O-terminated MXenes. It was expected that the surface chemistry of MXene had an effect on the behavior in the case of supercapacitors as well because HF-synthesized MXene were terminated with –F and –OH/=O functional groups, where the –F group may be a detriment to charge storage since F^- was not known to participate in any pseudocapacitive energy storage processes.

In the following, the influence of the surface chemistry of $Ti_3C_2T_x$ on its electrochemical performance is investigated in the acidic electrolyte sulfuric acid (H_2SO_4), this electrolyte was chosen because it had the highest capacitance, with no change in the c-lattice parameter.

Figure 44.a shows the cyclic voltammograms of all samples tested at 10 mV/s sweep rate in aqueous 1 M H_2SO_4. The best performances were achieved using d-$Ti_3C_2T_x$ electrodes, with an outstanding volumetric capacitance of 520 F/cm^3 and a gravimetric capacitance of 325 F/g at 2 mV/s (Figure 44.b). It is believed the superior performance of d-$Ti_3C_2T_x$ electrodes originated from several sources. First, it was a 6 times thinner electrode, leading to better charge transfer and improved mass transfer. It also had a higher specific surface area and was denser because of its morphology (aligned MXene flakes). Nonetheless, d-$Ti_3C_2T_x$ showed a stronger dependence of performance on scan rate, which was assumed to be caused by the flakes aligning parallel to the current collector and increasing the transport path for ions as the film thickness increased.

The $Ti_3C_2T_x$, KOH-$Ti_3C_2T_x$ and KOAc-$Ti_3C_2T_x$ electrodes had the same specific surface area, therefore the difference in electrochemical performance could only be related to the differences in surface chemistry. The moderate capacitances for $Ti_3C_2T_x$ were consistent with the absence of redox activity of the F-termination. The KOAc-$Ti_3C_2T_x$ and KOH-$Ti_3C_2T_x$ electrodes exhibited similar behavior, with the latter having a higher gravimetric capacitance thanks to a lower content of F-groups (Figure 41.a). Their surfaces were terminated by oxygen-containing groups, including –OOH, =O and –OH, which are known to be responsible for pseudocapacitive behavior seen in carbon in acidic electrolytes. This hypothesis was consistent with the shape of the cyclic voltammograms presented in Figure 44.a, where the presence of a set of broad peaks at -0.2 and -0.1 V/Ref was observed. These peaks were assumed to originate from surface redox reactions of MXene, leading to changes in the degree of oxidation of titanium in MXene, which is a transition metal capable of changing oxidation degree between +3 and +4.

Figure 45.a shows the capacitance vs. cycle number dependencies obtained from galvanostatic charge-discharge curves shown in Figure 45.b. Stable capacitances of 415 F/cm^3 and 215 F/cm^3 were obtained at 5 A/g for d-$Ti_3C_2T_x$ and KOH-$Ti_3C_2T_x$, respectively. After 10,000 cycles, no significant degradation was observed. Similar electrochemical performances improvements due to the delamination process were observed in some other electrolytes (KOH, NaOAc and $MgSO_4$) by Lukatskaya *et al.* (*172*).

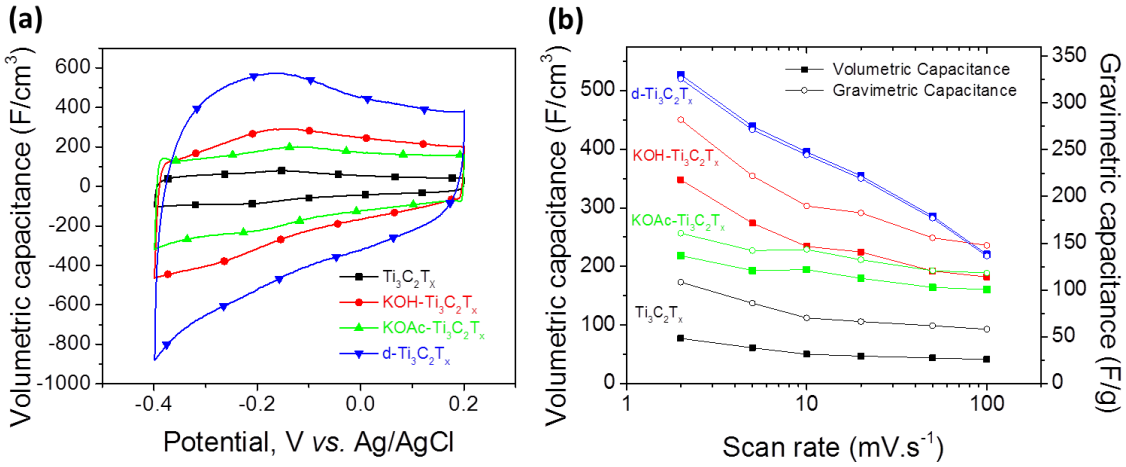

Figure 44: Electrochemical performance of Ti_3C_2-based electrodes in 1M H_2SO_4: cyclic voltammograms profiles at 10 mV/s (a). Summary of rate performance (b) (adapted from (*178*)).

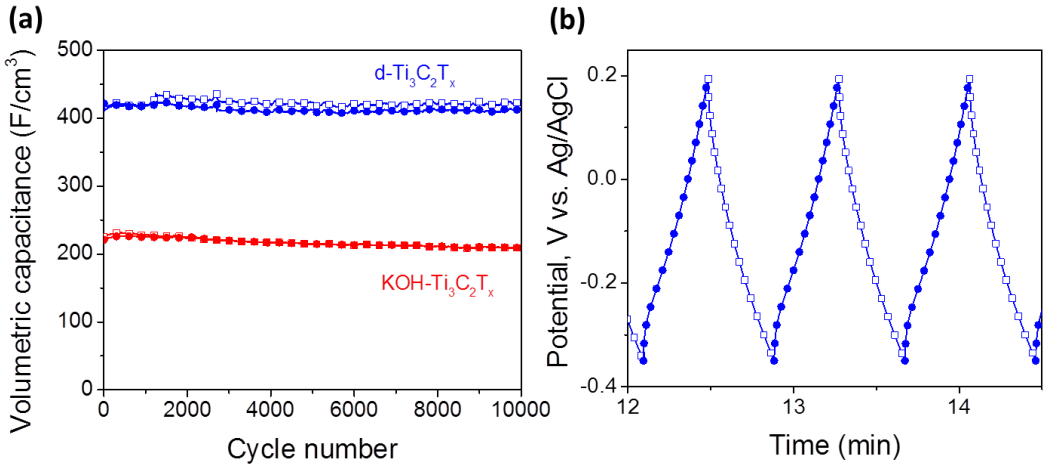

Figure 45: Charge and discharge volumetric capacitance vs. cycle number of KOH-$Ti_3C_2T_x$ and d-$Ti_3C_2T_x$ electrodes from galvanostatic cycling in 1M H_2SO_4 at 5 A/g (a). Galvanostatic charge-discharge profile of d-$Ti_3C_2T_x$ (b) (adapted from (*178*)).

3.5 Conclusions

The intercalation of a wide range of cations (Li^+, Na^+, K^+ and Mg^{2+}) between $Ti_3C_2T_x$ layers from various aqueous solutions was demonstrated. The mechanism depended on pH and the nature of the cations. The electrochemical behavior of $Ti_3C_2T_x$ was investigated in these aqueous electrolytes. The energy storage mechanism was identified to be intercalation capacitance by *in-situ* X-ray diffraction.

The best performance was observed in sulfuric acid electrolytes. The effect of intercalation and delamination of the two-dimensional titanium carbide, $Ti_3C_2T_x$ (MXene) on its surface chemistry and electrochemical capacitance was demonstrated. The change in surface chemistry (-F repaced by –O) led to a 4-fold increase in the capacitance in sulfuric acid, demonstrating a pseudocapacitive contribution to the electrochemical behavior of MXene. A recent study using *in-situ* X-ray absorption

spectroscopy confirmed the change of oxidation state of Ti atoms in $Ti_3C_2T_x$ (*180*). Later, the performance of $Ti_3C_2T_x$ itself was improved by optimizing the d-$Ti_3C_2T_x$ electrode formulation (*162*) and a new synthesis route of $Ti_3C_2T_x$ (*161*).

The delamination process gave rise to an electrochemical capacitance of 520 F/cm^3 at 2 mV/s, the highest volumetric capacitance reported for this material. This value was dramatically higher than the 60-100 F/cm^3 for activated graphene (*118*, *185*) or 180 F/cm^3 for micrometer-thin carbide-derived carbon electrodes (*186*, *187*). Extreme values of 1200 F/cm^3 (*188*) and 640 F/cm^3 (*189*) for MnO_2 hybrid electrodes were obtained on *thin films* of supported nanoparticles and cannot be compared with MXenes electrodes. Moreover, freestanding d-$Ti_3C_2T_x$ electrodes were highly flexible which is promising for wearable energy storage devices (*190*). The fact that cations of different sizes and valences could be accommodated between the $Ti_3C_2T_x$ layers opens the door for the use of MXene in batteries going beyond Li-ions and metal-ion capacitors.

CHAPTER 4: MXenes for Na-ion Capacitors

4.1 Introduction

One of the most important applications of MXene are electrodes for lithium-ion batteries. For example, Ti_3C_2, V_2C and Nb_2C have recently shown better performance than Ti_2C, with reversible capacities about 400 mAh/g, 300 mAh/g and 200 mAh/g at 1C rate respectively (*159, 191*). Unfortunately, all data showed a large working potential window (from 0V to 2.5V) and a sloping charge-discharge curve which are drawbacks for batteries.

However, such a drawback becomes a key advantage for assembling hybrid devices, such as lithium and sodium-ion capacitors. Ti_2C was proposed for Li-ion capacitors and exhibited 70 mAh/g 10C rate (Figure 26) (*157*). All MXenes tested for lithium-ion batteries (Ti_3C_2, Nb_2C and V_2C) were expected to be suitable for lithium-ion capacitors. In particular, delaminated Ti_3C_2 electrodes have shown excellent power capability in batteries (Figure 27) and a full cell could be assembled with a suitable battery-type counter electrode. However, the results shown in the previous chapter highlighted the innovative possibility to go beyond lithium with energy storage solutions based on the inexpensive sodium chemistry. Indeed, the fast intercalation of large cations between $Ti_3C_2T_x$ layers from various aqueous electrolytes was demonstrated, including with sodium-based electrolytes.

Considering that Na^+ intercalation into $Ti_3C_2T_x$ from aqueous electrolytes led to good performance, the Na^+ intercalation into MXene-based electrodes should be investigated for sodium-ion capacitors in organic electrolytes in order to increase the potential range.

Herein, the work reported aimed to identify the most suitable MXene electrode to reach the highest energy and power densities for use in the assembly of a full sodium hybrid cell.

4.2 Selection of Suitable MXene Electrodes

Results in aqueous supercapacitors and lithium-ion batteries emphasized that the electrochemical performance depended on the composition of MXene (M and X elements) as well as its surface chemistry. Therefore, before creating a full Na-ion capacitor the electrochemical behavior of all synthesized MXene in sodium based organic electrolyte was investigated. The synthesis conditions of MXenes are described in Chapter 2. MXenes were terminated with functional groups (-OH and -F) and the formulae are annotated with T_x to account for these surface terminations.

Table 7 shows an estimated theoretical capacitance (Q) of MXene using the following equations:

$$M_{n+1}X_n + yNa^+ + ye^- \leftrightarrow Na_yM_{n+1}X_n$$

$$Q = \frac{yF}{3.6 \times M} \tag{30}$$

Where: y is the number of sodium ions intercalated, F the Faraday constant (96485 C/mol) and M the molar mass (g/mol).

Table 7: Capacitance estimation.

$M_{n+1}X_n$	$Ti_3C_2T_x$	Ti_3CNT_x	Nb_2CT_x	Ti_2CT_x	$TiVCT_x$	$Ti_{1.5}V_{1.5}CT_x$	V_2CT_x
Q (mAh/g)	160	158	135	249	242	156	235

Calculation did not take into account the surface chemistry and considered the intercalation of a single sodium per MXene formula.

4.2.1 Comparison of Cyclic Voltammograms

A two-electrode Swagelok® cell was used for half-cells with metallic sodium as counter and reference electrodes separated by a glass fiber separator (Whatman® GF/A, Sigma Aldrich). The working electrode was a given MXene powder mixed with 20 wt. % of carbon black (Alfa Aesar) to ensure good conductivity. The electrolyte used was 1M $NaPF_6$ in EC:DMC (1:1). Figure 46 shows the cyclic voltammograms of carbon black and of all synthesized MXene materials. The result with carbon black showed that a reaction occured below 0.5V vs. Na^+/Na. The cell was cycled between 0 and 4V vs. Na^+/Na in order to observe the electrolyte reaction occurring at high potential and determine the potential stability range (3.7 V). As expected the electrochemical behavior varied greatly according to the MXene composition.

The corresponding capacities are shown in Figure 47. Surprisingly the performance of Ti_2CT_x and Nb_2CT_x were the lowest observed whereas good performances were achieved for lithium-ion batteries using the same materials. In all MXenes, an irreversibility was observed during the first cycle, originating from the formation of the solid electrolyte interphase as well as irreversible processes, such as reactions between Na^+ and residual

water or unwashed etching products from the synthesis. A large degree of irreversibility was observed in particular for Ti_3CNT_x (70% capacity loss) lessening the interest of this material for commercial rechargeable energy storage application (*5*).

As the performance also depends on the surface chemistry it was difficult to attribute the electrochemical behavior solely to the composition of M and X in MXenes. However, it appears that $TiVCT_x$ and $Ti_{1.5}V_{1.5}C_2T_x$ cyclic voltammograms were very similar, suggesting that there could be peaks characteristic to the composition.

The electrochemical performances of $Ti_3C_2T_x$, $TiVCT_x$, $Ti_{1.5}V_{1.5}C_2T_x$ and V_2CT_x were on the same order of magnitude (150 mAh/g). $Ti_3C_2T_x$ and V_2CT_x could only be cycled over a limited potential range. Indeed, $Ti_3C_2T_x$ capacitive behavior was achieved below 2.5 V, which was suitable for negative electrodes, while V_2CT_x had a redox peak above 3V, suitable for positive electrodes. To conclude, $Ti_3C_2T_x$ and V_2CT_x were selected for further investigation because they had lower irreversibility, better defined redox peaks and their synthesis condition was better known.

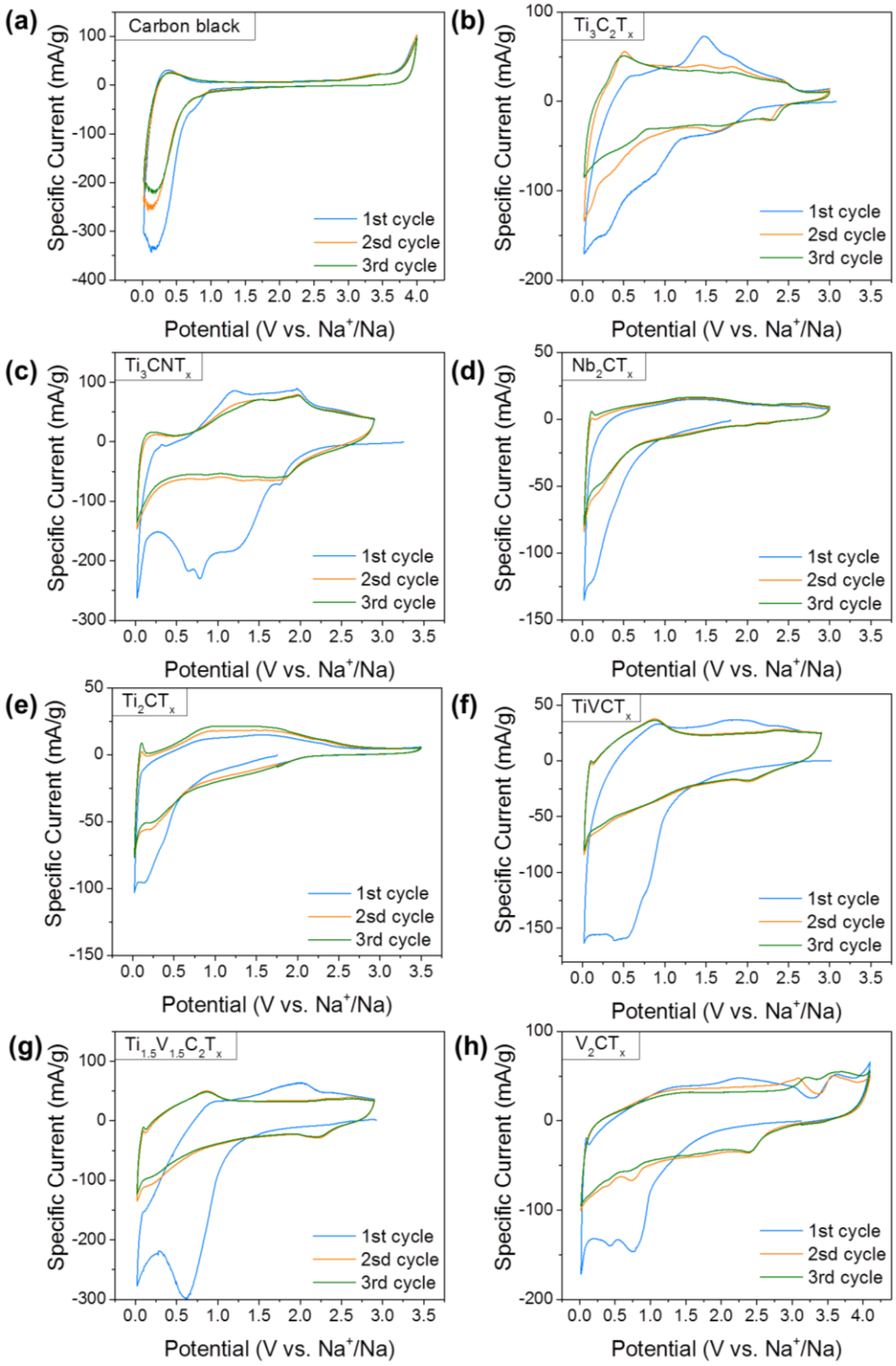

Figure 46: Cyclic voltammetry of carbon black (a) and MXene (b-h) at 0.2 mV/s in 1 M $NaPF_6$ in EC:DMC.

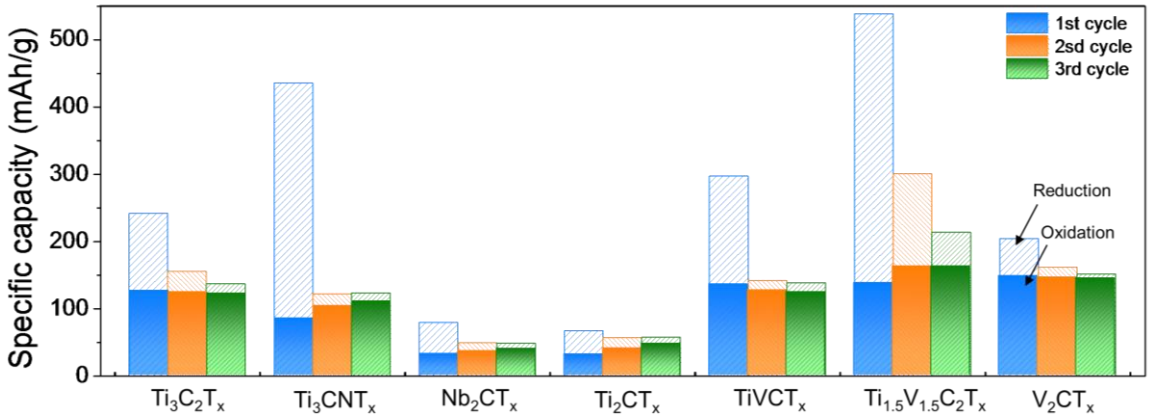

Figure 47: Capacity of all MXenes calculated from cyclic voltammetry at 0.2 mV/s.

4.3 $Ti_3C_2T_x$

$Ti_3C_2T_x$ is the most studied MXene. In the previous chapter, it was demonstrated that its electrochemical behavior in a given electrolyte could be modified by tuning its surface chemistry and morphology. Preliminary experiments in half-cell sodium-ion batteries showed a capacity above 120 mAh/g, which is promising in the field of sodium-ion battery. First, the charge storage mechanism of $Ti_3C_2T_x$ was investigated. Then, inspired by the previous results in supercapacitors, it was attempted to improve the electrochemical performance by chemical treatment.

4.3.1 Energy Storage Mechanisms

In order to investigate the mechanism of energy storage, electrochemical *in-situ* X-ray diffraction experiments were performed. The *in-situ* cell used is described in Chapter 2 using a mixture of 80 wt. % $Ti_3C_2T_x$ and 20 wt. % carbon black (Alfa Aesar) powder. Figure 48 shows the X-ray diffraction spectra during galvanostatic-charge discharge at 0.03 A/g.

During the first charge a downshift of the (00n) peaks, here (002) and (004), were observed. This was attributed to sodium intercalation between $Ti_3C_2T_x$ layers. According to equation 4, the capacity was converted into the number of sodium ions intercalated and revealed that almost 3 cations were inserted into $Ti_3C_2T_x$ per formula unit, although the calculation overestimated this value because it did not take into account the solid electrolyte interphase formation nor the side reaction with impurities. Regardless, the c-lattice parameter expansion during the first charge was 1.4 Å, which was larger than the ionic radius of neat Na^+. This suggested that more than 1 layer of sodium ions could be intercalated into $Ti_3C_2T_x$, but an effect of the solvation shell was not excluded.

During the next charge and discharge, a reversible cell expansion and shrinkage of 0.4 Å was observed. $Ti_3C_2T_x$ did not fully recover to its original lattice size. This phenomenon was previously observed upon cation intercalation from aqueous electrolytes and lithium intercalation in lithium-ion capacitors (Figure 26). It suggested that during the first reduction sodium cations were irreversibly intercalated and formed a pillared structure, similar to what was seen in a few other 2D materials (*138, 192-194*).

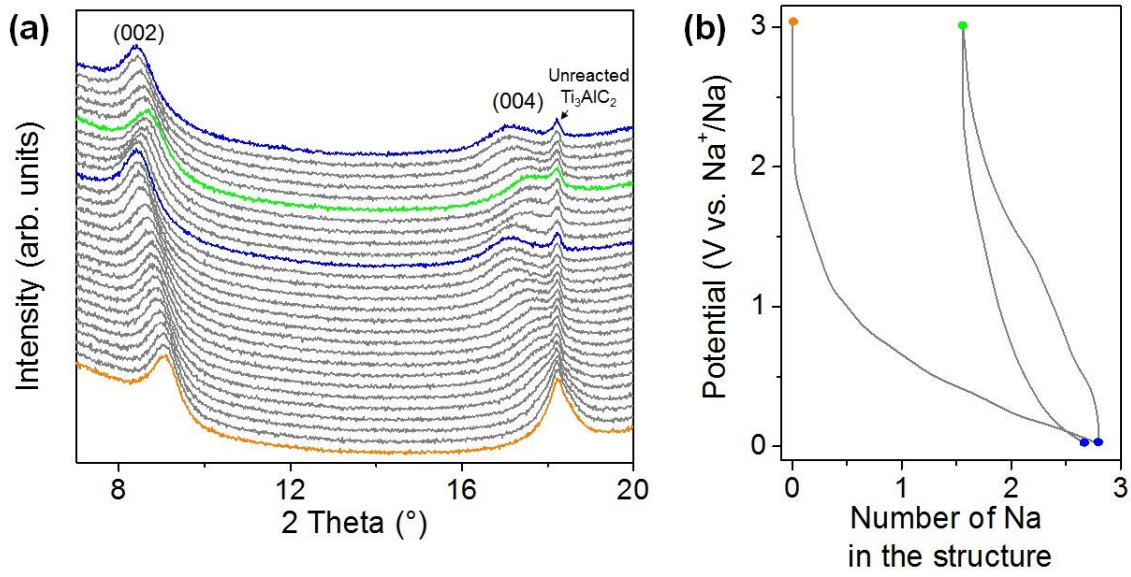

Figure 48: *In-situ* X-ray diffraction spectra (a) of $Ti_3C_2T_x$.during galvanostatic charge-discharge at 0.03 A/g and corresponding charge-discharge curves (b).

4.3.2 Modification of $Ti_3C_2T_x$

As the results presented in Figure 44 (capacitance improvement after chemical treatment in aqueous supercapacitors) suggested, a valid strategy to improve the performance was to tune the surface chemistry of the MXene. For this purpose, $Ti_3C_2T_x$ was modified using the same treatment, described in Chapter 3.2.1. In brief, $Ti_3C_2T_x$ was immersed and stirred for 6 hours in different electrolytes. Here, $Ti_3C_2T_x$ was immersed in 1M potassium hydroxide (KOH-$Ti_3C_2T_x$), 1M potassium acetate (KOAc-$Ti_3C_2T_x$), 1M lithium hydroxide (LiOH-$Ti_3C_2T_x$) and 1M sodium hydroxide (NaOH-$Ti_3C_2T_x$) replacing fluorine at the surface by oxygenated functional groups.

For comparison with the untreated $Ti_3C_2T_x$ in Figure 46.b, cyclic voltammetry tests were performed at 0.2 mV/s using modified-$Ti_3C_2T_x$ with 20 wt. % carbon black. The

results, shown Figure 49.a-d, demonstrated that the various treatments greatly influenced the electrochemical response upon cycling.

The first cycle irreversibility was reduced in all modified-$Ti_3C_2T_x$. It was be attributed to the contribution of two phenomena. First, the chemical treatments removed impurities such as aluminum fluoride and therefore prevented irreversible side reactions. Second, cations were spontaneously pre-intercalated from the aqueous electrolyte during the chemical treatments (seen Figure 36), resulting in an already pillared structure before cycling in the sodium-ion battery half-cell.

The shape of the cyclic voltammograms was modified with a clear displacement of the redox peaks. For example, the oxidation peak at 0.5 V vs Na^+/Na in the untreated $Ti_3C_2T_x$ (Figure 45.b) disappeared in the others cases. Broad peaks at 1.2 V and 1V were observed in KOH-$Ti_3C_2T_x$ and KOAc-$Ti_3C_2T_x$, respectively. NaOH-$Ti_3C_2T_x$ exhibited well defined sharp redox peaks at 2.3 V while LiOH-$Ti_3C_2T_x$ redox peaks were at 2.3 V and 1.6 V.

Whereas a 4-fold increase in capacitance was achieved by KOH treatment in the case of aqueous supercapacitors, herein the capacities achieved were not greatly improved, as seen Figure 52. To conclude, it was possible to modify the $Ti_3C_2T_x$ behavior by chemical treatments. It is conceivable that one could precisely tune a given MXene behavior by controlling the synthesis and post-treatment condition. This goal requires a separate extensive study.

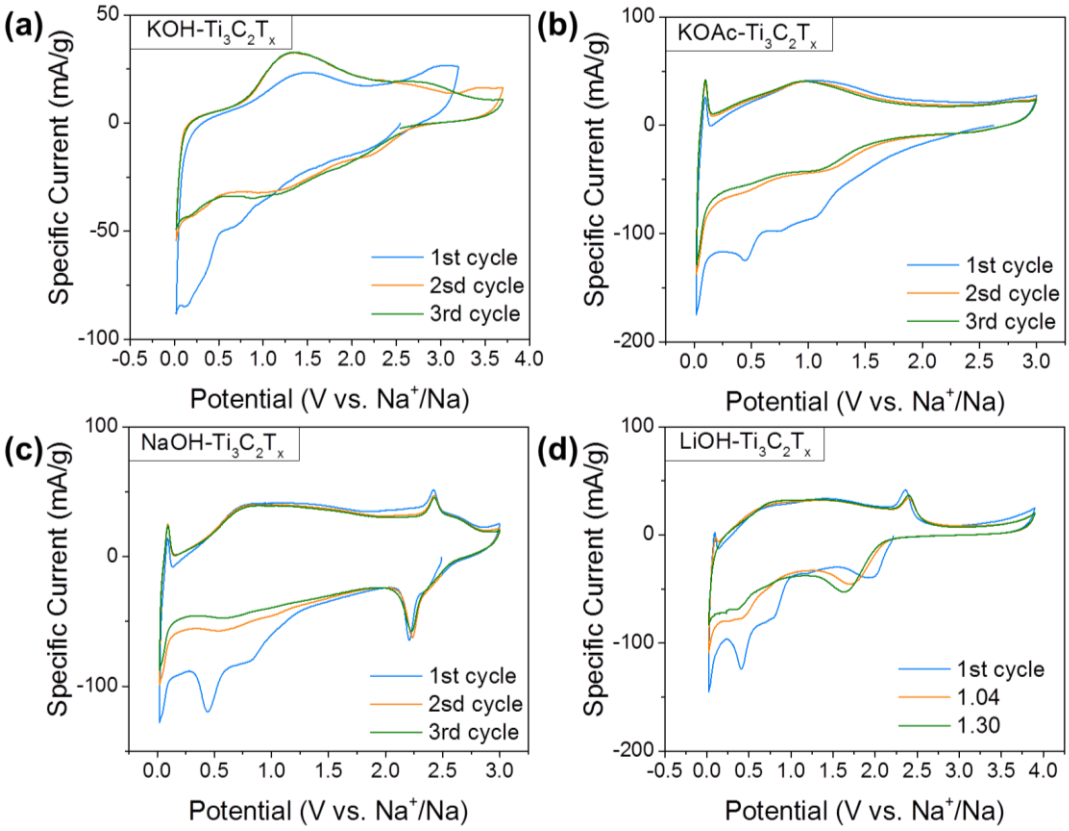

Figure 49: Cyclic voltammetry of $Ti_3C_2T_x$ treated in KOH (a) KOAc (b) NaOH (c) or LiOH (d) at 0.2 mV/s in 1 M $NaPF_6$ in EC:DMC.

4.3.2.1 Delaminated $Ti_3C_2T_x$

The delamination process discovered by Mashtalir *et al*. (*159*) already led twice to energy storage improvement (shown Figure 27 and Figure 44). The experimental procedure to prepare a binder-free flexible film electrode was detailed in Chapter 2.

The cyclic voltammograms obtained from this material are shown in Figure 50. The d-$Ti_3C_2T_x$ behavior was different from any $Ti_3C_2T_x$-based electrode previously tested. Unexpectedly, the performance was worse than untreated $Ti_3C_2T_x$. Several possible reasons exist, such as ion accessibility hindered by residual DMSO or fast deterioration

of the electrode in air, but none were investigated because a new synthesis method was discovered at Drexel University and explored instead. Recent research suggested that in-plane alignment of $Ti_3C_2T_x$ sheets limited the accessibility of electrolyte ions (*162*).

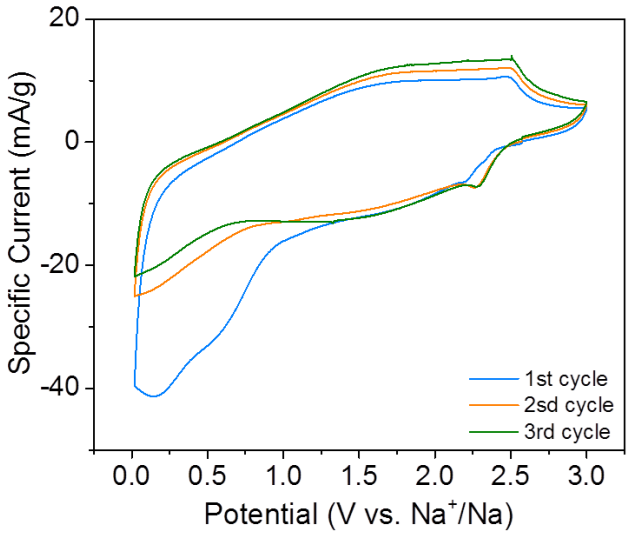

Figure 50: Cyclic voltammetry of d-$Ti_3C_2T_x$ at 0.2 mV s^{-1} in 1 M $NaPF_6$ in EC:DMC.

4.3.2.2 Clay $Ti_3C_2T_x$

All the MXene results described previously were obtained from the selective etching of Al from MAX phases using a concentrated solution of hydrofluoric acid (HF). Handling HF is dangerous and new procedures were investigated for safer and easier manufacturing. Early in 2014, a new synthesis procedure was proposed by Ghidiu *et al*. (*161*), by replacing the hydrofluoric acid etching agent with a mixture of hydrochloric acid (HCl) and fluoride salt (LiF, etc.). This mixture produced *in-situ* HF that could react as previously described. The main advantage of this procedure was that it was easier to handle and used safer and inexpensive chemicals. It consisted of mixing 2g of T_3AlC_2 in

100 mL of a 6M HCl/LiF solution at room temperature for 24 hours. With this mixture, the aluminum layer in Ti_3AlC_2 was still etched away but the $Ti_3C_2T_x$ produced behaved like clay that could be rolled by a glass tube to obtain a binder-free flexible freestanding film electrode (*161*).

Figure 51.a shows the scanning electron microscopy image of the cross-section. It showed that the film electrode was composed of multilayered $Ti_3C_2T_x$ and delaminated $Ti_3C_2T_x$ that created a network acting as binder and being responsible for the flexibility of the electrode. The electrochemical behavior of this material was investigated by cyclic voltammetry. In Figure 51.b the cyclic voltammogram shape can be described as rectangular with a well-defined redox couple at 2.4V vs. Na^+/Na. Notably, the first cycle irreversibility was the lowest observed so far. Although the capacity was lower than in other $Ti_3C_2T_x$ its behavior was still attractive for sodium-ion capacitors. Cyclic voltammetry at different rates has been performed to investigate the rate capability. The capacitance decreased quickly with increasing scan rate. At a moderate scan rate of 10 mV/s only 23 mAh/g remained which was too limited for real applications.

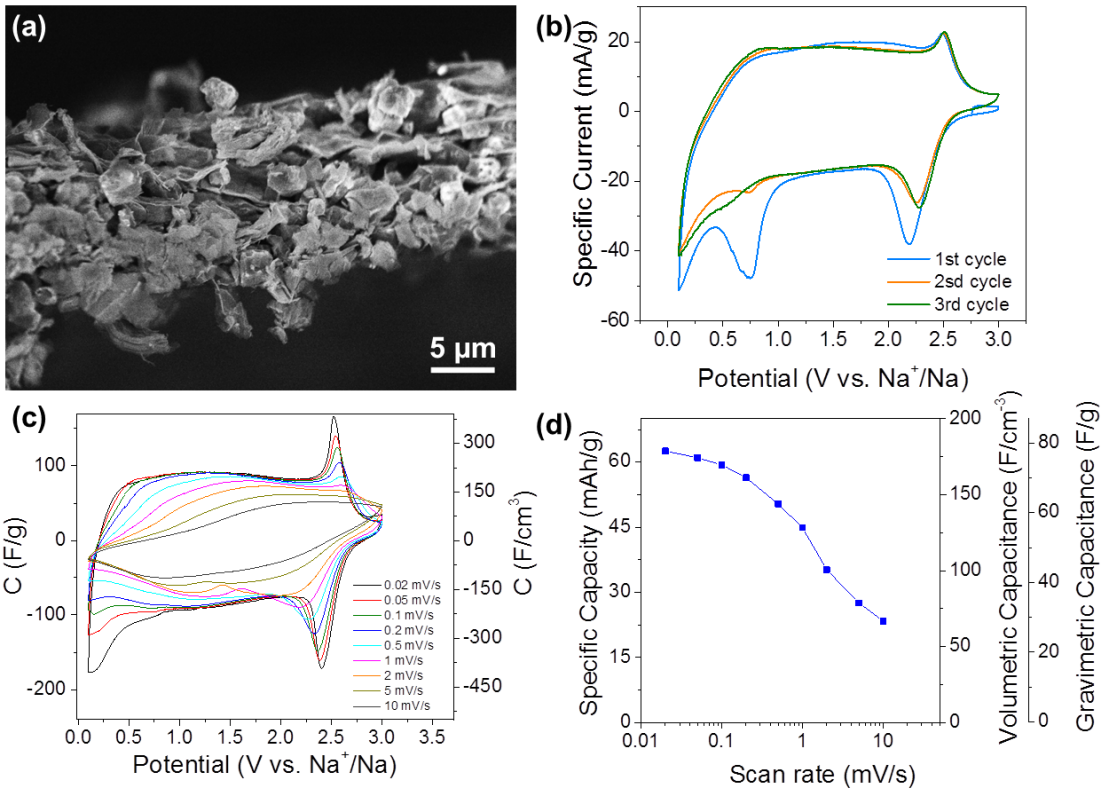

Figure 51: Scanning electron microscograph image of $Ti_3C_2T_x$ clay (a). Cyclic voltammetry of $Ti_3C_2T_x$ clay at 0.2 mV s^{-1} (b) and at different rates (c) in 1 M $NaPF_6$ in EC:DMC. Summary of rate performances (d).

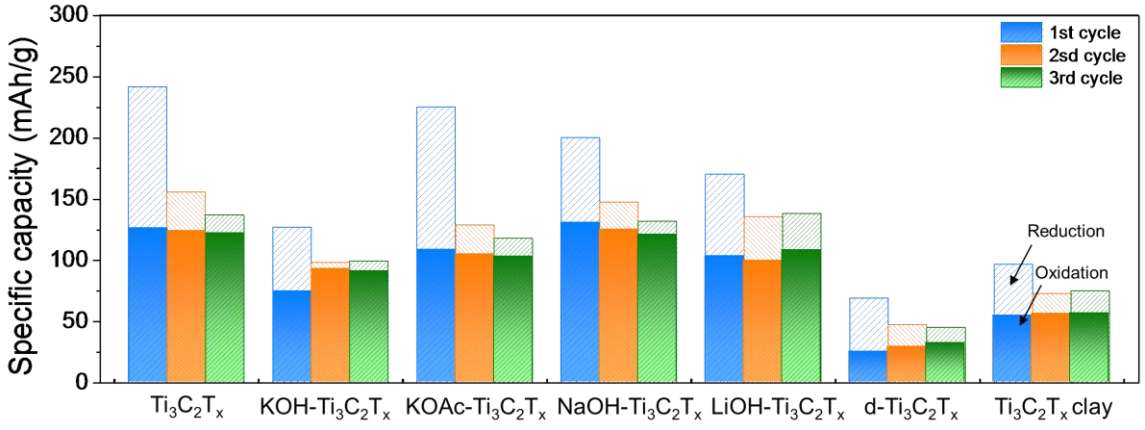

Figure 52: Capacity of all $Ti_3C_2T_x$-based electrodes calculated from cyclic voltammetry at 0.2 mV/s.

Early in 2015, the first experimental investigation of sodium-ion capacitors using MXenes was published by Wang *et al*. (*194*), who used Ti_2C as the negative electrode and alluaudite $Na_2Fe_2(SO_4)_3$ as the positive electrode. The cyclic voltammetry of this Ti_2CT_x was very different than the one observed in Figure 46, proving the influence of the synthesis conditions on the electrochemical performance. Interestingly it showed similarities to the clay $Ti_3C_2T_x$ (Figure 51), with redox peaks around 2.2 V vs. Na^+/Na. The mechanism was studied by *ex-situ* X-ray diffraction and showed sodium intercalation only during the first charge. Surprisingly, this was a different mechanism than that observed in Figure 48. Despite this, one could argue that *ex-situ* X-ray diffraction spectra could be irrelevant if extra care concerning reaction in air and electrode drying were not taken into account. The full cell showed a good rate capability and high specific power of 1.4 kW/kg with specific energy of 260 Wh per kg of Ti_2C.

Although promising results were shown with $Ti_3C_2T_x$, previous sodium-ion battery studies demonstrated that it was not the best MXene in terms of performance. It was decided to concentrate the effort on V_2CT_x.

4.4 V_2CT_x as a Positive Electrode

In contrast with Ti_2C and Ti_3C_2 which could only be used as negative electrodes because of their operating potential window, V_2CT_x showed a potential window ranging from 1 V to 3.5 V vs Na^+/Na. It is attractive as a positive electrode in Na sodium-ion capacitors. Here, the electrochemical behavior of two-dimensional vanadium carbide, V_2CT_x, was extensively investigated. V_2CT_x has been identified as the most promising member from the MXene family for use as a positive electrode. First, further test in half

cells were performed, then the energy storage mechanism was studied, and finally a full cell was assembled using a known negative electrode.

4.4.1 V_2CT_x vs Na

4.4.1.1 Electrode Preparation

V_2CTx electrodes were prepared with a 5 wt.% polytetrafluoroethylene binder (60 wt.% in H_2O, Sigma Aldrich) and 15 wt.% carbon black (Alfa Aesar) to secure a sufficient electronic conductivity. The electrodes were rolled and cut into ≈30 μm thick disks with an average mass loading of 5 $mg.cm^{-2}$. A two-electrode Swagelok® cell was used for half-cells with metallic sodium as counter and reference electrode separated by a glass fiber separator (Whatman® GF/A, Sigma Aldrich).

4.4.1.2 Cyclic Voltammetry

Figure 53.a shows the cyclic voltammetry results at different scan rates, while the change of the capacitance with the scan rate is described in Figure 53.b. High capacitances of 100 F/g or 170 F/cm^3 were obtained at slow scan rates and 50 F/g was still measured at 50 mV/s, evidence of good power performance of V_2CT_x for Na intercalation. At low scan rates, two different regions could be seen in the cyclic voltammograms, corresponding to two different electrochemical processes. From 1 V to 2.2 V, the rectangular shape of the voltammogram described a pseudocapacitive behavior. A similar storage mechanism has been previously demonstrated in others MXenes. For example Ti_3C_2 cycled in aqueous electrolyte exhibited a rectangular-shaped voltammogram attributed to redox reactions and intercalation (*172, 195*). Redox peaks were identified at low scan rates, with an oxidation peak at 3 V (peak A), and a reduction

peak at 2.5 V vs. Na^+/Na, (peak B). As the scan rate increased, the redox peaks tended to disappear, thus suggesting a diffusion limitation at scan rates beyond 2 mV/s. The large potential range and the absence of any 2-phase system plateaus make V_2C less suitable for sodium-ion battery electrodes, but such features are attractive for sodium-ion capacitors.

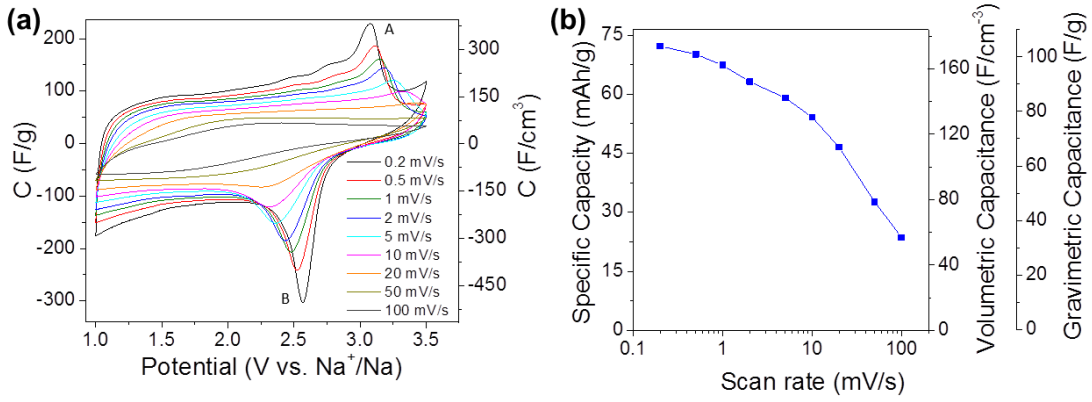

Figure 53: Cyclic voltammetry of V_2CT_x at different scan rates (a) and summary of rate performance (b) (adapted from (*196*)).

4.4.1.3 Galvanostatic Charge-Discharge Measurement

V_2CT_x was cycled at current densities from 30 mA/g to 1 A/g corresponding to the rate from C/3 (3 hours discharge) to 20C (3 min discharge), as shown in Figure 54. In this example, the positive electrode/negative electrode mass ratio was 1:2, to keep each electrode potential in their working potential window. At low charge/discharge rates, the faradaic efficiency decreased, thus leading to a capacity fade with cycling. At a low rate (C/3), the capacity fading was more pronounced in the first 40 cycles. Good capacity up to 70 mAh/g was obtained, with remarkable stability at discharge rates beyond 3C. The

performance achieved experimentally was lower than that predicted by first-principles simulations corresponding to the maximum theoretical capacity for a bare V_2C monolayer (335 mAh/g)(*184*). Experimentally, the capacity was limited by the presence of MAX phase residue, functionalized layers and stacked layers. Thus, there is much room for further increases in the capacitance of this material.

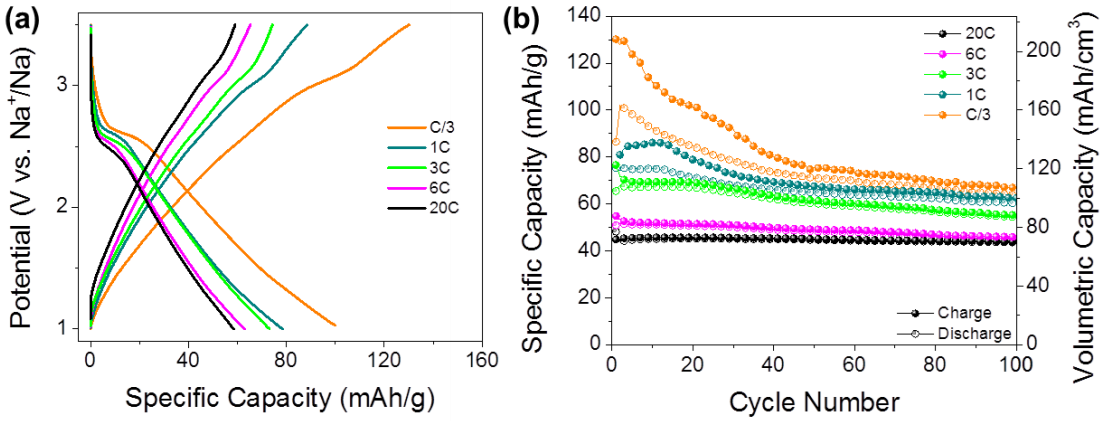

Figure 54: Charge-discharge profiles of V_2CT_x (a) and cycle life (b) from galvanostatic charge-discharge at different rates (adapted from (*196*)).

4.4.2 Mechanism

4.4.2.1 Electrochemical Impedance Spectroscopy

Characterization by electrochemical impedance spectroscopy was done at different potentials (Figure 55). The constant charge transfer resistance, as well as the improvement in the capacitive region at low frequencies, between 1 V to 2.5 V correlated well with a pseudo-capacitive intercalation mechanism. The charge transfer resistance (200 Ω/cm²) associated with the Na^+ pseudo-intercalation reaction explained the resistive

behavior observed in the cyclic voltammetry curves. The increase of the charge transfer resistance and the semi-infinite diffusion limitation visible in the low-frequency region at 3.2 V was associated with the full desodiation of V_2CTx, in agreement with the redox peaks observed in the voltammograms.

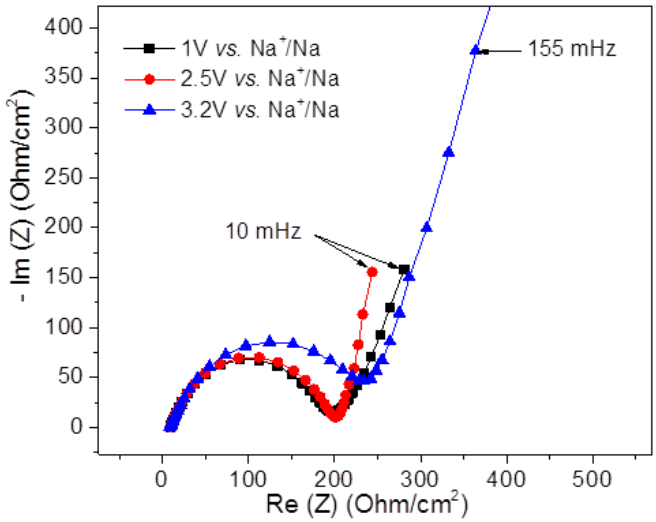

Figure 55: Nyquist plot from electrochemical impedance spectroscopy at different potentials (adapted from (*196*)).

4.4.2.2 X-ray Diffraction

Figure 56 shows *ex-situ* X-ray diffraction patterns of V_2CT_x recorded at different voltages, where it was observed that the (002) peak shifted continuously and reversibly from 9° to 12° during cycling between 1 and 3.5V vs Na^+/Na. In this potential range, the change was perfectly reversible, thus demonstrating that there were no undesired side reactions occuring. During sodiation, c-lattice parameter increased with the amount of Na^+ stored. This demonstrated that V_2CT_x stored energy through intercalation of Na ions

between layers in a similar way to that previously demonstrated for both intercalation of Li^+ into Ti_2C (*157*) or Ti_3C_2 (*175*) and Na^+ into Ti_3C_2 (*197*). There was no new phase appearing at 3.5 V vs. Na^+/Na, thus the redox process identified by peaks A and B in the voltammogram did not modify the crystallographic structure of the material. A 4.6 Å change in c-lattice parameter was observed, as calculated from Bragg's law. Taking into account that there were two interlayer gaps in a lattice unit, there is a 2.3 Å expansion or shrinkage during sodiation and desodiation, respectively. This was a larger change than expected for a single layer of Na^+ ions, which indicated that a second layer of Na^+ ions could be intercalated, as shown for Ti_3C_2 intercalated by Na^+ ions (*197*). The peak at 13° corresponded to V_2AlC from an incomplete synthesis reaction. This peak did not move during cycling, demonstrating that the MAX phase was not electrochemically active and that the capacity could be increased by increasing V_2CT_x yield. Nevertheless, the presence of this peak was useful as a reference for the other peaks.

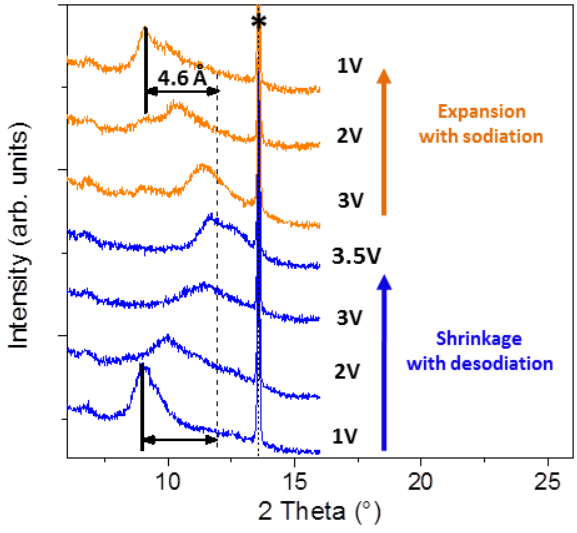

Figure 56: X-ray diffraction patterns at different potentials. (*) Peak of unreacted V_2AlC (adapted from (*196*)).

4.4.3 Full Cell

4.4.3.1 Negative Electrode Hard Carbon

The objective was to assemble a full cell using V_2CT_x as positive electrode and hard carbon (HC) as negative electrode for sodium intercalation (*42*). The hard carbon synthesized by pyrolysis of sugar under argon flow was selected because Ponrouch *et al*. demonstrated its low working potential (below 1V), good cycle life (>100 cycles), and high specific capacity (230 mAh/g at 1C rate).

Galvanostatic charge-discharge cycling of hard carbon electrodes was done at the same C-rate as V_2CT_x in perspective to assemble the full cell. In Figure 57 the expected key features of a carbon intercalation electrode were observed, with an intercalation potential below 1 V vs Na^+/Na and a capacity beyond 200 mAh/g at low rates.

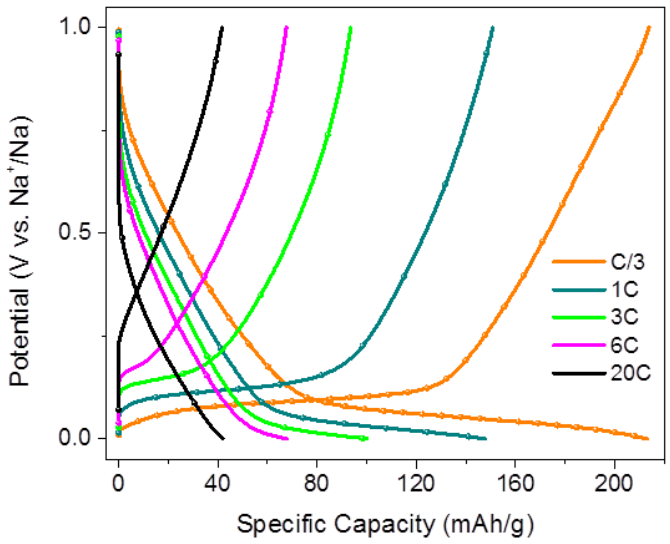

Figure 57: Charge-discharge profiles Hard Carbon electrode.

4.4.3.2 Full Cell Testing

Based on half-cell results, hybrid Na-ion capacitor full cells were assembled in three-electrode Swagelok© cells using an Ag wire as pseudo-reference electrode. The electrodes were pre-sodiated by immersing them in the electrolyte and short-circuited with metallic sodium. By anticipating the capacity decrease of V_2CT_x during the first cycles, a HC/V_2CT_x weight ratio of 1:2 was prepared.

In such conditions, the over-capacitive HC electrode allowed a better potential stability for the negative electrode. The full cells were tested from C/3 to 20C rate. Figure 58.b shows the electrochemical performance obtained in a full cell configuration. All the gravimetric capacities were calculated based on the total weight of both positive and negative electrodes in order to focus on the performances of the device. As the mass ratio of positive to negative electrode was 1:2, the equivalent capacities based on the mass of V_2CT_x were three times higher than those presented in Figure 58.

The charge/discharge galvanostatic profile is presented in Figure 58.a. During discharge, a sharp potential drop occured from 3.5 V down to 2.6 V, followed by a small plateau at 2.5 V due to the redox reaction peaks observed in Figure 53.a. Figure 58.b showed that high-power performance could be achieved with 40% of the total capacity obtained at 20C, despite the use of a Na-ion intercalation HC negative electrode. The capacity decrease during the first cycles at the low rate (C/3) was associated with a decrease of the coulombic efficiency due to redox reactions occuring beyond 3V.

Figure 58.c shows the cycle life of the full cell at a high rate (20C). After 300 cycles, the capacity retention was 70%. Interestingly, the capacity slightly increased during the first 70 cycles. Afterward, the capacity decrease was associated with the decrease of the

faradaic efficiency down to 98%. In order to better understand this decrease, both electrodes were studied using a 3-electrode cell. Figure 58.d shows the 2^{sd} and 200^{th} cycles. First, it can be noticed that the negative electrode potential range was smaller than 1 V because HC was in excess. As explained previously, a slightly overcapacitive negative electrode is necessary to ensure good stability. Although the positive electrode had low irreversibility, it was sufficient to drive a shift of the negative electrode toward higher potentials after a large number of cycles. The potential of the V_2CT_x electrode went slightly beyond the optimum operating potential range of 1 V to 3.5 V, which leads to irreversible redox reactions, thus explaining the capacity decrease upon cycling. An optimization of the electrode mass ratio should prevent the observed drift of the positive electrode potential, leading to an improvement in cyclability.

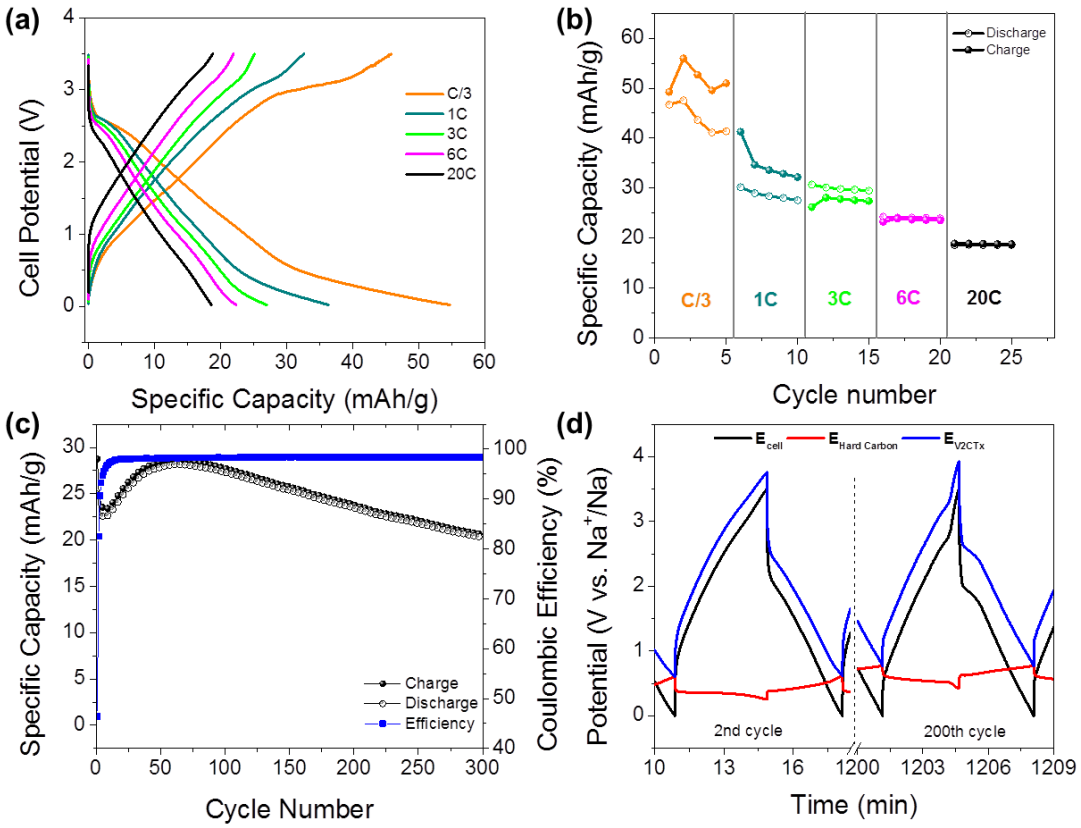

Figure 58: Charge-discharge profiles at various rates (a). Change of the capacity during galvanostatic charge-discharge at different rates (b). Capacity vs cycle number (c). Details of the potential range of positive and negative electrodes at 1A/g (d). Capacities were calculated for the total mass of both positive and negative active material, taken with the mass ratio as 1:2 (adapted from (*196*)).

4.5 Conclusions

This work showed that at least one representative of the large family of MXenes, V_2CT_x, can serve as the positive electrode for a sodium-ion supercapacitor. Investigation of the mechanism of sodiation and desodiation of V_2CT_x by X-ray diffraction showed continuous intercalation of sodium ions between the V_2CT_x layers over a wide range of potentials. Electrochemical testing in half-cells demonstrated that both capacitive

(pseudocapacitive) and diffusion-limited redox processes took place. An asymmetric full cell was assembled using hard carbon, a known anode material for sodium-ion batteries. V_2CT_x/HC sodium-ion capacitor showed promising results, with a capacity of 50 mAh/g.

It is important to note that all results shown here were obtained on samples containing residual MAX phase, therefore decreasing the overall performances. The capacitance could be improved by tuning the surface chemistry by post-synthesis treatment or by the new synthesis route of MXene, via a fluoride salt and HCl etching, proposed for $Ti_3C_2T_x$. It may offer material of higher purity, which would also show improved performance in Na-ion capacitors. Finally, with just two MXenes studied in Na-ion capacitors to date and already showing promise for use as both negative and positive electrodes, there is clear opportunity to create devices with both electrodes made of 2D carbides, but further studies of electrochemical behavior of those new materials are needed.

CHAPTER 5: MXene as a Supercapacitors Electrode in Organic Electrolytes

5.1 Introduction

MXene-based Ti_3C_2 electrodes have shown excellent capacitance in aqueous electrolytes in Chapter 3, but over a narrow potential window which limits both the energy and power density. It was shown that the morphology and surface chemistry have a great impact on the electrochemical performance. New electrode formulation and synthesis routes have been explored by other researchers to continuously improve the performance of MXene electrodes in aqueous supercapacitors.

The interest in composites has been demonstrated previously with the example of graphene composites. As MXene has comparable properties to graphene, the elaboration of MXene composites is a promising method to obtain new material properties. Zhao *et al.* proposed the fabrication of various carbon material/Ti_3C_2 composites (*162*). Tests with several carbon compounds (carbon nanotube, graphene or onion-like carbon) and different fabrication process (layer by layer sandwiched structure or mixed) were performed. 1M $MgSO_4$ electrolyte was used to compare the different composites. Capacitances up to 390 F/cm^3 were obtained for sandwich-like Ti_3C_2/single-walled carbon nanotubes As carbon nanotubes do not contribute significantly to the capacitance, the improvement was attributed to the conductivity increase, to the increase of spacing between layers and to the well-organized layered structure that increase the diffusion rate. Liu *et al*. prepared a carbon nanotubes/Ti_3C_2 composite for lithium-ion batteries (*198*).The composite exhibited higher capacity (428 mAh/g) than individual Ti_3C_2 (96 mAh/g) and better rate capability.

MXene synthesized with the new method proposed by Ghidiu *et al*. (*161*) behaved differently than MXene synthesized by the concentrated HF method. The wet product behaved like clay and could be rolled. In a single step (rolling) a conductive, flexible, and free-standing film can be prepared. In comparison, preparing the free-standing delaminated film previously described is laborious. Clay-like MXenes did not show the graphite like (accordion-like) morphology. This was attributed to shearing of layers containing water acting as a lubricant. The authors investigated the electrochemical behavior for aqueous supercapacitor using H_2SO_4. Authors obtained excellent capacitance values up to 900 F/cm^3 and 245 F/g at 2 mV/s.

MXene has been investigated several times as an electrode material for supercapacitors in aqueous electrolytes, but all the results reported showed a limited potential window due to water electrolysis. Moreover, oxidation of Ti_3C_2 under high anodic potentials in aqueous electrolytes further limits its use to the cathodes of asymmetric devices. As both the energy and the power density increase with the square of the potential window, the expansion of the voltage window is one of the key challenges for designing supercapacitors with improved performance and organic electrolytes may expand the voltage window beyond 2-2.5 V.

Here, the electrochemical behavior of Ti_3C_2 MXene was investigated in 1M solution of 1-ethly-3-methylimidazolium bis-(trifluoromethylsulfonyl)-imide (EMITFSI) in acetonitrile and two other common organic electrolytes. Both the addition of carbon nanotubes and the new synthesis procedure showed an increase in performance. The following describes the use of clay, delaminated, and composite Ti_3C_2 electrodes with

carbon nanotubes in order to understand the effect of the electrode architecture and composition on the electrochemical performance.

5.2 Electrode Preparation

$Ti_3C_2T_x$ was synthesized by selectively etching the aluminum layer out of the Ti_3AlC_2 MAX phase in a 6M HCl/LiF solution at 35°C for 24h (*161*). The material obtained was then washed with distilled water. Full delamination of $Ti_3C_2T_x$ was obtained by ultrasonication for 1h in distilled water. A composite material was prepared by mixing the colloidal solution of delaminated Ti_3C_2 with 20 wt. % of multiwalled carbon nanotubes (MWCNT C100, Graphistrength) which had specific surface area of 175 m²/g. The as-synthesized $Ti_3C_2T_x$, the delaminated $Ti_3C_2T_x$, and the CNT/$Ti_3C_2T_x$ composite were filtered on polypropylene membranes then rolled into film electrodes on Teflon® membranes using a glass tube. Once dried, the films were easily removed from the membrane to obtain the freestanding flexible $Ti_3C_2T_x$, d-$Ti_3C_2T_x$ and CNT-$Ti_3C_2T_x$ films without binder. The electrodes were prepared by cutting the films into ~25 mm² rectangles with a razor blade, with mass loadings of 1.5 mg/cm, 1.8 mg/cm and 2.8 mg/cm respectively, for $Ti_3C_2T_x$, d-$Ti_3C_2T_x$ and CNT-$Ti_3C_2T_x$ electrodes. The thicknesses were determined from scanning electron microscope observations and $Ti_3C_2T_x$, d-$Ti_3C_2T_x$ and CNT-$Ti_3C_2T_x$ film densities were calculated to be 2.3 g/cm^3, 3.0 g/cm^3 and 2.9 g/cm^3, respectively.

5.3 Materials Characterization

A scanning electron microscope JSM-6700F (JEOL, Japan) was used to investigate the morphology of the samples. Figure 59 shows cross-section scanning electron

microscopy images of electrode materials. The as-prepared MXene clay, denoted as $Ti_3C_2T_x$, is shown in Figure 59.a-b. MXene layers could be rolled and sheared, forming a freestanding flexible electrode (*161, 178*). Fully delaminated MXene electrodes, denoted as d-$Ti_3C_2T_x$ (Figure 59.c-d), were prepared for improving the electrochemical performance by taking advantage of a higher specific surface area resulting from delamination. The specific surface areas values were 23 m^2/g for multilayered Ti_3C_2 and 98 m^2/g for delaminated Ti_3C_2 measured elsewhere by nitrogen gas sorption analysis (*159*) while 128 m^2/g was estimated for CNT-$Ti_3C_2T_x$.

However, previous studies demonstrated that restacking of delaminated MXene layers forming a dense MXene "paper" with in-plane alignment of MXene sheets limited the accessibility of electrolyte ions. Such restacking issue could be prevented by the addition of carbon nanoparticles (*162, 198*). Accordingly, composite electrodes were prepared by mixing appropriate amounts of d-$Ti_3C_2T_x$ and MWCNTs. The specific surface area obtained by nitrogen gas sorption analysis was 70 m^2/g for the CNT-$Ti_3C_2T_X$. Figure 59.e-f shows scanning electron microscopy images of a cross-section of the CNT-$Ti_3C_2T_x$ composite electrode, where CNTs were homogeneously spread between the Ti_3C_2 layers since no aggregates could be seen. Aside from preventing restacking, CNT addition is known to increase the conductivity of the electrodes (*162, 198-201*).

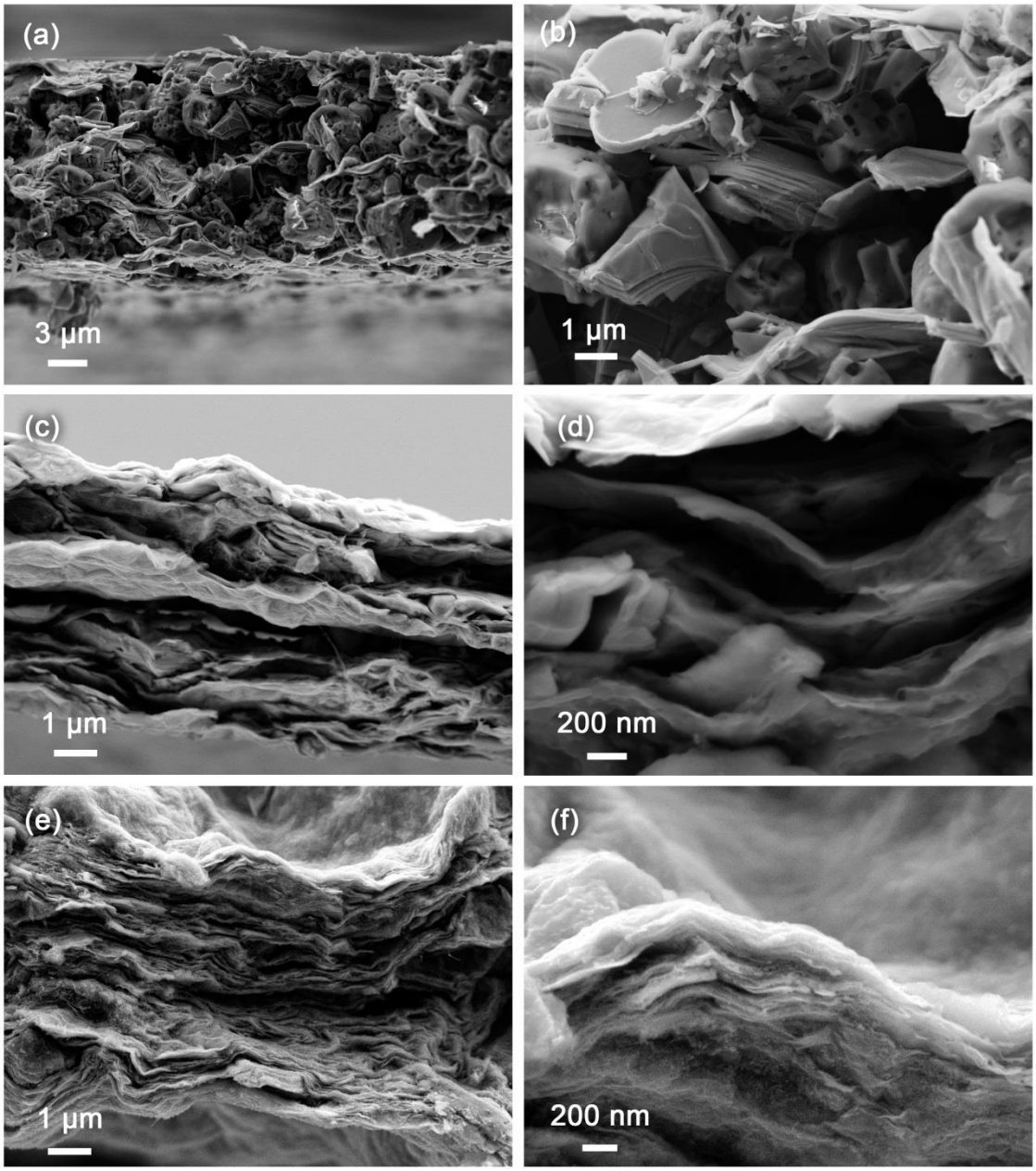

Figure 59: Scanning electron microscope images of rolled $Ti_3C_2T_x$ "clay" (a-b), d-$Ti_3C_2T_x$ (c-d) and CNT-$Ti_3C_2T_x$ (e-f) electrode films (adapted from (*202*)).

5.4 Electrochemical Behavior

Most pseudocapacitive materials, such as RuO_2, have high capacitance values in aqueous electrolytes (720 F/g for RuO_2 (*87*)) but very low in organic electrolytes. The reason for this important difference could be found in redox mechanisms in aqueous electrolytes that do not work in organic solutions. However $Ti_3C_2T_x$ is promising because it can store the charge through intercalation capacitance even in organic electrolytes as was demonstrated previously by Come *et al*. (*157*) and in Chapter 4. In this part the study focused on the electrochemical behavior in a common organic electrolyte; 1M EMITFSI (Solvionic) dissolved in acetonitrile (Acros Organics). Three-electrode Swagelok® cells were used with Ti_3C_2 as working electrode, an Ag wire as a pseudo-reference electrode and a commercial activated carbon (YP17 Kuraray, Japan) overcapacitive counter electrode prepared by mixing 5 wt.% polytetrafluoroethylene binder (60 wt.% in H_2O, Aldrich) to 95 wt.% of YP17. A polypropylene membrane (GH Polypro, Pall) was used as a separator.

5.4.1 Characterization of Carbon Nanotubes

Since a composite electrode was prepared with carbon nanotubes, it was important to determine the capacitance contribution of this additive. In the first chapter, it was reported that carbon nanotubes capacitances were estimated at 60 F/g in the literature. However the performance depended on various parameters and it was necessary to test the exact carbon nanotube that was selected.

Figure 60 shows the cyclic voltammetry results at different scan rates of the multiwalled carbon nanotube C100 from Graphistrength® tested as powder in a three-electrode Swagelok® cell with a Ag wire reference and overcapacitive activated carbon

counter electrode. Gravimetric capacitance of up to 36 F/g was obtained. This value was lower than that reported for some other carbon nanotubes, but the cyclic voltammograms exhibited a rectangular shaped response characteristic to double layer capacitance. A good rate capability highlighted the good conductivity of this material. The capacitance contribution of 20 wt. % of carbon nanotubes in the composite can be assumed to not exceed 7.2 F/g and will be taken into account.

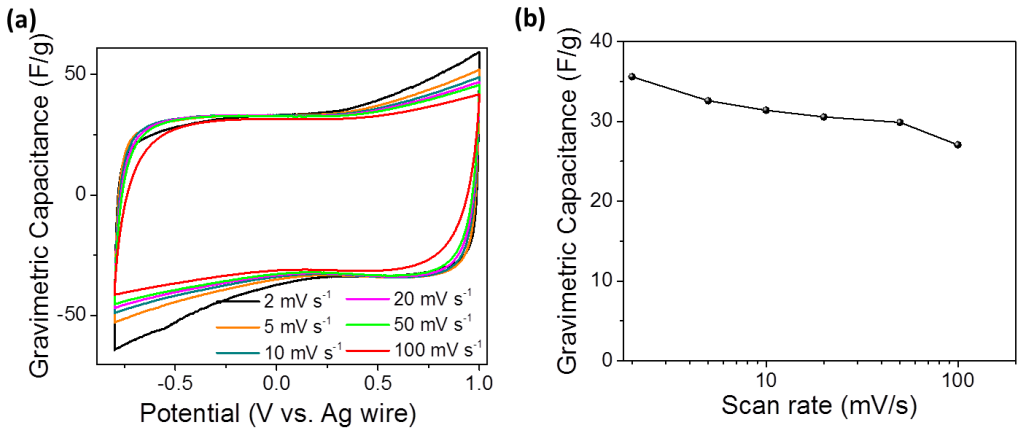

Figure 60: Electrochemical performance of multiwalled carbon nanotubes in 1M EMITFSI in acetonitrile; cyclic voltammograms at different scan rates (a) and summary of capacitance with the potential scan rate (b).

5.4.2 Cyclic Voltammetry

Figure 61 shows cyclic voltammograms of the three Ti_3C_2-based electrodes at 20 mV/s in 1M EMITFSI in acetonitrile. The electrochemical signatures of the three samples appeared to be similar, characterized by a capacitive envelope and a set of redox peaks around -0.2 V and -0.4 V *vs.* Ag. The potential difference between the oxidation and reduction peaks, associated with kinetics and ohmic limitations, changed from one

electrode to another. The smallest difference was observed for CNT-$Ti_3C_2T_x$, which could be associated with a first approach to a faster diffusion path, thanks to the addition of CNTs. $Ti_3C_2T_x$ showed a similar electrochemical signature with a slightly larger overpotential. d-$Ti_3C_2T_x$ showed the largest overpotential and most resistive behavior, possibly due to the restacking of delaminated layers during electrode preparation. The potential range (1.8V) was narrower than expected from this electrolyte but could be explained by water trapped between Ti_3C_2 layers, responsible for electrolyte reaction at the extrema of the potential range visible at low scan rates.

The change of the capacitance (calculated from the integration of the charge during cyclic voltammograms measurements) with the potential scan rate is shown Figure 61.d. Capacitance up to 245 F/cm^3 (85 F/g) was obtained at 2 mV/s for CNT-Ti_3C_2, with 75% capacitance retention at 100 mV/s (50% for d-$Ti_3C_2T_x$). This performance highlighted a fairly high power capability of the electrodes, which was assumed to originate from the open 2D structure of the material and the associated high accessibility of the surface to ions. The lower rate performance of d-$Ti_3C_2T_x$ could be attributed to poor charge percolation.

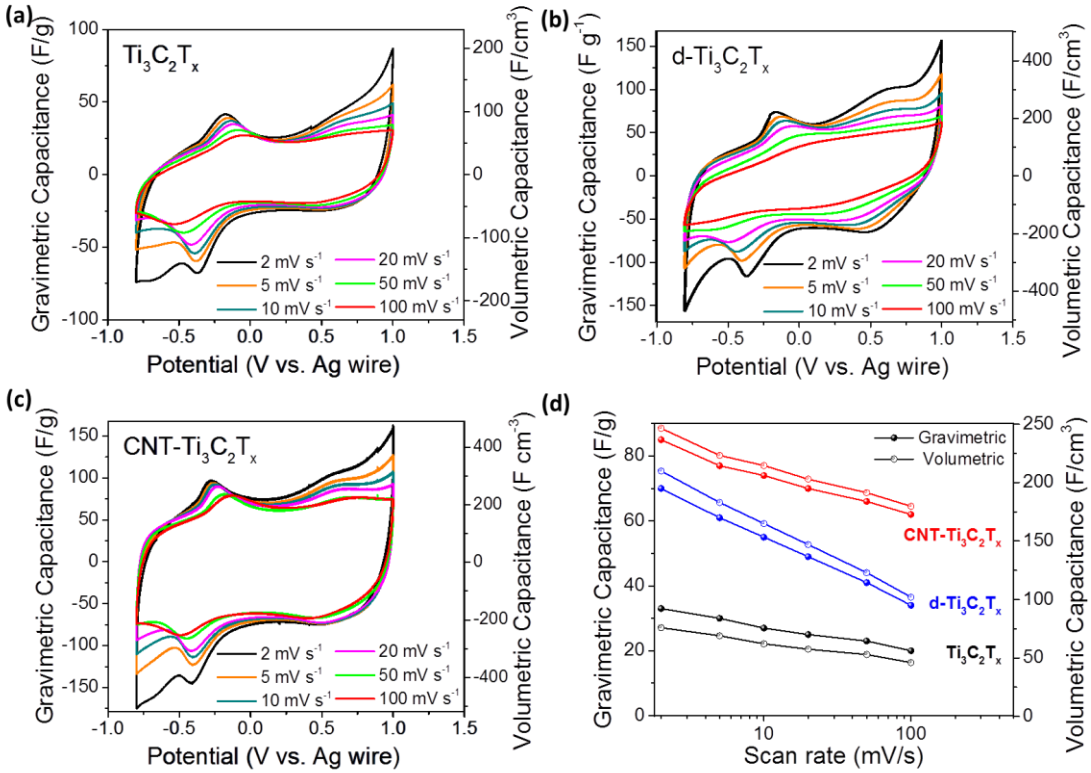

Figure 61: Cyclic voltammograms of $Ti_3C_2T_x$ (a), d-$Ti_3C_2T_x$ (b) and CNT-$Ti_3C_2T_x$ (c) in 1M EMITFSI in acetonitrile electrolyte at different scan rates and summary of the change of capacitance with the potential scan rate (d). These measurements were done using a three-electrode Swagelok® cell (adapted from (*202*)).

5.4.3 Electrochemical Impedance Spectroscopy

The electrochemical impedance spectroscopy measurements (Figure 62) of the three different samples were performed between 200 kHz and 100 mHz in a two-electrode configuration after polarization at 0.5 V *vs.* Ag (open circuit voltage) using a three-electrode setup. The smaller semi-circle suggested that the addition of MWCNT greatly improves the charge percolation of the electrode. Additionally, there was little to no influence of MWCNTs on the electronic conductivity of the electrode, as can be seen from the constant value of the high-frequency resistance. This can be explained by a

much higher conductivity of metallic $Ti_3C_2T_x$ electrode films (~ 2000 S/cm (*203*)) compared to conventional activated carbon, oxide or even graphene electrodes.

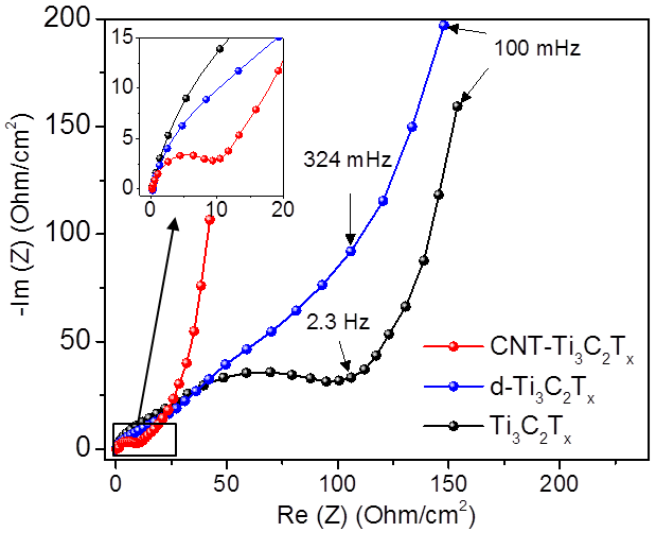

Figure 62: Nyquist plot at 0.5 V *vs.* Ag reference obtained using a two-electrode setup (adapted from (*202*)).

5.4.4 Galvanostatic Charge-Discharge Measurements

Figure 63.a-c shows the galvanostatic charge-discharge curves obtained at 1A/g for the three electrodes. Gravimetric capacitances were calculated from the total mass of the composite electrode; associated volumetric capacitances were obtained using the density of the respective electrodes. The curves were almost linear but contained a slight change in their slopes which corresponded to the redox peaks identified previously. It appeared that the electrodes exhibited pseudo-capacitive behavior. Also, a 5-10 times lower specific surface area of MXene (*172*) compared to activated carbons (*4*) would lead to a very low capacitance without the contribution of charge-transfer processes. Figure 63.d

shows the cycle life for the different electrodes at 1A/g. CNT-$Ti_3C_2T_x$ showed a good stability, with 90% capacitance retention after 1,000 cycles. $Ti_3C_2T_x$ and d-$Ti_3C_2T_x$ showed a lower stability and faster capacitance decrease during cycling, as well as a lower coulombic efficiency.

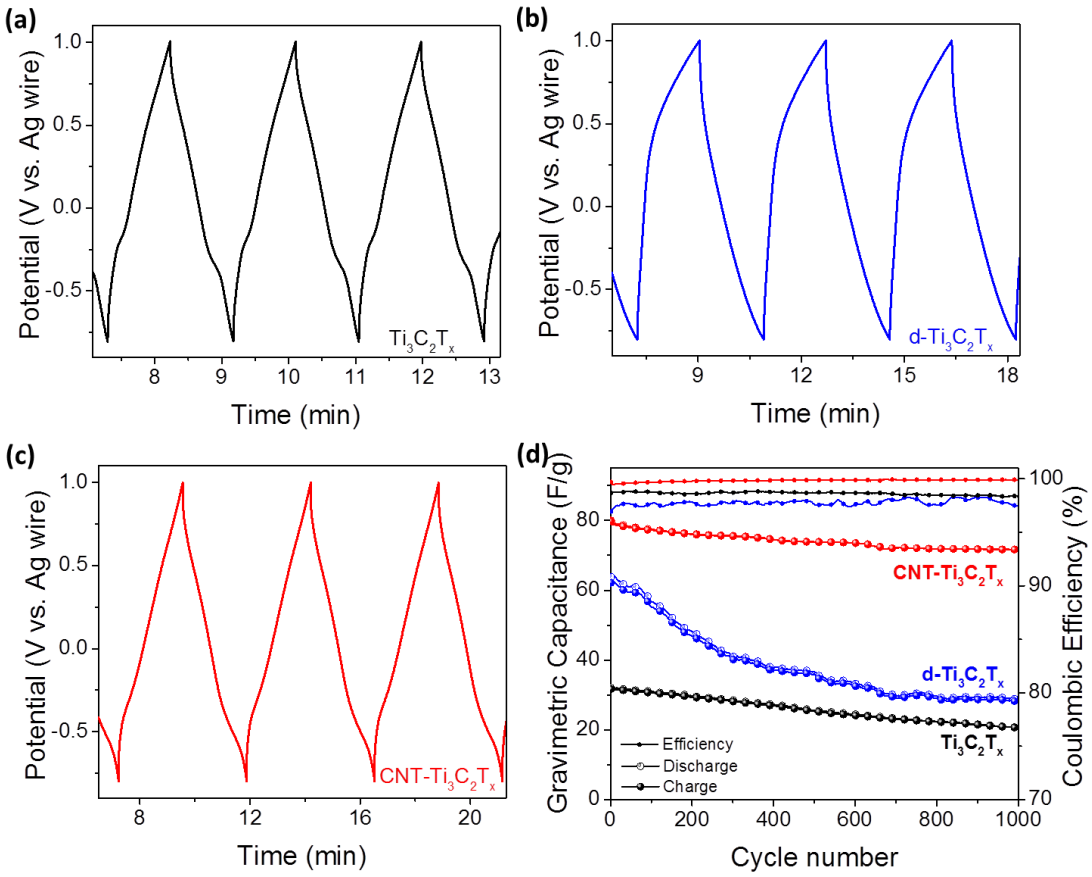

Figure 63: Galvanostatic charge-discharge curves of $Ti_3C_2T_x$ (a), d-$Ti_3C_2T_x$ (b) and CNT-$Ti_3C_2T_x$ (c) in 1M EMITFSI in acetonitrile electrolyte obtained at 1 A/g and the corresponding cycle life of those electrodes (d). These measurements were done using a three-electrode Swagelok® cell (adapted from (*202*)).

5.5 Charge Storage Mechanism

5.5.1 *In-situ* X-ray Diffraction

The energy storage mechanism was investigated by recording *in-situ* X-ray diffraction patterns at different potentials (Figure 64). Each set of Bragg peaks could be indexed using the (00n) diffraction planes of Ti_3C_2 which are characteristic of the interlayer spacing. Interestingly at the open current voltage before cycling (open circuit voltage was 0.5 V vs. Ag) a (00n) downshift was observed, demonstrating a spontaneous intercalation similar to that previously observed in aqueous electrolytes.

The comparison of patterns indicated that depending on the applied potential, two different sets of Bragg peaks were observed and that the phase change occurred at the same potential where the set of redox peaks appeared in the cyclic voltammetry (Figure 61.c). This showed that the intercalation / deintercalation processes followed a reversible two-phase mechanism. On the basis of the diffraction angle of (002) Bragg peaks (Figure 64.b), it was deduced that over the -0.8 V to -0.5 V potential range, the interlayer distance was 1.3 Å larger than at potentials above -0.5 V and should correspond to the intercalation and de-intercalation of ions from the electrolyte into $Ti_3C_2T_x$.

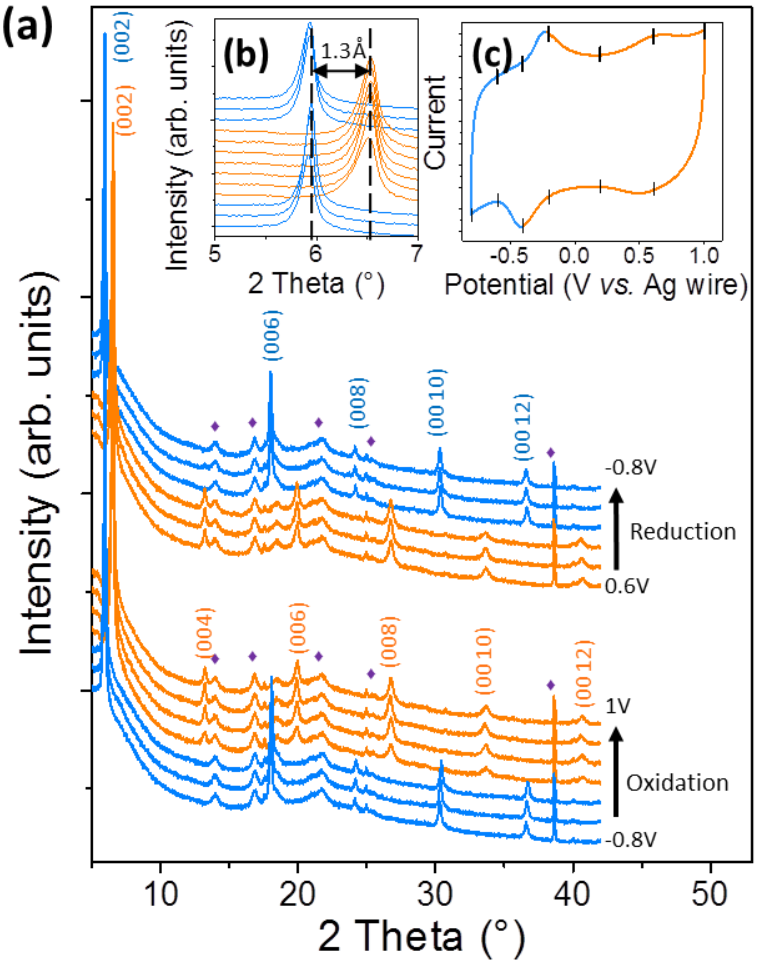

Figure 64: *In-situ* X-ray diffraction patterns of CNT-$Ti_3C_2T_x$ at different potentials in the 5-50° 2θ range (a). Purple diamonds indicate peaks coming from the cell for *in-situ* measurements. Inset (b) shows a zoom in the 5-7° 2θ range and cycle voltammograms recorded at 20 mV/s (c) (adapted from (*202*)).

This charge storage mechanism was not expected for $Ti_3C_2T_x$ because it differed from the progressive and continuous intercalation process previously observed for MXenes materials in aqueous supercapacitors (Chapter 3) and metal-ion capacitors (Figure 26 and Chapter 4). Another method to reveal this fast and reversible two-phase transformation was to record the X-ray diffraction spectra during the electrochemical cycling over the

total potential range instead of at a fixed potential. For this purpose the *in-situ* cell was cycled at fast scan rate (50 mV/s) while the X-ray diffraction spectra was recorded slowly, as shown Figure 65. The two sets of peak were identifiable clearly demonstrating that this two-phase transformation was not limited by diffusion or kinetics.

Taking into account that the cation EMI^+ spontaneously intercalated between $Ti_3C_2T_x$ layers, a reasonable hypothesis for the intercalation/deintercalation mechanism observed was the formation of a second EMI^+ layer. This hypothesis, represented in the inset of Figure 65., was supported by a recent *in-situ* aberration-corrected scanning transmission electron microscope experiment that demonstrated the formation of 2 layers of Na^+ between $Ti_3C_2T_x$ layers (*197*).

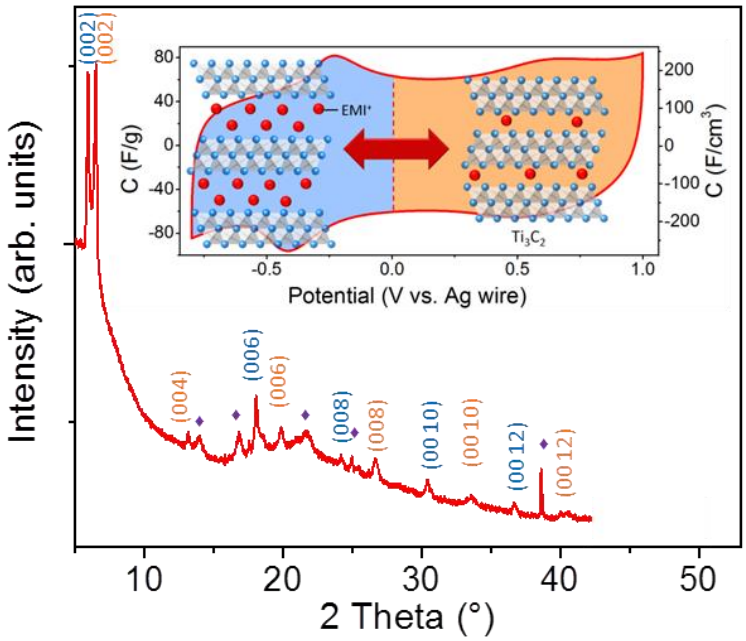

Figure 65: *In-situ* X-ray diffraction patterns of CNT-$Ti_3C_2T_x$ during cycling at 50 mV/s. Purple diamonds indicate peaks corresponding to the *in-situ* cell. Inset: Schematic of the two-phase transformation.

5.5.2 Cyclic Voltammetry

Considering the low value of the intercalation potential, one can assume in a first approximation that the expansion was due to the intercalation of the EMI^+ cations between Ti_3C_2 layers and the shrinkage was attributed to its de-intercalation. Reversible intercalation of organic ions, accompanied by peaks in the cyclic voltammograms, was observed for porous carbon electrodes when the ion size was somewhat larger than the pore size (*204*). Interestingly when cycled within the 0.1 V to 1 V potential range, $Ti_3C_2T_x$ capacitance quickly decreased with the cycle number, while it was more stable when cycled between -0.8 V and 0.1 V, as shown Figure 66. This suggested that the capacitive behavior observed above 0 V was associated with a redox process at negative potentials. In other 2D materials, it was observed that the intercalation of ions could form a pillared structure (*138, 192-194*). It is possible that cycling exclusively in the positive region caused the structure to collapse.

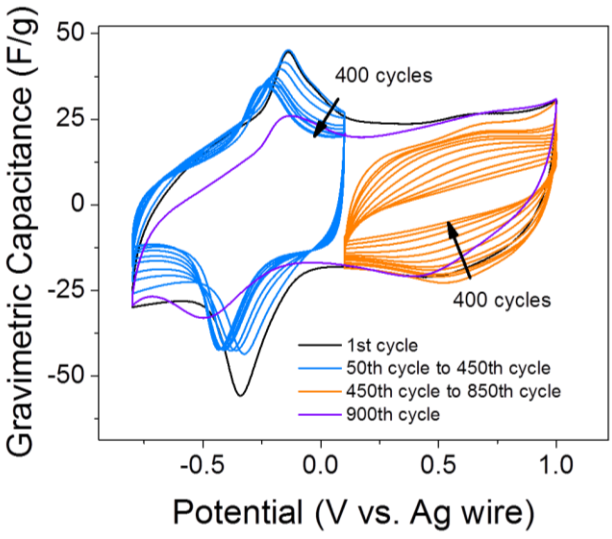

Figure 66: Cyclic voltammograms of $Ti_3C_2T_x$ in different potential ranges at 20 mV/s (adapted from (*202*)).

5.6 Other Organic Electrolytes

The electrochemical performance of $Ti_3C_2T_x$ electrodes in aqueous electrolytes greatly depended on the electrolytes used. This was demonstrated in Chapter 3 by performing extensive electrochemical tests on a wide variety of electrolytes. Herein, the behavior of CNT-$Ti_3C_2T_x$ in two other commonly used organic electrolytes, 1M $EMIBF_4$ (1-ethyl-3-methylimidazolium tetrafluoroborate, Fluka) and 1M $TEABF_4$ (tetraethylammonium tetrafluoroborate, Acros Organics), was tested by cyclic voltammetry at 20 mV/s.

Figure 67.a shows the cyclic voltammogram of the CNT-$Ti_3C_2T_x$ electrode in 1 M $EMIBF_4$ in acetonitrile electrolyte (a smaller anion but the same cation as in Figure 61). The electrochemical signature was similar to that obtained in 1M EMITFSI in acetonitrile electrolyte (Figure 61); more specifically, the presence of a set of redox peaks at the same potential. Figure 67.b shows the cyclic voltammogram of the CNT-$Ti_3C_2T_x$ electrode in 1 M $TEABF_4$ in acetonitrile electrolyte. When replacing the "planar" EMI^+ cation with the larger and more "spherical" TEA^+ cation, the electrochemical response was changed drastically. The reduction (intercalation) peak was present at a lower potential (-1 V vs Ag wire), but the reaction seemed irreversible with an oxidation wave shifted to about 0.5 V. It was probable that the large TEA^+ ions were stuck between MXene sheets after intercalation, decreasing the reversibility of the process, but also contributing to pillaring. The comparison of the cyclic voltammograms of CNT-$Ti_3C_2T_x$ in 1M solutions of EMITFSI, $EMIBF_4$ and $TEABF_4$ in acetonitrile provided further evidence that the redox reaction was due to the intercalation of cations. These measurements suggested that the intercalation/deintercalation of the EMI^+ cation was responsible for the reversible redox

process occurring at -0.4 V *vs.* Ag. This hypothesis should be further confirmed by other *in-situ* characterization techniques, such as electrochemical quartz crystal microbalance (*205*) or nuclear magnetic resonance (*206*).

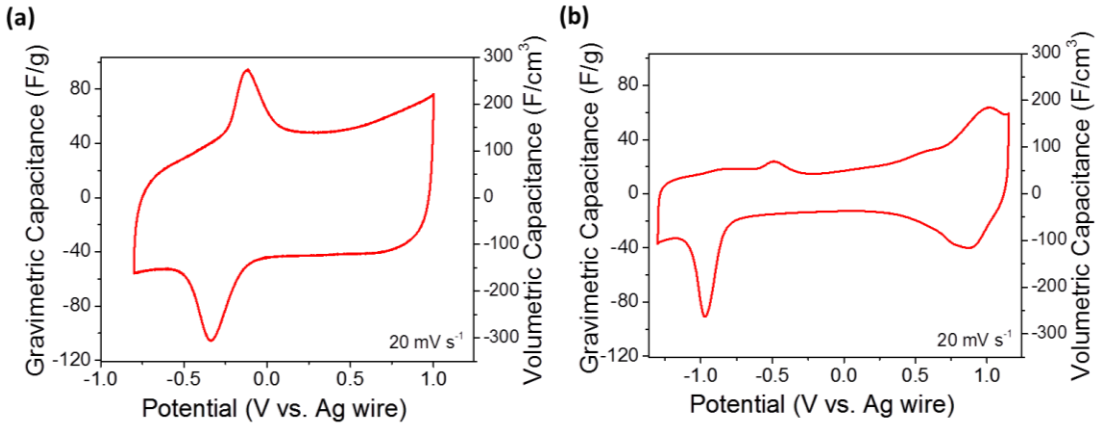

Figure 67: Cyclic voltammetry of CNT-$Ti_3C_2T_x$ at 20 mV/s in 1 M solutions of $EMIBF_4$ (a) and $TEABF_4$ (b) in acetonitrile (adapted from (*202*)).

5.7 Conclusions

The electrochemical behavior of $Ti_3C_2T_x$ as an electrochemical capacitor electrode in organic electrolytes has been investigated. Capacitances up to 32 F g^{-1} were obtained for as-produced $Ti_3C_2T_x$-MXene clays and improved up to 85 F g^{-1} by delamination and addition of carbon nanotubes. Intercalation of large EMI^+ cations between the layers of Ti_3C_2 has been demonstrated suggesting that other large or multivalent cations may be similarly intercalated into MXenes from organic electrolyte solutions. $Ti_3C_2T_x$ capacitance was increased 3-fold, up to 85 F g^{-1} and 245 F cm^{-3} at 2 mV s^{-1} by using

carbon nanotubes as an additive to improve ion accessibility to the active material. The CNT/$Ti_3C_2T_x$ electrodes showed a good rate performance and good cycle life stability.

Considering that this was the first report on capacitance of Ti_3C_2 in organic electrolytes used in supercapacitors and that Ti_3C_2 is only one of more than a dozen of MXenes already synthesize, there are good reasons to expect further improvement in capacitance as the optimal MXene-electrolyte couples have been identified and their performance optimized. It took less than two years to increase capacitance of Ti_3C_2-MXene in aqueous electrolyte from about 100 F g^{-1} (*172*) to 320 F g^{-1} (*178*) and fast improvement of capacitance is expected in organic electrolytes as well.

General Conclusions

In this work, the electrochemical behavior of a new family of two-dimensional materials called MXenes was investigated for designing high energy and power electrochemical storage. Various MXenes were prepared and tested as electrodes for supercapacitors in aqueous electrolytes, for sodium-ion hybrid capacitors, and for supercapacitors in organic electrolytes.

Investigation of Ti_3C_2-based electrodes in various aqueous electrolytes has shown the spontaneous intercalation of cations in neutral and basic electrolytes. The lattice expansion observed by X-ray diffraction could not be directly linked to the size of the cation, but rather to the contribution of both ion valence and pH. The electrochemical performances greatly depended on the electrolytes used. The *in-situ* X-ray diffraction results indicated that the energy storage mechanism was the cation pseudo-intercalation reaction.

The surface chemistry of $Ti_3C_2T_x$ was modified by pre-intercalation in basic solutions and after delamination process. The effects of the surface chemistry and the morphology were highlighted by comparison of the electrochemical behaviors of modified-Ti_3C_2 electrodes. The best performance in terms of capacitance was obtained with the delaminated Ti_3C_2 paper electrode in 1M H_2SO_4 with capacitances up to 520 F/cm^3 or 325 F/g. The volumetric capacitance is higher compared to similar materials. The corresponding maximum energy density of 16Wh per kg with a power density of 200 W per Kg of MXene was obtained. Although these values are higher than conventional carbon-based supercapacitors, they were limited by the small potential ranges.

As the intercalation of Na^+ was demonstrated from aqueous electrolyte, the design of organic sodium-ion capacitors was proposed. V_2C studied as a positive electrode exhibited Na^+ cations intercalation mechanism. The full cell assembled with V_2C and hard carbon showed capacity up to 50 mAh/g. The performances at higher rate were lower than other materials proposed for this application.

The research on supercapacitors in organic electrolyte using Ti_3C_2 electrode synthesized by a 'clay' method showed a promising electrochemical performance using a carbon nanotube/MXene composite, a gravimetric capacitance of 85 F/g was obtained, which was less than activated carbons. However, the volumetric capacitance, up to 245 F/cm^3, was higher than for other electrodes cycled in organic electrolytes. The high energy density of 8.10^{-2} Wh/cm^3 obtained at a power density of 16 W/cm^3 highlighted the promise of MXene for applications where the volume is the main concern. A different storage mechanism than the two previous cases was demonstrated, consisting of a two phase reaction based on the intercalation of the EMI^+ cation. Preliminary results suggested that the size of the cation had an influence on the electrochemical behavior.

To conclude, this thesis highlighted the need to develop new electrode materials and shows that MXenes are promising candidates for supercapacitor electrodes, but that further work is needed to better understand and optimize these materials.

Future Work

It was demonstrated that the surface chemistry of MXene can be modified by chemical treatment in various electrolytes and that it plays an important role in the electrochemical behavior of MXene. To further investigate these phenomena, work focusing on controlling the surface chemistry by other treatment (such as hydrogenation at high temperature) and using other analytical technics need to be performed. Besides, the spontaneous and electrochemical ions intercalation, demonstrated by X-ray diffraction, is not totally understood. The use of a broader variety of electrolytes could reveal more of the intercalation mechanism.

After investigating Ti_3C_2-based electrodes in aqueous electrolytes and organic electrolytes, which showed promising results, it sounds appealing to investigate their electrochemical behavior in ionic liquids to increase the energy and power densities by increasing the potential range. Indeed, EMITFSI dissolved in acetonitrile has a smaller potential stability window than its pure ionic liquid phase. It was demonstrated that EMI^+ dissolved in acetonitrile could be reversibly intercalated into $Ti_3C_2T_x$, but the physicochemical properties in ionic liquid are different, therefore a new study will take place.

Moreover, MXenes could be investigated in other energy storage applications. Ones of the most promising technologies under development are multivalent batteries based on Mg^{2+}, Ca^{2+} and Al^{3+}. The interest is that redox reactions with such ions exchange more electrons than with Li^+ or Na^+. It was demonstrated than at least Mg^{2+} spontaneously intercalates from aqueous electrolyte into Ti_3C_2 layers, which strongly encourages us to pursue in that direction.

Finally, this thesis mainly focused on Ti_3C_2 and V_2C, but they are members of a large family of two-dimensional transition metal carbides/nitrides. The synthesis work leading to new MXenes family needs to be continued. There is high probability that, if their composition and surface chemistry are properly controlled, other MXenes could achieve even higher electrochemical performances for the applications proposed here.

List of References

1. J. M. Tarascon, M. Armand, Issues and challenges facing rechargeable lithium batteries. *Nature* **414**, 359 (Nov, 2001).

2. J. R. Miller, P. Simon, Materials science - Electrochemical capacitors for energy management. *Science* **321**, 651 (Aug, 2008).

3. B. E. Conway, *Electrochemical supercapacitors: scientific fundamentals and technological applications*. (Springer Science & Business Media, 2013).

4. P. Simon, Y. Gogotsi, Materials for electrochemical capacitors. *Nature Materials.* **7**, 845 (Nov, 2008).

5. M. Armand, J. M. Tarascon, Building better batteries. *Nature* **451**, 652 (02/07/print, 2008).

6. M. Winter, R. J. Brodd, What Are Batteries, Fuel Cells, and Supercapacitors? *Chemical Reviews* **104**, 4245 (2004/10/01, 2004).

7. A. S. Arico, P. Bruce, B. Scrosati, J. M. Tarascon, W. Van Schalkwijk, Nanostructured materials for advanced energy conversion and storage devices. *Nature Materials.* **4**, 366 (May, 2005).

8. M. Naguib *et al.*, Two-Dimensional Nanocrystals Produced by Exfoliation of Ti_3AlC_2. *Advanced Materials* **23**, 4248 (2011).

9. M. Naguib *et al.*, MXene: a promising transition metal carbide anode for lithium-ion batteries. *Electrochemistry Communications* **16**, 61 (2012).

10. A. Volta, On the Electricity Excited by the Mere Contact of Conducting Substances of Different Kinds. In a Letter from Mr. Alexander Volta, F. R. S. Professor of Natural Philosophy in the University of Pavia, to the Rt. Hon. Sir Joseph Banks, Bart. K. B. P. R. S. *Philosophical Transactions of the Royal Society of London* **90**, 403 (January 1, 1800, 1800).

11. K. Mizushima, P. C. Jones, P. J. Wiseman, J. B. Goodenough, Li_xCoO_2 ($0<x<-1$): A new cathode material for batteries of high energy density. *Materials Research Bulletin* **15**, 783 (1980/06/01, 1980).

12. B. Di Pietro, M. Patriarca, B. Scrosati, On the use of rocking chair configurations for cyclable lithium organic electrolyte batteries. *Journal of Power Sources* **8**, 289 (1982/01/01, 1982).

13. H. I. Becker. (U.S. Patent 2800616 1957).

14. R. A. Rightmire. (U.S. Patent 3288641, 1966).

15. H. Helmholtz, Studien über electrische Grenzschichten. *Annalen der Physik* **243**, 337 (1879).

16. V. Augustyn, P. Simon, B. Dunn, Pseudocapacitive oxide materials for high-rate electrochemical energy storage. *Energy & Environmental Science* **7**, 1597 (2014).

17. T. Brousse, D. Bélanger, J. W. Long, To Be or Not To Be Pseudocapacitive? *Journal of the Electrochemical Society* **162**, A5185 (January 1, 2015, 2015).

18. M. S. Whittingham, Chemistry of intercalation compounds: Metal guests in chalcogenide hosts. *Progress in Solid State Chemistry* **12**, 41 (1978/01/01, 1978).

19. M. R. Palacin, Recent advances in rechargeable battery materials: a chemist's perspective. *Chemical Society Reviews* **38**, 2565 (2009).

20. M. M. Doeff, Y. Ma, S. J. Visco, L. C. De Jonghe, Electrochemical Insertion of Sodium into Carbon. *Journal of the Electrochemical Society* **140**, L169 (December 1, 1993, 1993).

21. Y. P. Ma, M. M. Doeff, S. J. Visco, L. C. Dejonghe, Rechargeable Na Naxcoo2 And $Na_{15}Pb_4$ Na_xCoO_2 Polymer Electrolyte Cells. *Journal of the Electrochemical Society* **140**, 2726 (Oct, 1993).

22. J. B. Goodenough, K.-S. Park, The Li-Ion Rechargeable Battery: A Perspective. *Journal of the American Chemical Society* **135**, 1167 (2013/01/30, 2013).

23. D. Liu, G. Cao, Engineering nanostructured electrodes and fabrication of film electrodes for efficient lithium ion intercalation. *Energy & Environmental Science* **3**, 1218 (2010).

24. P. G. Bruce, B. Scrosati, J.-M. Tarascon, Nanomaterials for Rechargeable Lithium Batteries. *Angewandte Chemie International Edition* **47**, 2930 (2008).

25. F. Risacher, B. Fritz, Origin of Salts and Brine Evolution of Bolivian and Chilean Salars. *Aquat Geochem* **15**, 123 (2009/02/01, 2009).

26. A. Yaksic, J. E. Tilton, Using the cumulative availability curve to assess the threat of mineral depletion: The case of lithium. *Resources Policy* **34**, 185 (12//, 2009).

27. P. Ge, M. Fouletier, Electrochemical intercalation of sodium in graphite. *Solid State Ionics* **28**, 1172 (1988/09/01, 1988).

28. D. A. Stevens, J. R. Dahn, The Mechanisms of Lithium and Sodium Insertion in Carbon Materials. *Journal of the Electrochemical Society* **148**, A803 (August 1, 2001, 2001).

29. R. C. Asher, A lamellar compound of sodium and graphite. *Journal of Inorganic and Nuclear Chemistry* **10**, 238 (5//, 1959).

30. S.-W. Kim, D.-H. Seo, X. Ma, G. Ceder, K. Kang, Electrode Materials for Rechargeable Sodium-Ion Batteries: Potential Alternatives to Current Lithium-Ion Batteries. *Advanced Energy Materials* **2**, 710 (2012).

31. B. L. Ellis, L. F. Nazar, Sodium and sodium-ion energy storage batteries. *Current Opinion in Solid State and Materials Science* **16**, 168 (8//, 2012).

32. V. Palomares *et al.*, Na-ion batteries, recent advances and present challenges to become low cost energy storage systems. *Energy & Environmental Science* **5**, 5884 (Mar, 2012).

33. V. Palomares, M. Casas-Cabanas, E. Castillo-Martinez, M. H. Han, T. Rojo, Update on Na-based battery materials. A growing research path. *Energy & Environmental Science* **6**, 2312 (2013).

34. C. Masquelier, L. Croguennec, Polyanionic (Phosphates, Silicates, Sulfates) Frameworks as Electrode Materials for Rechargeable Li (or Na) Batteries. *Chemical Reviews* **113**, 6552 (2013/08/14, 2013).

35. C. Delmas, F. Cherkaoui, A. Nadiri, P. Hagenmuller, A Nasicon-Type Phase As Intercalation Electrode - $NaTi_2(PO_4)_3$. *Materials Research Bulletin* **22**, 631 (May, 1987).

36. M. M. Doeff, M. Y. Peng, Y. P. Ma, L. C. Dejonghe, Orthorhombic Na_xMnO_2 As A Cathode Material For Secondary Sodium And Lithium Polymer Batteries. *Journal Of The Electrochemical Society* **141**, L145 (Nov, 1994).

37. J. Morales, J. Santos, J. L. Tirado, Electrochemical studies of lithium and sodium intercalation in $MoSe_2$. *Solid State Ionics* **83**, 57 (Jan, 1996).

38. M. M. Doeff *et al.*, Thin-Film Solid-State Sodium Batteries For Electric Vehicles. *Electrochimica Acta* **40**, 2205 (Oct, 1995).

39. D. A. Stevens, J. R. Dahn, High Capacity Anode Materials for Rechargeable Sodium-Ion Batteries. *Journal of the Electrochemical Society* **147**, 1271 (April 1, 2000, 2000).

40. P. Thomas, D. Billaud, Electrochemical insertion of sodium into hard carbons. *Electrochimica Acta* **47**, 3303 (Aug, 2002).

41. S. Komaba *et al.*, Electrochemical Na Insertion and Solid Electrolyte Interphase for Hard-Carbon Electrodes and Application to Na-Ion Batteries. *Advanced Functional Materials* **21**, 3859 (Oct, 2011).

42. A. Ponrouch, A. R. Goñi, M. R. Palacín, High capacity hard carbon anodes for sodium ion batteries in additive free electrolyte. *Electrochemistry Communications* **27**, 85 (2013).

43. H. Xiong, M. D. Slater, M. Balasubramanian, C. S. Johnson, T. Rajh, Amorphous TiO_2 Nanotube Anode for Rechargeable Sodium Ion Batteries. *The Journal of Physical Chemistry Letters* **2**, 2560 (2011/10/20, 2011).

44. P. Senguttuvan, G. Rousse, V. Seznec, J. M. Tarascon, M. R. Palacin, $Na_2Ti_3O_7$: Lowest Voltage Ever Reported Oxide Insertion Electrode for Sodium Ion Batteries. *Chemistry of Materials* **23**, 4109 (Sep, 2011).

45. C. Delmas, C. Fouassier, P. Hagenmuller, Structural classification and properties of the layered oxides. *Physica B+C* **99**, 81 (1//, 1980).

46. Y. Cao *et al.*, Reversible Sodium Ion Insertion in Single Crystalline Manganese Oxide Nanowires with Long Cycle Life. *Advanced Materials* **23**, 3155 (2011).

47. S. Komaba *et al.*, Fluorinated Ethylene Carbonate as Electrolyte Additive for Rechargeable Na Batteries. *ACS Applied Materials & Interfaces* **3**, 4165 (Nov, 2011).

48. R. Berthelot, D. Carlier, C. Delmas, Electrochemical investigation of the P2–Na_xCoO_2 phase diagram. *Nature Materials* **10**, 74 (01//print, 2011).

49. J. Billaud *et al.*, beta-$NaMnO_2$: A High-Performance Cathode for Sodium-Ion Batteries. *Journal of the American Chemical Society* **136**, 17243 (Dec, 2014).

50. H. Yoshida, N. Yabuuchi, S. Komaba, $NaFe_{0.5}Co_{0.5}O_2$ as high energy and power positive electrode for Na-ion batteries. *Electrochemistry Communications* **34**, 60 (Sep, 2013).

51. A. Mendiboure, C. Delmas, P. Hagenmuller, Electrochemical Intercalation And Deintercalation Of Naxmno2 Bronzes. *Journal of Solid State Chemistry* **57**, 323 (1985).

52. A. Bhide, K. Hariharan, Physicochemical properties of Na_xCoO_2 as a cathode for solid state sodium battery. *Solid State Ionics* **192**, 360 (Jun, 2011).

53. A. K. Padhi, K. S. Nanjundaswamy, J. B. Goodenough, Phospho-olivines as Positive-Electrode Materials for Rechargeable Lithium Batteries. *Journal of the Electrochemical Society* **144**, 1188 (April 1, 1997, 1997).

54. T. Shiratsuchi, S. Okada, J. Yamaki, T. Nishida, $FePO_4$ cathode properties for Li and Na secondary cells. *Journal of Power Sources* **159**, 268 (Sep, 2006).

55. S. M. Oh, S. T. Myung, J. Hassoun, B. Scrosati, Y. K. Sun, Reversible $NaFePO_4$ electrode for sodium secondary batteries. *Electrochemistry Communications* **22**, 149 (Aug, 2012).

56. P. Moreau, D. Guyomard, J. Gaubicher, F. Boucher, Structure and Stability of Sodium Intercalated Phases in Olivine FePO4. *Chemistry of Materials* **22**, 4126 (Jul, 2010).

57. K. Zaghib *et al.*, Characterization of Na-based phosphate as electrode materials for electrochemical cells. *Journal of Power Sources* **196**, 9612 (Nov, 2011).

58. J. Gopalakrishnan, K. K. Rangan, $V_2(PO_4)_3$ - A Novel Nasicon-Type Vanadium Phosphate Synthesized By Oxidative Deintercalation Of Sodium From $Na_3V_2(PO_4)_3$. *Chemistry of Materials* **4**, 745 (Jul-Aug, 1992).

59. S. Patoux, G. Rousse, J. B. Leriche, C. Masquelier, Structural and electrochemical studies of rhombohedral $Na_2TiM(PO_4)_{(3)}$ and $Li_{1.6}Na_{0.4}TiM(PO_4)_{(3)}$ (M = Fe, Cr) phosphates. *Chemistry of Materials* **15**, 2084 (May, 2003).

60. Z. L. Jian *et al.*, Carbon coated $Na_3V_2(PO_4)_3$ as novel electrode material for sodium ion batteries. *Electrochemistry Communications* **14**, 86 (Jan, 2012).

61. J. Kang *et al.*, High rate performance of a $Na_3V_2(PO_4)_3$ /C cathode prepared by pyro-synthesis for sodium-ion batteries. *Journal of Materials Chemistry* **22**, 20857 (2012).

62. K. Saravanan, C. W. Mason, A. Rudola, K. H. Wong, P. Balaya, The First Report on Excellent Cycling Stability and Superior Rate Capability of $Na_3V_2(PO_4)_3$ for Sodium Ion Batteries. *Advanced Energy Materials* **3**, 444 (Apr, 2013).

63. H. Li, Y. Bai, F. Wu, Q. Ni, C. Wu, $Na_3V_2(PO_4)_3$ /C nanorods as advanced cathode material for sodium ion batteries. *Solid State Ionics* **278**, 281 (Oct, 2015).

64. F. Sauvage, L. Laffont, J. M. Tarascon, E. Baudrin, Study of the insertion/deinsertion mechanism of sodium into $Na_{0.44}MnO_2$. *Inorganic Chemistry* **46**, 3289 (Apr, 2007).

65. A. Ponrouch, E. Marchante, M. Courty, J. M. Tarascon, M. R. Palacin, In search of an optimized electrolyte for Na-ion batteries. *Energy & Environmental Science* **5**, 8572 (Sep, 2012).

66. C. Vidal-Abarca *et al.*, Improving the cyclability of sodium-ion cathodes by selection of electrolyte solvent. *Journal of Power Sources* **197**, 314 (1/1/, 2012).

67. R. Kotz, M. Carlen, Principles and applications of electrochemical capacitors. *Electrochimica Acta* **45**, 2483 (2000).

68. G. P. Wang, L. Zhang, J. J. Zhang, A review of electrode materials for electrochemical supercapacitors. *Chemical Society Reviews* **41**, 797 (2012).

69. D. L. Chapman, LI. A contribution to the theory of electrocapillarity. *Philosophical Magazine Series 6* **25**, 475 (1913/04/01, 1913).

70. D. C. Grahame, The Electrical Double Layer and the Theory of Electrocapillarity. *Chemical Reviews* **41**, 441 (1947/12/01, 1947).

71. A. G. Pandolfo, A. F. Hollenkamp, Carbon properties and their role in supercapacitors. *Journal of Power Sources* **157**, 11 (Jun, 2006).

72. J. Gamby, P. L. Taberna, P. Simon, J. F. Fauvarque, M. Chesneau, Studies and characterisations of various activated carbons used for carbon/carbon supercapacitors. *Journal of Power Sources* **101**, 109 (Oct, 2001).

73. L. L. Zhang, X. S. Zhao, Carbon-based materials as supercapacitor electrodes. *Chemical Society Reviews* **38**, 2520 (2009).

74. W. Gu, G. Yushin, Review of nanostructured carbon materials for electrochemical capacitor applications: advantages and limitations of activated carbon, carbide-derived carbon, zeolite-templated carbon, carbon aerogels, carbon nanotubes, onion-like carbon, and graphene. *Wiley Interdisciplinary Reviews: Energy and Environment* **3**, 424 (2014).

75. N. Mohamad Nor, L. C. Lau, K. T. Lee, A. R. Mohamed, Synthesis of activated carbon from lignocellulosic biomass and its applications in air pollution control—a review. *Journal of Environmental Chemical Engineering* **1**, 658 (12//, 2013).

76. O. Barbieri, M. Hahn, A. Herzog, R. Kötz, Capacitance limits of high surface area activated carbons for double layer capacitors. *Carbon* **43**, 1303 (5//, 2005).

77. J. Chmiola, G. Yushin, R. Dash, Y. Gogotsi, Effect of pore size and surface area of carbide derived carbons on specific capacitance. *Journal of Power Sources* **158**, 765 (2006).

78. R. Dash *et al.*, Titanium carbide derived nanoporous carbon for energy-related applications. *Carbon* **44**, 2489 (2006).

79. C. Largeot *et al.*, Relation between the ion size and pore size for an electric double-layer capacitor. *Journal of the American Chemical Society* **130**, 2730 (2008).

80. B. E. Conway, V. Birss, J. Wojtowicz, The role and utilization of pseudocapacitance for energy storage by supercapacitors. *Journal of Power Sources* **66**, 1 (5//, 1997).

81. P. Simon, Y. Gogotsi, B. Dunn, Where Do Batteries End and Supercapacitors Begin? *Science* **343**, 1210 (Mar, 2014).

82. B. E. Conway, E. Gileadi, Kinetic theory of pseudo-capacitance and electrode reactions at appreciable surface coverage. *Transactions of the Faraday Society* **58**, 2493 (1962).

83. W. Sugimoto, H. Iwata, K. Yokoshima, Y. Murakami, Y. Takasu, Proton and Electron Conductivity in Hydrous Ruthenium Oxides Evaluated by Electrochemical Impedance Spectroscopy: The Origin of Large Capacitance. *The Journal of Physical Chemistry B* **109**, 7330 (2005/04/01, 2005).

84. W. Sugimoto, T. Kizaki, K. Yokoshima, Y. Murakami, Y. Takasu, Evaluation of the pseudocapacitance in RuO2 with a RuO_2/GC thin film electrode. *Electrochimica Acta* **49**, 313 (1/15/, 2004).

85. J. M. Miller, B. Dunn, Morphology and electrochemistry of ruthenium/carbon aerogel nanostructures. *Langmuir* **15**, 799 (Feb, 1999).

86. W. Sugimoto, H. Iwata, Y. Yasunaga, Y. Murakami, Y. Takasu, Preparation of ruthenic acid nanosheets and utilization of its interlayer surface for electrochemical energy storage. *Angewandte Chemistry International Edition* **42**, 4092 (2003).

87. B. E. Conway, Transition From Supercapacitor To Battery Behavior In Electrochemical Energy-Storage. *Journal of the Electrochemical Society* **138**, 1539 (Jun, 1991).

88. J. P. Zheng, P. J. Cygan, T. R. Jow, Hydrous ruthenium oxide as an electrode material for electrochemical capacitors. *Journal of the Electrochemical Society* **142**, 2699 (Aug, 1995).

89. N. L. Wu, Nanocrystalline oxide supercapacitors. *Materials Chemistry and Physics* **75**, 6 (Apr, 2002).

90. X.-h. Yang, Y.-g. Wang, H.-m. Xiong, Y.-y. Xia, Interfacial synthesis of porous MnO_2 and its application in electrochemical capacitor. *Electrochimica Acta* **53**, 752 (2007).

91. M. Galiński, A. Lewandowski, I. Stępniak, Ionic liquids as electrolytes. *Electrochimica Acta* **51**, 5567 (8/15/, 2006).

92. M. Ue, M. Takeda, M. Takehara, S. Mori, Electrochemical Properties of Quaternary Ammonium Salts for Electrochemical Capacitors. *Journal of the Electrochemical Society* **144**, 2684 (August 1, 1997, 1997).

93. E. Frackowiak, G. Lota, J. Pernak, Room-temperature phosphonium ionic liquids for supercapacitor application. *Applied Physical Letter* **86**, (Apr, 2005).

94. J. R. Miller, Proceedings of the Fifth International Seminar on Double-Layer Capacitors and Similar Energy Storage Devices. *S. P. Wolsky, N. Marincic, eds., Florida Educational Seminars, Boca Raton, Fla (1995).* (1995).

95. K. Naoi, P. Simon, New Materials and New Configurations for Advanced Electrochemical Capacitors. *Journal of the Electrochemical Society*, 34 (2008).

96. K. Naoi, S. Ishimoto, J. Miyamoto, W. Naoi, Second generation 'nanohybrid supercapacitor': Evolution of capacitive energy storage devices. *Energy & Environmental Science* **5**, 9363 (Nov, 2012).

97. J. H. Park, O. O. Park, K. H. Shin, C. S. Jin, J. H. Kim, An electrochemical capacitor based on a Ni (OH) 2/activated carbon composite electrode. *Electrochemical and Solid-State Letters* **5**, H7 (2002).

98. AxionPower, http://www.axionpower.com/.

99. T. Brousse *et al.*, Long-term cycling behavior of asymmetric activated carbon/MnO2 aqueous electrochemical supercapacitor. *Journal of Power Sources* **173**, 633 (11/8/, 2007).

100. G. G. Amatucci, F. Badway, A. Du Pasquier, T. Zheng, An asymmetric hybrid nonaqueous energy storage cell. *Journal of the Electrochemical Society* **148**, A930 (Aug, 2001).

101. A. Du Pasquier, I. Plitz, J. Gural, S. Menocal, G. Amatucci, Characteristics and performance of 500 F asymmetric hybrid advanced supercapacitor prototypes. *Journal of Power Sources* **113**, 62 (2003).

102. K. Naoi, S. Ishimoto, N. Ogihara, Y. Nakagawa, S. Hatta, Encapsulation of Nanodot Ruthenium Oxide into KB for Electrochemical Capacitors. *Journal of the Electrochemical Society* **156**, A52 (January 1, 2009, 2009).

103. K. Naoi, 'Nanohybrid Capacitor': The Next Generation Electrochemical Capacitors. *Fuel Cells* **10**, 825 (2010).

104. V. Khomenko, E. Raymundo-Piñero, F. Béguin, High-energy density graphite/AC capacitor in organic electrolyte. *Journal of Power Sources* **177**, 643 (3/1/, 2008).

105. JMEnergy, *http://jmenergy.co.jp/en/profile.html*.

106. R. Ding, L. Qi, H. Wang, An investigation of spinel $NiCo_2O_4$ as anode for Na-ion capacitors. *Electrochimica Acta* **114**, 726 (2013).

107. K. Kuratani *et al.*, Na-ion capacitor using sodium pre-doped hard carbon and activated carbon. *Electrochimica Acta* **76**, 320 (2012).

108. J. Yin, L. Qi, H. Wang, Sodium Titanate Nanotubes as Negative Electrode Materials for Sodium-Ion Capacitors. *ACS Applied Material Interfaces* **4**, 2762 (2012/05/23, 2012).

109. Z. Chen *et al.*, High-Performance Sodium-Ion Pseudocapacitors Based on Hierarchically Porous Nanowire Composites. *Acs Nano* **6**, 4319 (2012/05/22, 2012).

110. Z. Yu, L. Tetard, L. Zhai, J. Thomas, Supercapacitor electrode materials: nanostructures from 0 to 3 dimensions. *Energy & Environmental Science* **8**, 702 (2015).

111. A. K. Geim, K. S. Novoselov, The rise of graphene. *Nature Materials* **6**, 183 (03//print, 2007).

112. K. S. Novoselov *et al.*, Electric Field Effect in Atomically Thin Carbon Films. *Science* **306**, 666 (October 22, 2004, 2004).

113. J.-H. Chen, C. Jang, S. Xiao, M. Ishigami, M. S. Fuhrer, Intrinsic and extrinsic performance limits of graphene devices on SiO_2. *Nature Nanotechnology* **3**, 206 (04//print, 2008).

114. A. A. Balandin *et al.*, Superior Thermal Conductivity of Single-Layer Graphene. *Nano Letters* **8**, 902 (2008/03/01, 2008).

115. M. D. Stoller, S. Park, Y. Zhu, J. An, R. S. Ruoff, Graphene-Based Ultracapacitors. *Nano Letters* **8**, 3498 (2008/10/08, 2008).

116. J. Yan *et al.*, Preparation of a graphene nanosheet/polyaniline composite with high specific capacitance. *Carbon* **48**, 487 (2//, 2010).

117. S. Chen, J. Zhu, X. Wu, Q. Han, X. Wang, Graphene Oxide−MnO_2 Nanocomposites for Supercapacitors. *Acs Nano* **4**, 2822 (2010/05/25, 2010).

118. Y. Zhu *et al.*, Carbon-Based Supercapacitors Produced by Activation of Graphene. *Science* **332**, 1537 (June 24, 2011, 2011).

119. M. F. El-Kady, V. Strong, S. Dubin, R. B. Kaner, Laser Scribing of High-Performance and Flexible Graphene-Based Electrochemical Capacitors. *Science* **335**, 1326 (March 16, 2012, 2012).

120. Y. Sun, Q. Wu, G. Shi, Graphene based new energy materials. *Energy & Environmental Science* **4**, 1113 (2011).

121. X. Yang, C. Cheng, Y. Wang, L. Qiu, D. Li, Liquid-Mediated Dense Integration of Graphene Materials for Compact Capacitive Energy Storage. *Science* **341**, 534 (2013).

122. E. Yoo *et al.*, Large Reversible Li Storage of Graphene Nanosheet Families for Use in Rechargeable Lithium Ion Batteries. *Nano Letters* **8**, 2277 (2008/08/01, 2008).

123. P. Guo, H. Song, X. Chen, Hollow graphene oxide spheres self-assembled by W/O emulsion. *Journal of Materials Chemistry* **20**, 4867 (2010).

124. D. S. Su , R. Schlögl, Nanostructured Carbon and Carbon Nanocomposites for Electrochemical Energy Storage Applications. *ChemSusChem* **3**, 136 (2010).

125. D. Pan *et al.*, Li Storage Properties of Disordered Graphene Nanosheets. *Chemistry of Materials* **21**, 3136 (2009/07/28, 2009).

126. P. Lian *et al.*, Large reversible capacity of high quality graphene sheets as an anode material for lithium-ion batteries. *Electrochimica Acta* **55**, 3909 (4/30/, 2010).

127. P. Guo, H. Song, X. Chen, Electrochemical performance of graphene nanosheets as anode material for lithium-ion batteries. *Electrochemistry Communications* **11**, 1320 (6//, 2009).

128. E. Pollak *et al.*, The Interaction of Li^+ with Single-Layer and Few-Layer Graphene. *Nano Letters* **10**, 3386 (2010/09/08, 2010).

129. C. Uthaisar, V. Barone, Edge Effects on the Characteristics of Li Diffusion in Graphene. *Nano Letters* **10**, 2838 (2010/08/11, 2010).

130. J. Yan *et al.*, Fast and reversible surface redox reaction of graphene–MnO_2 composites as supercapacitor electrodes. *Carbon* **48**, 3825 (11//, 2010).

131. S. Chen, J. Zhu, X. Wang, One-Step Synthesis of Graphene−Cobalt Hydroxide Nanocomposites and Their Electrochemical Properties. *The Journal of Physical Chemistry C* **114**, 11829 (2010/07/15, 2010).

132. H. Wang, H. S. Casalongue, Y. Liang, H. Dai, $Ni(OH)_2$ Nanoplates Grown on Graphene as Advanced Electrochemical Pseudocapacitor Materials. *Journal of the American Chemical Society* **132**, 7472 (2010/06/02, 2010).

133. S. Yang, X. Feng, S. Ivanovici, K. Müllen, Fabrication of Graphene-Encapsulated Oxide Nanoparticles: Towards High-Performance Anode Materials for Lithium Storage. *Angewandte Chemie International Edition* **49**, 8408 (2010).

134. S.-M. Paek, E. Yoo, I. Honma, Enhanced Cyclic Performance and Lithium Storage Capacity of SnO_2/Graphene Nanoporous Electrodes with Three-Dimensionally Delaminated Flexible Structure. *Nano Letters* **9**, 72 (2009/01/14, 2009).

135. D. Wang *et al.*, Ternary Self-Assembly of Ordered Metal Oxide−Graphene Nanocomposites for Electrochemical Energy Storage. *Acs Nano* **4**, 1587 (2010/03/23, 2010).

136. J. Yao, X. Shen, B. Wang, H. Liu, G. Wang, In situ chemical synthesis of SnO_2–graphene nanocomposite as anode materials for lithium-ion batteries. *Electrochemistry Communications* **11**, 1849 (10//, 2009).

137. L.-S. Zhang *et al.*, Mono dispersed SnO_2 nanoparticles on both sides of single layer graphene sheets as anode materials in Li-ion batteries. *Journal of Materials Chemistry* **20**, 5462 (2010).

138. N. Zhu *et al.*, Graphene as a conductive additive to enhance the high-rate capabilities of electrospun $Li_4Ti_5O_{12}$ for lithium-ion batteries. *Electrochimica Acta* **55**, 5813 (8/1/, 2010).

139. Z.-S. Wu *et al.*, Graphene Anchored with Co_3O_4 Nanoparticles as Anode of Lithium Ion Batteries with Enhanced Reversible Capacity and Cyclic Performance. *Acs Nano* **4**, 3187 (2010/06/22, 2010).

140. S. Yang *et al.*, Fabrication of Cobalt and Cobalt Oxide/Graphene Composites: Towards High-Performance Anode Materials for Lithium Ion Batteries. *ChemSusChem* **3**, 236 (2010).

141. F.-Y. Su *et al.*, Flexible and planar graphene conductive additives for lithium-ion batteries. *Journal of Materials Chemistry* **20**, 9644 (2010).

142. Y. Ding *et al.*, Preparation of nano-structured $LiFePO_4$/graphene composites by co-precipitation method. *Electrochemistry Communications* **12**, 10 (1//, 2010).

143. L. Wang *et al.*, A facile method of preparing mixed conducting $LiFePO_4$/graphene composites for lithium-ion batteries. *Solid State Ionics* **181**, 1685 (12/13/, 2010).

144. G. Wang *et al.*, Sn/graphene nanocomposite with 3D architecture for enhanced reversible lithium storage in lithium ion batteries. *Journal of Materials Chemistry* **19**, 8378 (2009).

145. J. K. Lee, K. B. Smith, C. M. Hayner, H. H. Kung, Silicon nanoparticles-graphene paper composites for Li ion battery anodes. *Chemical Communications (Cambridge, United Kingdom)* **46**, 2025 (2010).

146. S.-L. Chou *et al.*, Enhanced reversible lithium storage in a nanosize silicon/graphene composite. *Electrochemistry Communications* **12**, 303 (2//, 2010).

147. X. Xu, W. Liu, Y. Kim, J. Cho, Nanostructured transition metal sulfides for lithium ion batteries: Progress and challenges. *Nano Today* **9**, 604 (10//, 2014).

148. H. Wang, H. B. Feng, J. H. Li, Graphene and Graphene-like Layered Transition Metal Dichalcogenides in Energy Conversion and Storage. *Small* **10**, 2165 (Jun, 2014).

149. J. Xiao *et al.*, Electrochemically Induced High Capacity Displacement Reaction of PEO/MoS2/Graphene Nanocomposites with Lithium. *Advanced Functional Materials* **21**, 2840 (2011).

150. T. Stephenson, Z. Li, B. Olsen, D. Mitlin, Lithium ion battery applications of molybdenum disulfide (MoS_2) nanocomposites. *Energy & Environmental Science* **7**, 209 (2014).

151. T. Brousse, S. M. Lee, L. Pasquereau, D. Defives, D. M. Schleich, Composite negative electrodes for lithium ion cells. *Solid State Ionics* **113**, 51 (Dec, 1998).

152. Y. Kim, J. B. Goodenough, Lithium Insertion into Transition-Metal Monosulfides: Tuning the Position of the Metal 4s Band. *The Journal of Physical Chemistry C* **112**, 15060 (2008/09/25, 2008).

153. J. Feng *et al.*, Metallic Few-Layered VS2 Ultrathin Nanosheets: High Two-Dimensional Conductivity for In-Plane Supercapacitors. *Journal of the American Chemical Society* **133**, 17832 (2011/11/09, 2011).

154. G. A. Muller, J. B. Cook, H.-S. Kim, S. H. Tolbert, B. Dunn, High Performance Pseudocapacitor Based on 2D Layered Metal Chalcogenide Nanocrystals. *Nano Letters* **15**, 1911 (2015/03/11, 2015).

155. M. Naguib *et al.*, Synthesis of a new nanocrystalline titanium aluminum fluoride phase by reaction of Ti_2AlC with hydrofluoric acid. *RSC Advances* **1**, 1493 (2011).

156. M. Naguib *et al.*, Two-Dimensional Transition Metal Carbides. *Acs Nano* **6**, 1322 (2012/02/28, 2012).

157. J. Come *et al.*, A Non-Aqueous Asymmetric Cell with a Ti_2C-Based Two-Dimensional Negative Electrode. *Journal of the Electrochemical Society* **159**, A1368 (2012).

158. M. W. Barsoum, The $M_{N+1}AX_N$ phases: A new class of solids: Thermodynamically stable nanolaminates. *Progress in Solid State Chemistry* **28**, 201 (2000).

159. O. Mashtalir *et al.*, Intercalation and delamination of layered carbides and carbonitrides. *Nature Communication* **4**, 1716 (04/16/online, 2013).

160. Q. Tang, Z. Zhou, P. Shen, Are MXenes Promising Anode Materials for Li Ion Batteries? Computational Studies on Electronic Properties and Li Storage Capability of Ti_3C_2 and $Ti_3C_2X_2$ (X = F, OH) Monolayer. *Journal of the American Chemical Society* **134**, 16909 (2012/10/10, 2012).

161. M. Ghidiu, M. R. Lukatskaya, M.-Q. Zhao, Y. Gogotsi, M. W. Barsoum, Conductive two-dimensional titanium carbide /`clay/' with high volumetric capacitance. *Nature* **516**, 78 (12/04/print, 2014).

162. M.-Q. Zhao *et al.*, Flexible MXene/Carbon Nanotube Composite Paper with High Volumetric Capacitance. *Advanced Materials* **27**, 339 (2015).

163. J. M. Tarascon *et al.*, First example of monodispersed $(Mo_3Se_3)1\infty$ clusters. *J. Solid State Chemistry* **58**, 290 (1985/07/15, 1985).

164. S. Goriparti *et al.*, Review on recent progress of nanostructured anode materials for Li-ion batteries. *Journal of Power Sources* **257**, 421 (7/1/, 2014).

165. M. Winter, J. O. Besenhard, M. E. Spahr, P. Novák, Insertion Electrode Materials for Rechargeable Lithium Batteries. *Advanced Materials* **10**, 725 (1998).

166. F. Nobili, F. Croce, B. Scrosati, R. Marassi, Electronic and Electrochemical Properties of $Li_xNi_{1-y}Co_yO_2$ Cathodes Studied by Impedance Spectroscopy. *Chemistry of Materials* **13**, 1642 (2001/05/01, 2001).

167. W. Van Schalkwijk, B. Scrosati, *Advances in lithium-ion batteries*. (Springer Science & Business Media, 2002).

168. D. Aurbach, Review of selected electrode-solution interactions which determine the performance of Li and Li ion batteries. *Journal of Power Sources* **89**, 206 (Aug, 2000).

169. R. de Levie, On porous electrodes in electrolyte solutions. *Electrochimica Acta* **8**, 751 (1963/10/01, 1963).

170. J.-F. Fauvarque, P. Simon, Principles of Electrochemistry and Electrochemical Methods. *Carbons for Electrochemical Energy Storage and Conversion Systems, RC Press/Taylor and Francis*, 1 (2009).

171. P. L. Taberna, P. Simon, J. F. Fauvarque, Electrochemical characteristics and impedance spectroscopy studies of carbon-carbon supercapacitors. *Journal of The Electrochemical Society* **150**, A292 (Mar, 2003).

172. M. R. Lukatskaya *et al.*, Cation Intercalation and High Volumetric Capacitance of Two-Dimensional Titanium Carbide. *Science* **341**, 1502 (Sep, 2013).

173. V. Augustyn *et al.*, High-rate electrochemical energy storage through Li^+ intercalation pseudocapacitance. *Nature Materials* **12**, 518 (06//print, 2013).

174. Z. Sun *et al.*, Microstructure and supercapacitive properties of buserite-type manganese oxide with a large basal spacing. *Journal of Power Sources* **216**, 425 (10/15/, 2012).

175. Y. Xie *et al.*, Role of Surface Structure on Li-Ion Energy Storage Capacity of Two-Dimensional Transition-Metal Carbides. *Journal of the American Chemical Society* **136**, 6385 (2014/04/30, 2014).

176. L. M. Viculis, J. J. Mack, O. M. Mayer, H. T. Hahn, R. B. Kaner, Intercalation and exfoliation routes to graphite nanoplatelets. *Journal of Materials Chemistry* **15**, 974 (2005).

177. Y. Hernandez *et al.*, High-yield production of graphene by liquid-phase exfoliation of graphite. *Nature Nanotechnology* **3**, 563 (09//print, 2008).

178. Y. Dall'Agnese *et al.*, High capacitance of surface-modified 2D titanium carbide in acidic electrolyte. *Electrochemistry Communications* **48**, 118 (2014).

179. P. W. Ruch *et al.*, A dilatometric and small-angle X-ray scattering study of the electrochemical activation of mesophase pitch-derived carbon in non-aqueous electrolyte solution. *Carbon* **48**, 1880 (2010).

180. M. R. Lukatskaya *et al.*, Probing the Mechanism of High Capacitance in 2D Titanium Carbide Using In Situ X-Ray Absorption Spectroscopy. *Advanced Energy Materials* **5**, n/a (2015).

181. R. C. Weast, CRC Handbook of Chemistry, and Physics, 70th Edition *CRC Press, Boca Raton, FL,* , D (1989).

182. A. V. Wolf, Aqueous Solutions and Body Fluids. *Harper and Row, New York*, (1966).

183. O. Ghodbane, F. Ataherian, N. L. Wu, F. Favier, In situ crystallographic investigations of charge storage mechanisms in MnO_2-based electrochemical capacitors. *Journal of Power Sources* **206**, 454 (May, 2012).

184. Y. Xie *et al.*, Prediction and Characterization of MXene Nanosheet Anodes for Non-Lithium-Ion Batteries. *Acs Nano* **8**, 9606 (2014/09/23, 2014).

185. S. Murali *et al.*, Volumetric capacitance of compressed activated microwave-expanded graphite oxide (a-MEGO) electrodes. *Nano Energy* **2**, 764 (9//, 2013).

186. J. Chmiola, C. Largeot, P.-L. Taberna, P. Simon, Y. Gogotsi, Monolithic Carbide-Derived Carbon Films for Micro-Supercapacitors. *Science* **328**, 480 (2010).

187. M. Heon *et al.*, Continuous carbide-derived carbon films with high volumetric capacitance. *Energy & Environmental Science* **4**, 135 (2011).

188. X. Lang, A. Hirata, T. Fujita, M. Chen, Nanoporous metal/oxide hybrid electrodes for electrochemical supercapacitors. *Nature Nanotechnology* **6**, 232 (04//print, 2011).

189. X. Zhao *et al.*, Incorporation of Manganese Dioxide within Ultraporous Activated Graphene for High-Performance Electrochemical Capacitors. *Acs Nano* **6**, 5404 (2012/06/26, 2012).

190. J. R. Miller, Valuing Reversible Energy Storage. *Science* **335**, 1312 (2012).

191. M. Naguib *et al.*, New Two-Dimensional Niobium and Vanadium Carbides as Promising Materials for Li-Ion Batteries. *Journal of the American Chemical Society* **135**, 15966 (2013/10/30, 2013).

192. M. M. Hantel, R. Nesper, A. Wokaun, R. Kötz, In-situ XRD and dilatometry investigation of the formation of pillared graphene via electrochemical activation of partially reduced graphite oxide. *Electrochimica Acta* **134**, 459 (7/10/, 2014).

193. Y. Dong *et al.*, Inhibiting effect of Na+ pre-intercalation in MoO_3 nanobelts with enhanced electrochemical performance. *Nano Energy* **15**, 145 (7//, 2015).

194. X. Wang *et al.*, Pseudocapacitance of MXene nanosheets for high-power sodium-ion hybrid capacitors. *Nature Communication* **6**, (04/02/online, 2015).

195. M. R. Lukatskaya *et al.*, Probing the Mechanism of High Capacitance in 2D Titanium Carbide Using In Situ X-Ray Absorption Spectroscopy. *Advanced Energy Materials*, n/a (2015).

196. Y. Dall'Agnese, P.-L. Taberna, Y. Gogotsi, P. Simon, Two-Dimensional Vanadium Carbide (MXene) as Positive Electrode for Sodium-Ion Capacitors. *The Journal of Physical Chemistry Letters* **6**, 2305 (2015).

197. X. Wang *et al.*, Atomic-Scale Recognition of Surface Structure and Intercalation Mechanism of Ti_3C_2X. *Journal of the American Chemical Society* **137**, 2715 (2015/02/25, 2015).

198. Y. Liu, W. Wang, Y. Ying, Y. Wang, X. Peng, Binder-free layered Ti_3C_2/CNTs nanocomposite anodes with enhanced capacity and long-cycle life for lithium-ion batteries. *Dalton Transactions* **44**, 7123 (2015).

199. Q. Cheng *et al.*, Graphene and carbon nanotube composite electrodes for supercapacitors with ultra-high energy density. *Physical Chemistry Chemical Physics* **13**, 17615 (2011).

200. X.-M. Liu *et al.*, Carbon nanotube (CNT)-based composites as electrode material for rechargeable Li-ion batteries: A review. *Composites Science and Technology* **72**, 121 (1/18/, 2012).

201. B. J. Landi, M. J. Ganter, C. D. Cress, R. A. DiLeo, R. P. Raffaelle, Carbon nanotubes for lithium ion batteries. *Energy & Environmental Science* **2**, 638 (2009).

202. Y. Dall'Agnese, P. Rozier, P.-L. Taberna, Y. Gogotsi, P. Simon, Capacitance of two-dimensional titanium carbide (MXene) and MXene/carbon nanotube composites in organic electrolytes. *Journal of Power Sources* **306**, 510 (2016).

203. Z. Ling *et al.*, Flexible and conductive MXene films and nanocomposites with high capacitance. *Proceedings of the National Academy of Sciences* **111**, 16676 (November 25, 2014, 2014).

204. R. Lin *et al.*, Solvent effect on the ion adsorption from ionic liquid electrolyte into sub-nanometer carbon pores. *Electrochimica Acta* **54**, 7025 (11/30/, 2009).

205. M. D. Levi *et al.*, Solving the Capacitive Paradox of 2D MXene using Electrochemical Quartz-Crystal Admittance and In Situ Electronic Conductance Measurements. *Advanced Energy Materials* **5**, 1400815 (2015).

206. J. M. Griffin *et al.*, In situ NMR and electrochemical quartz crystal microbalance techniques reveal the structure of the electrical double layer in supercapacitors. *Nature Materials* **14**, 812 (2015).

VITA

Yohan Dall'Agnese • yohan@dallagnese.fr

EDUCATION

2012 - 2016	PhD in Materials Science and Engineering	
	Drexel University, Philadelphia, USA	Advisor: Dr. Y. Gogotsi
	Université Paul Sabatier, Toulouse, France	Advisor: Dr. P. Simon
2010 - 2012	European Master in "Materials for Energy Storage and Conversion"	
	Erasmus Mundus Fellowship	
	Degree jointly awarded by 5 universities:	
	Université Paul Sabatier, Toulouse, France	
	Université de Provence; Marseille, France	
	Université de Picardie Jules Vernes, Amiens, France	
	Warsaw University of Technology, Warsaw, Poland	
	Universidad d Cordoba, Cordoba, Spain	
2007 - 2010	BSc Degree in "Chemistry and Materials Science"	
	Université Paul Sabatier, Toulouse, France	

PUBLICATIONS

Dall'Agnese, Y.; Rozier, P.; Taberna, P.-L.; Gogotsi, Y.; Simon, P., "Capacitance of two-dimensional titanium carbide (MXene) and MXene/carbon nanotube composites in organic electrolytes" *The Journal of Power Sources* **2016**, 306, 510-515.

Dall'Agnese, Y.; Taberna, P.-L.; Gogotsi, Y.; Simon, P., "Two-Dimensional Vanadium Carbide (MXene) as Positive Electrode for Sodium-Ion Capacitors." *The Journal of Physical Chemistry Letters* **2015**, 6, 2305-2309.

Dall'Agnese, Y.; Lukatskaya, M. R.; Cook, K. M.; Taberna, P.-L.; Gogotsi, Y.; Simon, P., "High capacitance of surface-modified 2D titanium carbide in acidic electrolyte." *Electrochemistry Communications*. **2014**, 48 (0), 118-122.

Xie, Y.; **Dall'Agnese, Y.**; Naguib, M.; Gogotsi, Y.; Barsoum, M. W.; Zhuang, H. L.; Kent, P. R. C., "Prediction and Characterization of MXene Nanosheet Anodes for Non-Lithium-Ion Batteries." *ACS Nano* **2014**, 8 (9), 9606-9615.

Lukatskaya, M. R.; Mashtalir, O.; Ren, C. E.; **Dall'Agnese, Y.**; Rozier, P.; Taberna, P. L.; Naguib, M.; Simon, P.; Barsoum, M. W.; Gogotsi, Y., "Cation Intercalation and High Volumetric Capacitance of Two-Dimensional Titanium Carbide." *Science* **2013**, 341 (6153), 1502-1505.

Mashtalir, O.; Naguib, M.; Mochalin, V. N.; **Dall'Agnese, Y.**; Heon, M.; Barsoum, M. W.; Gogotsi, Y., "Intercalation and delamination of layered carbides and carbonitrides." *Nature Communications* **2013**, 4, 1716.